Serial Crystallography: Beyond Monte Carlo Data Analysis

by

Chufeng Li

A Dissertation Presented in Partial Fulfillment
of the Requirements for the Degree
Doctor of Philosophy

Approved September 2016 by the
Graduate Supervisory Committee:

John Spence, Chair
Richard Kirian
Uwe Weierstall
Kevin Schmidt

ARIZONA STATE UNIVERSITY

December 2016

ABSTRACT

The superior brightness and ultra short pulse duration of X-ray free electron laser (XFEL) allows it to outrun radiation damage in coherent diffractive imaging since elastic scattering terminates before photoelectron cascades commences. This "diffract-before-destroy" feature of XFEL opened up new opportunities for biological macromolecule imaging and structure studies by breaking the limit to spatial resolution imposed by the maximum dose that is allowed before radiation damage. However, data collection in serial femto-second crystallography (SFX) using XFEL is affected by a bunch of stochastic factors, which pose great challenges to the data analysis in SFX. These stochastic factors include crystal size, shape, random orientation, X-ray photon flux, position and energy spectrum. Monte-Carlo integration proves effective and successful in extracting the structure factors by merging all diffraction patterns given that the data set is sufficiently large to average out all stochastic factors. However, this approach typically requires hundreds of thousands of patterns collected from experiments. This dissertation explores both experimental and algorithmic methods to eliminate or reduce the effect of stochastic factors in data acquisition and analysis. Coherent convergent X-ray beam diffraction (CCB) is discussed for possibilities of obtaining single-shot angular-integrated rocking curves. It is also shown the interference between Bragg disks helps ab-initio phasing. Two-color diffraction scheme is proposed for time-resolved studies and general data collection strategies are discussed based on error

metrics. A new auto-indexing algorithm for sparse patterns is developed and demonstrated for both simulated and experimental data. Statistics show that indexing rate is increased by 3 times for I3C data set collected from beam time LJ69 at Linac coherent light source (LCLS). Finally, dynamical inversion from electron diffraction is explored as an alternative approach for structure determination.

TABLE OF CONTENTS

Page

CHAPTER Page

CHAPTER Page

CHAPTER Page

CHAPTER Page

LIST OF FIGURES

Figure Page

Figure Page

Figure Page

CHAPTER 1

INTRODUCTION

Structure determines function

Structure determines function. The recognition of this basic principle has been through various fields of scientific research including materials science, condensed matter physics and structural biology. Graphite and diamond are both comprised of carbon, but the difference in their structures distinguishes them in mechanical characteristics. Graphite is used as a common lubricant in modern industry while diamond becomes the most well known cutting material. Numerous similar examples exist in the inorganic world where structure plays a decisive role.

Life science has been rapidly gaining public awareness since the beginning of 21st century because of its direct relevance to the human health and well being. Biological macromolecules such as DNA, RNA and proteins are the basic building blocks and functioning units of life systems. Determining the structures of these molecules directly results in understanding of fundamental biological processes and functions as well as the mechanisms of diseases. Besides unraveling biological processes and mechanisms, structural discoveries have also been known to identify target proteins and hence aid the design of drugs (Congreve, Murray, & Blundell, 2005). Structural studies of biological macromolecules are making an overwhelming impact on human health and the modern

world.

X-ray crystallography

Biomolecules are generally too small to be imaged even with the light microscopes of the best resolution. The methods used to determine their structures include mass spectroscopy, X-ray crystallography, cryogenic electron microscopy (cryo-EM), electron paramagnetic resonance (EPR) and nuclear magnetic resonance spectroscopy (NMR). Among these methods, X-ray crystallography and cryo-EM have the capability of imaging biomolecules at atomic resolution to give important details of their structures. With the rapid advancements in X-ray science and technology, the brilliance of X-ray light sources has improved by orders of magnitude over the past several decades (Ackermann et al., 2007). These bright light sources allow most of protein structures to be solved by X-ray crystallography. Thousands of new protein structures are determined using X-ray light sources such as synchrotrons every year and are deposited in the Protein Data Bank (PDB). Because the X-ray photons interact with matter relatively weekly, protein molecules need to be crystalized to sufficient size and diffracting-quality so that detectable signals can be collected from diffraction experiments. Growing crystals of diffracting-quality requires tremendous investments, efforts and becomes the main challenge for certain classes of proteins such as membrane proteins for structure determination using X-ray crystallography.

Radiation damage

Radiation damage is a critical problem in structure determination in X-ray crystallography as it distorts the native structure of proteins and also degrades the diffraction quality of crystals (Garman, 2013; Henderson, 1995). Radiation effect is observed to be resolution dependent (Barty et al., 2011; Garman, 2013) in X-ray diffraction experiments. The diffraction intensity gets weaker with the increased radiation dose deposited on the crystal and the high-resolution intensity degrades faster than that with lower resolutions. However, on the other hand, the diffraction signal is also proportional to the dose that is delivered to the sample. The achievable resolution is therefore limited by the maximum dose (Henderson, 1995) that can be deposited to the sample crystal before the radiation damage commences.

The radiation effect is generally avoided by limiting the dose. This can be realized by spreading the X-ray beam and distributing the photons to a larger sample volume. Alternatively, diffraction data from multiple identical crystals can be merged with each crystal receiving below the dose limit. One can also cool down the sample crystal to cryogenic temperature by liquid nitrogen to reduce the rate of radiation damage (Henderson, 1990).

X-ray free electron laser (XFEL) outruns radiation damage

The emergence and development of X-ray free electron laser (XFEL) is a huge

revolution to X-ray crystallography and structural biology studies (Spence, Weierstall, & Chapman, 2012). For biological macromolecules that are poorly crystalized or even single particles, the X-ray dose needed to obtain sufficient elastic scattering signals to solve the structure is enormously high. The coexistence of superior brightness and ultra short pulse duration of XFEL (Emma et al., 2010) enables the structural studies that are impossible using other light sources such as synchrotrons. It is pointed out that the femto-second level X-ray pulse can outrun the radiation damage, since the elastic scattering from sample is complete and recorded before the radical diffusion and photoelectron cascade processes commence (Neutze, Wouts, van der Spoel, Weckert, & Hajdu, 2000; Solem, 1986). The radiation damage is therefore eliminated or reduced from the collected data in this diffraction scheme. In this way, the damage free structures with atomic resolution can be obtained regardless of the dose. This novel imaging approach is termed as "diffract-before-destroy" (Chapman, 2009) and lies the foundation for serial femto-second crystallography (SFX).

Serial femto-second crystallography

There are four types of coherent diffractive imaging (CDI) experiments using XFEL: serial femto-second crystallography (SFX), snapshot wide angle X-ray scattering from solutions, single particle diffractive imaging and pump-probe experiments for time-resolved studies (Spence et al., 2012). Among these four experiments, SFX is

mostly chosen for structure study at atomic resolution because of its relatively strong scattering power and hence sharp signals. Protein crystals are delivered in a single-file jet using a gas dynamic virtual nozzle (GDVN) (DePonte et al., 2008) across the focus of the X-ray beam. Snapshot diffraction patterns are read out on a split detector at a 120 Hz frequency. Low angles data of the diffraction pattern are recorded on the back detector and high angle data on front detector. Snapshot diffraction patterns are collected from individual crystals of varying size, shape and in random orientations. In contrast to SFX, one large size crystal is rotated with a goniometer through different orientations and diffraction patterns are collected with full reflections in synchrotron crystallography. In SFX, hundreds of thousands of snapshot patterns from different crystals are then merged to a whole data set and passed to data analysis pipeline for later processing.

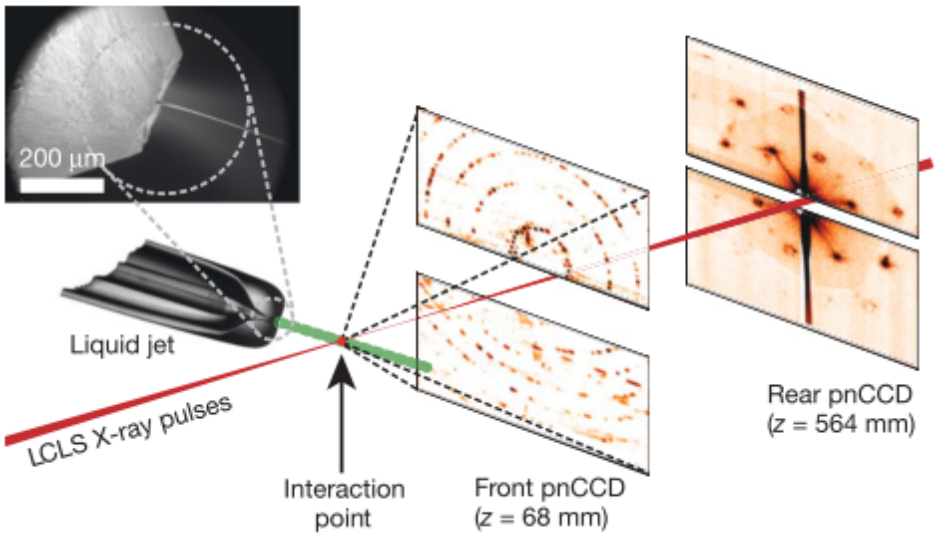

Fig. 1.1. General arrangement for serial femto-second crystallography (SFX) at LCLS (Chapman et al., 2011).

Data analysis pipeline

Because of the serial data collection nature of SFX, the whole data set can take up to hundreds of terabytes for one experiment. This unique problem of big data set for SFX necessitates a data reduction module as the first step of data processing. Data reduction software Cheetah distinguishes the "hit" events from blank frames where X-ray pulse misses the crystal (Barty et al., 2014). Along with hit finding, Cheetah also serves as a versatile diagnosis tool that monitors the data statistics of experiments in real time. After data reduction, the filtered patterns identified as hits are passed to the next analysis module to perform peak finding, indexing and lattice determination, intensity integration, scaling and merging (Spence et al., 2012; White et al., 2013). CrystFEL (White et al., 2013) package has been the most widely used among several freely available software suites for auto-mated SFX data analysis. CrystFEL also addresses more advanced problems in SFX data analysis such as indexing ambiguity, intensity scaling and partiality estimate and provides figures of merits for the whole data set.

Partiality problem

Snapshot diffraction patterns are collected from different crystals of varying size, shape and in random orientations. Each pattern is a still image that represents a

2-dimensional slice of the reciprocal lattice by the Ewald sphere (Fig. 1.2(b)). Therefore, most of the Bragg reflections sampled in a still image do not give their full intensities in the pattern (Fig. 1.2(a)). One must correct these partial intensities to full intensities to obtain the structure factor. This problem is termed as the partiality problem. An equivalent concept called "excitation error" is used instead in the field of electron diffraction. Since reflection intensity varies sensitively with slight change in crystal orientation, the partiality correction is essential in extracting correct structure factors, especially from a relatively small data set. A widely accepted geometrical model for partiality correction that treats reciprocal lattice points as spheres was discussed by Rossmann et al., 1979.

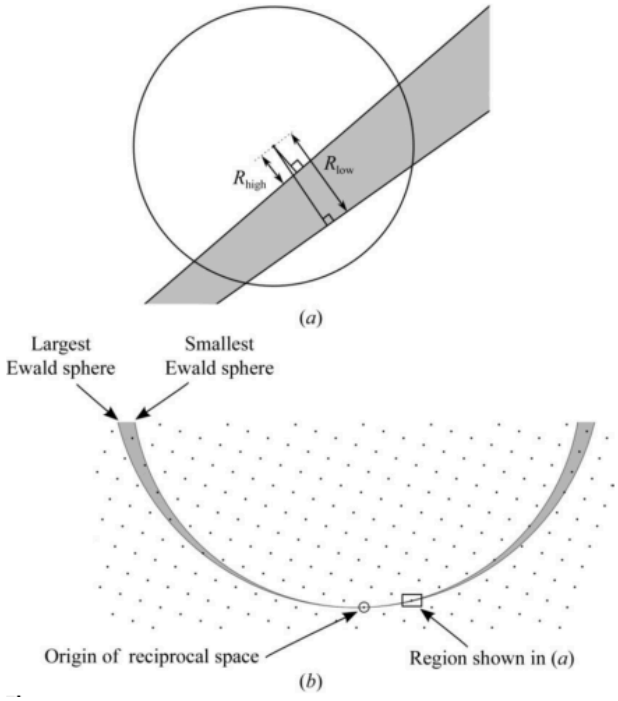

Fig. 1.2. (a) Geometrical model used for the partiality calculation. (b) context of the diagram. (White et al., 2013)

Stochastic factors and Monte-Carlo approach

In SFX experiments using XFEL, data are typically collected under lots of stochastic experimental conditions that fluctuate significantly. These stochastic factors include the crystal size, shape, lattice constants, mosaicity and orientation from which a snapshot diffraction pattern is collected. In addition, the XFEL beam also fluctuates in position, energy spectrum and intensity from shot to shot. All these stochastic factors in SFX data collection poses great challenges to the data analysis methods. The effects of these stochastic factors have not been corrected in a simple and consistent way. However, taking advantage of the vastness of the data set, Monte-Carlo approach was proposed by Kirian et al., 2010, which sums up intensities of the same Bragg orders from all patterns to average out these stochastic factors.

Scope of my thesis

Both experimental techniques and data analysis methods have been vastly developed over the past decade for structure determination using XFEL. Despite all these great achievements, more can be done to make XFEL an even more powerful and efficient tool for studies of structural determination and dynamics. This thesis explores different methods to eliminate or reduce the effects of stochastic factors in SFX to improve data

efficiency and hence cut the waste of sample and beam time. These efforts include both experimental design of new diffraction schemes and algorithmic development of data analysis methods. Chapter 2 proposes coherent convergent X-ray beam (CCB) diffraction using XFEL and discusses its potential use for time-resolved crystallography in three different cases: beam larger than crystal; beam smaller than crystal but bigger than unit cell; and beam smaller than unit cell. The possibilities of structure factor extraction; impact parameter estimate; and an ab-initio phasing approach from CCB patterns are discussed. Chapter 3 describes a two-color diffraction scheme for time-resolved studies of dynamics such as radiation damage. Three different SFX experiments are compared from the aspect of error metrics for structure factor measurement. Based on the comparison, data collection strategies are discussed for XFEL diffraction experiments. Chapter 4 describes development of a new algorithm for indexing sparse patterns and orientation refinement using intensity correlation. Efficiency of the algorithms is analyzed based on indexing statistics. Chapter 5 explores the possibility of solving the crystal structure by inversion from dynamical diffraction. Constraints and reconstruction algorithms are discussed in a mathematical framework.

CHAPTER 2

COHERENT CONVERGENT X-RAY BEAM TIME-RESOLVED DIFFRACTION

Introduction

Short and intense pulses generated by X-ray free electron lasers (XFELs) have been applied to study structural biology and overcome the damage problem in recent years. However, because of the low signal to noise ratio (SNR) of X-ray diffraction pattern from biological specimens, a large number of patterns are needed from the same crystal to determine the structure. In this work, properties of coherent convergent beam X-ray microdiffraction (CCB XRD) were discussed and possibility of structure factor extraction based on CCB configuration analyzed. Diffraction patterns from a Photosystem □(PS□) nanocrystal along c-axis are simulated with projection approximation in three different cases: 1. beam much larger than nanocrystal; 2. beam smaller than nanocrystal but larger than unit cell; 3. beam smaller than single unit cell. In case where beam convergence is larger than Bragg angle, adjacent Bragg orders overlap and interference fringes are obtained. This shadow image of nanocrystal is sensitive to probe coordinate which combined with large convergence diffraction indicates a lensless imaging technique similar to STEM. We also discuss the possibility of extracting structure factors from the angular integration over rocking curves of time-resolved snapshots with beam at the center or the edge of nanocrystal when the Bragg disks overlap or not. The dependence of

microdiffraction patterns on beam coordinate when the beam size is less than a single unit cell provides possible ideas on imaging the nanocrystals at atomic resolution lenslessly directly in combination with various phase retrieval algorithms(Fienup, 1982).

Plane-wave illumination

For plane wave illumination that models the normal XFEL radiation, the diffraction pattern is given by the kinematic theory as follow (Kirian et al., 2010):

$$I_n(\Delta\mathbf{k},\mathbf{k}_o,\alpha,\beta,\gamma,N_i) = J_o \,|F(\Delta\mathbf{k})|^2\, r_e^2 P(\mathbf{k}_o)\frac{\sin^2(N_1\Psi_1)}{\sin^2(\Psi_1)}\frac{\sin^2(N_2\Psi_2)}{\sin^2(\Psi_2)}\frac{\sin^2(N_3\Psi_3)}{\sin^2(\Psi_3)}\Delta\Omega \tag{2.1}$$

$$\begin{aligned}\Psi_1 &= 2\pi a\sin(\theta)\cos(\theta)/\lambda\\ \Psi_2 &= 2\pi b\sin(\theta)\cos(\beta)/\lambda\\ \Psi_3 &= 2\pi c\sin(\theta)\cos(\gamma)/\lambda\end{aligned} \tag{2.2}$$

where I_n is the intensity of diffraction pattern at the detector which corresponds to scattering vector $\Delta\mathbf{k} = \mathbf{k_o} - \mathbf{k_i}$ and subtends solid angel $\Delta\Omega$. The nanocrystal is composed of $N_1 \times N_2 \times N_3$ unit cells with a, b, c axis at angles of α,β,γ with $\Delta\mathbf{k}$. θ is the scattering angle and λ is the wavelength of incident X-ray. J_o denotes the incident photon flux and $F(\Delta\mathbf{k})$ is the structure factor of unit cell for scattering vector $\Delta\mathbf{k}$. r_e represents the Thomson radius of electron which has a value of 2.85 10-5, and $P(\mathbf{k}_o)$ describes the effect of X-ray polarization.

Coherent convergent beam (CCB) illumination —— reciprocal space

Diffraction pattern from coherent convergent beam X-ray (CCB) illumination which is of interest in this work, can be obtained by coherent superposition of diffraction patterns from plane waves designated by different $\mathbf{k_i}$ (Kirian et al., 2010). For convergence semi-angle θ_C, the intensity is expressed by the following formula:

$$I_C(\Delta\mathbf{k},\mathbf{k}_o,\alpha,\beta,\gamma,N_i,\theta_C) = A_C\left|\int_{k\le k_{\max}} \varphi(\Delta\mathbf{k},\mathbf{k}_i,\alpha,\beta,\gamma,N_i)d\mathbf{k}_i\right|^2 \Delta\Omega$$
$$\varphi(\Delta\mathbf{k},\mathbf{k}_i,\alpha,\beta,\gamma,N_i) = F(\Delta\mathbf{k})r_e P^{\frac{1}{2}}(\mathbf{k}_o)\frac{\sin(N_1\Psi_1)}{\sin(\Psi_1)}\frac{\sin(N_2\Psi_2)}{\sin(\Psi_2)}\frac{\sin(N_3\Psi_3)}{\sin(\Psi_3)} \quad (2.3)$$

where $\varphi(\Delta\mathbf{k},\mathbf{k}_i,\alpha,\beta,\gamma,N_i)$ is the contribution to exit wave function from plane wave component designated by $\mathbf{k}_i$. A_C is the normalization pre-factor which assures that the number of exit photons equals that of incident photons. The range of integration is the space within the illumination cone of the CCB which is represented by $k \le k_{\max}$ where $k_{\max} = \frac{\theta_C}{\lambda}$.

Coherent convergent beam (CCB) illumination —— real space

2-D projected diffraction patterns from CCB can also be calculated based on real space method. The elastic interaction between X-ray and specimen is relatively weak compared to electron scattering so that only single scattering is considered here. Because of this weak interaction, the X-ray wave function accumulates only a total phase shift after going through the specimen. Mathematically put, the effect of the specimen is to multiply the incidence wave function by a phase factor that is dependent on the integral

of the electron density of the specimen along the beam direction (projected electron density along c-axis). The wave function transmitted through the specimen is:

$$\varphi_{ex}(x,y) = \varphi_{in}(x,y)t(x,y) \tag{2.4}$$

where $\varphi_{in}(x,y)$ and $\varphi_{ex}(x,y)$ are the incident X-ray wave function and the exit X-ray wave function. $t(x,y)$ is the transmission function of the specimen and related to the projected electron density in the following way:

$$\begin{aligned} t(x,y) &= \exp[iC_X\rho_z(x,y)] \\ \rho_z(x,y) &= \int \rho(x,y,z)\,dz \end{aligned} \tag{2.5}$$

where $\rho(x,y,z)$ is the 3-D electron density distribution of the specimen and $\rho_z(x,y)$ is the projected electron density along beam direction (c-axis). C_X is the interaction constant which describes strength of interaction between X-ray and materials. C_X is often evaluated by the product of Thompson radius of electron $r_e = 2.82\times10^{-5}\,\mathring{A}$ and wavelength of the X-ray:

$$C_X = r_e\lambda \tag{2.6}$$

Therefore, for relatively thin specimens (e.g. 10 unit cells in beam direction) and X-ray with 1Å wavelength, $C_X\rho_z(x,y)$ is quite a small quantity (~10^{-3}) and weak phase object approximation (WPOA) is valid:

$$t(x,y) = \exp[iC_X\rho_z(x,y)] \approx 1 + iC_X\rho_z(x,y) \tag{2.7}$$

For CCB illumination, the incidence X-ray wave function is modeled by a probe function (Kirkland, 2010):

$$\varphi_P(\theta_C,\lambda,\Delta f,\boldsymbol{r}) = A_P \int_0^{k_{\max}} \exp(i\pi\lambda\Delta f\boldsymbol{k}^2)\exp(-2\pi i\boldsymbol{k}\cdot(\boldsymbol{r}-\boldsymbol{r_P}))d^2\boldsymbol{k} \qquad (2.8)$$

where Δf is the defocus, $\boldsymbol{r_P}$ is the probe center position and A_P is the normalization factor. When $\Delta f = 0$ which is the in-focus condition, the probe function turns out to be the first order Bessel function:

$$\varphi_P(\theta_C,\lambda,\Delta f = 0,\boldsymbol{r}) = c\frac{J_1(2\pi\theta_C|\boldsymbol{r}|/\lambda)}{2\pi\theta_C|\boldsymbol{r}|/\lambda} \qquad (2.9)$$

where c is a constant.

As discussed previously, the specimen could be represented by a projected 2-D electron density function $\rho_z(x,y)$. The calculation of $\rho_z(x,y)$ from structure factors $F(k_x,k_y,k_z)$ is implemented by using Fourier projection theorem (Kirkland, 2010):

$$\rho_z(x,y) = \int \rho(x,y,z)dz = FT_{2D}^{-1}[F(k_x,k_y,k_z=0)] \qquad (2.10)$$

where FT_{2D}^{-1} represents 2-D inverse Fourier transform with respect to k_x and k_y.

Finally the 2-D diffraction pattern is obtained by Fourier transform of the exit wave function:

$$I(k_x,k_y) = \left|\varphi(k_x,k_y)\right|^2$$
$$\varphi(k_x,k_y) = FT_{2D}[\varphi_{ex}(x,y)] \qquad (2.11)$$

where $I(k_x,k_y)$ and $\varphi(k_x,k_y)$ denote intensity and wave function of the 2-D diffraction pattern respectively.

Projection approximation

According to kinematic theory of X-ray scattering, Elastic scattering happens on the Ewald sphere which requires both energy and momentum conservation (Hawkes & Spence, 2007). Generally, centers of most reciprocal lattice points are not at Ewald sphere in the Ewald sphere construction which means that these Bragg orders are not exactly excited in diffraction. However, for thin specimens or nanocrystals, each Bragg order spread into a certain profile (i.e. shape transform) which has a width of about reciprocal of thickness in the beam direction. With the purpose of working out the principles of CCB XRD from nanocrystals, projection approximation is applied in computation of 2-D diffraction patterns. Projection approximation assumes "flat Ewald sphere" with zero curvature (plane) and it holds when Ewald sphere goes through central maxima of shape transforms. Projection approximation gives a spatial resolution limit to computation(Hawkes & Spence, 2007):

$$d_m > \left(\frac{\lambda t}{2}\right)^{\frac{1}{2}} \tag{2.12}$$

where t is the thickness of specimen.

Accordingly, structure factors within this spatial resolution limit are used when calculating the projected electron density.

Additionally, for CCB scattering geometry, the convergence semi-angle θ_C is further restricted by projection approximation. To assure that "flat Ewald sphere" for each plane-wave component within the "illumination cone" goes through central maxima

of shape transform, θ_C should be no greater than a certain value:

$$\theta_C < \frac{1/t}{g_{hkl}} = \frac{d_{hkl}}{t} \approx \frac{d_m}{t} = (\frac{\lambda}{2t})^{\frac{1}{2}} \tag{2.13}$$

Projection approximation takes different forms in reciprocal space and real space methods. In Eqn. (2.3) of reciprocal space method, to be consistent with projection approximation, we take $\gamma = 90°$ and $\Psi_3 = 0$. In real space method, Eqn. (2.4) is in fact based on the projection approximation in the first place. We notice that in both methods, once projection approximation is adopted, information of the shape transform along the beam direction vanishes.

Numerical simulation

Diffraction patterns from Photosystem Ⅱ (PS Ⅱ) nanocrystals with CCB X-ray are simulated based on real space method and projection approximation. Nanocrystals consisting of 10×10×10 unit cells and X-ray radiation with wavelength of 1Å are considered. Fig. 2.1(a) shows the PS Ⅱ nanocrystal geometry along with the 2-D electron density map projected along c-axis. As shown in Fig. 2.1(b), the computational superlattice is chosen to be relatively large compared to the size of nanocrystal to avoid computational artifacts, the dimensions are H=5U and L=5W (i.e. 5×5 times the size of nanocrystal).

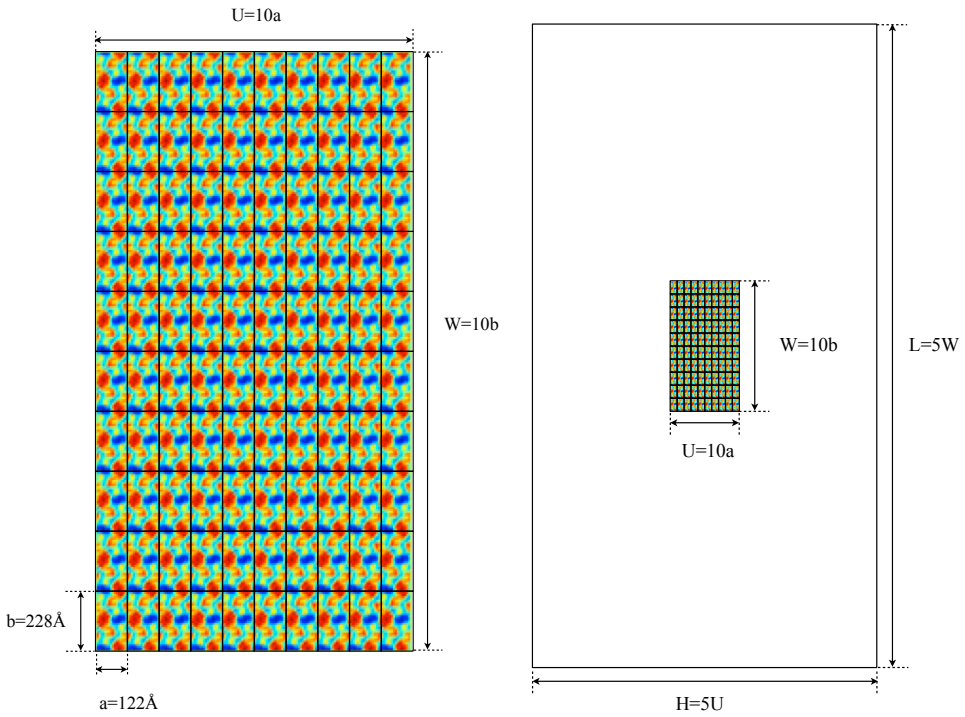

(a) (b)

Fig. 2.1. (a) Geometry of PS Ⅱ nanocrystal studied in this work (a=122Å, b=228Å, c=286Å, α=β=γ=90°) with the superimposed color map is the 2-D electron density projected along c-axis. Each square formed by the grid represents a unit cell. With 10×10×10 unit cells, the dimension of the nanocrystal is 122nm×228nm×286nm. (b) Configuration and relative sizes of unit cell, nanocrystal and computational superlattice. The computational superlattice is set to be 5×5 the size of nanocrystal.

Numerical simulation of CCB XRD from PS Ⅱ nanocrystal includes computations of specimen transmission function, probe function (incidence wave function), exit wave

function and diffraction pattern intensity. Schematic diagram of the whole CCB XRD system is shown in Fig. 2.2 (a). Algorithm implementation of CCB XRD simulation is based on Eqn. (2.4) to (11) and flow diagram is shown as in Fig. 2.2 (b). All simulations are carried out in MATLAB R2013a environment.

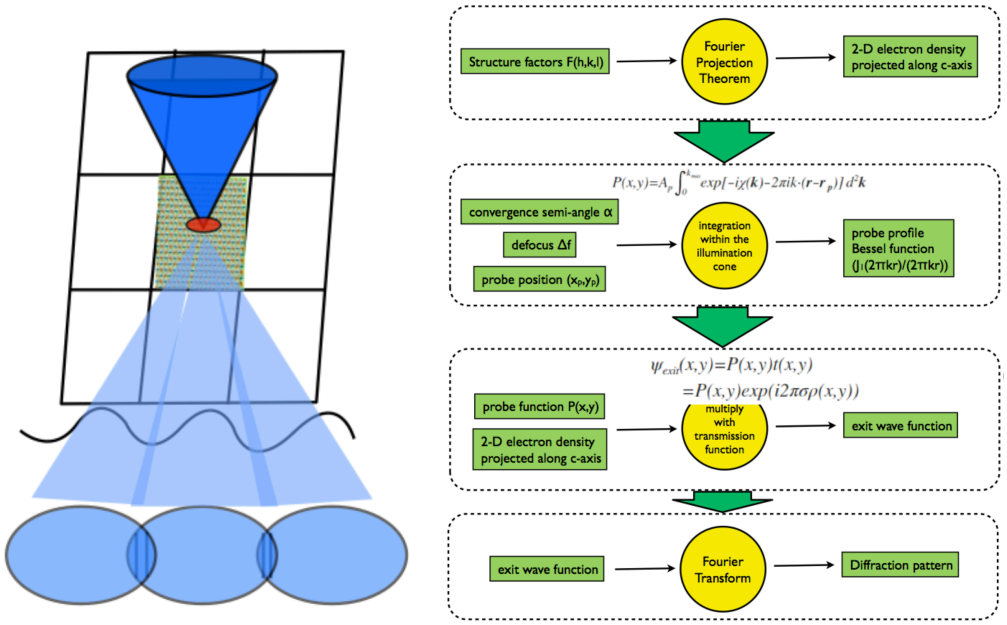

(a) (b)

Fig. 2.2. (a) Schematic diagram of CCB XRD from PS Ⅱ nanocrystals. (b) Flow diagram of algorithm implementation of CCB XRD simulation.

For X-ray wavelength $\lambda = 1\mathring{A}$ and specimen thickness $t = 286nm$, the resolution limit from projection approximation is $d_m = 37\mathring{A}$ according to Eqn. (2.12). Therefore, structure factors from Protein Data Bank (PDB) with 20Å resolution cutoff ($< d_m = 37\mathring{A}$)

are used to generate the projected electron density map. Convergence semi-angle θ_C is restricted to be less than 13.2mrad (~$6\theta_B$) based on Eqn. (2.13) and this is easily satisfied for purse of this work, which will be discussed later.

In MATLAB source codes, parameters including convergence semi-angle θ_C, defocus Δf, probe position $\boldsymbol{r_P}$ (Cartesian coordinates (x_P, y_P)), and numerical sampling rate are made adjustable so that effects of them on diffraction patterns can be studied. Specifically, three cases are simulated based on the relative sizes of unit cell b, nanocrystal W and probe size d_P: 1. probe size larger than nanocrystal $d_P >> W$ 2. probe size smaller than nanocrystal but larger than unit cell $b < d_P < W$ 3. probe size smaller than unit cell and adjacent Bragg disks overlap $d_P < b$. Also, diffraction patterns with beam approaching the edge of nanocrystal are simulated.

Beam larger than nanocrystal —— shape transform

First we consider the case where the beam is much larger than the nanocrystal $d_P >> W$. To implement this, convergence semi-angle is set to be $\theta_C = 0.001 mrad$, and the probe function can be almost treated as a plane wave. Diffraction pattern from a PS Ⅱ nanocrystal with a wide beam running along c axis are simulated and shown as in Fig. 2.3. 2-D sinc function shape transforms are clearly shown at each Bragg condition. The first minimum of the shape transform intensity is found to be at λ/W away from Bragg angle. This result is in exact accordance with prediction by Eqn. (2.1) ~ (2.3) from Kirian et al., 2010. Extraction of structure factors from diffraction patterns like Fig. 2.3 of

nanocrystals with random orientations in time-resolved crystallography requires angular integration over shape transforms using Mote Carlo approach .

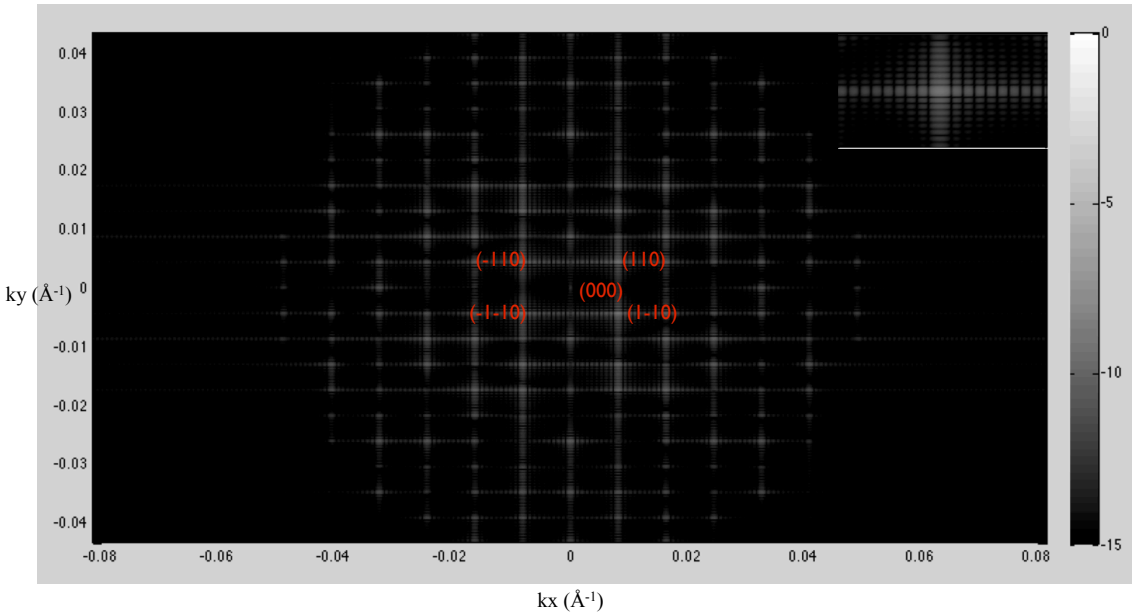

Fig. 2.3. CCB XRD pattern from a 10×10×10 unit cell PS Ⅱ nanocrystal when beam is much larger than nanocrystal with convergence angle θ_C =0.001mrad, defocus Δf=0, probe at center of nanocrystal. Shape transforms are clearly seen at each Bragg condition. Inset shows 2-D sinc function shape transform at (-110) Bragg spot.

Beam smaller than nanocrystal —— enhanced sampling power in reciprocal space

In the case where the probe size is smaller than nanocrystal but larger single unit cell, the probe is modeled by a probe function described by Eqn. (2.8), (2.9) and CCB XRD pattern is simulated based on Eqn. (2.4) ~ (2.11). To form a beam of this condition, convergence semi-angle $\theta_C = 1mrad$ and defocus $\Delta f = 0$ are used which give the radius of the probe $r_P = 0.61\lambda / \theta_C = 610\,\mathring{A}$ according to Rayleigh's criterion. To avoid artifacts

caused by the rapidly oscillating probe tails, probe function was multiplied by a Gaussian envelope function with cutoff of 500 Å. Resulting diffraction pattern from PS Ⅱ nanocrystal for this case under projection approximation is shown as in Fig. 2.4. Each Bragg spot is essentially an image of the illumination aperture neglecting the effect of the Gaussian envelope function. Shape transforms are not apparently seen in Fig. 2.4 compared to Fig. 2.3 that corresponds to the case where beam is much larger than nanocrystal. This can be easily understand from the view that the diffraction pattern is the convolution of the circular diffraction disk and the shape transform of the nanocrystal as a deduction from Eqn. (2.4), (2.7) and (2.11).

For this case, extraction of structure factors is simply implemented by integration over the diffraction disks. In contrast to conventional monochromatic X-ray beam used in SFX diffraction, the coherent convergent X-ray beam corresponds to an Ewald Shell instead of a thin sphere. Therefore, the CCBXRD is expected to yield more accurate structure factor measurements and faster convergence using fewer patterns because of its increased "Ewald volume" and hence stronger sampling power in reciprocal space. Simulations of 225000 snapshot diffraction patterns from PS Ⅱ nano-crystals with various X-ray divergence semi-angles were simulated, indexed and merged using software CrystFEL and CCP4. The result shows that larger divergence leads to smaller R-split factor and larger man partialities, which indicates that less data need to be collected to achieve a comparable accuracy in structure factor measurements and hence samples and beam time

could be conserved for CCBXRD (Spence, Zatsepin, & Li, 2014).

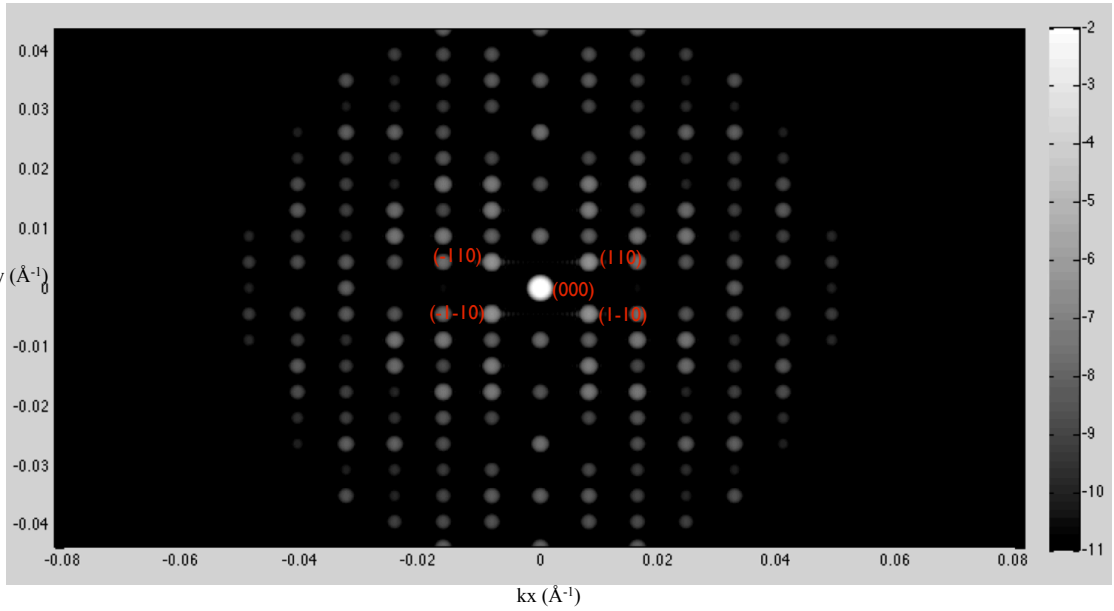

Fig. 2.4. Coherent diffraction pattern from 10 x 10 unit cell nanocrystal of PS Ⅱ, with convergence semi-angle θ_C=1mrad=0.45θ_B, defocus Δf=0, probe at center of nanocrystal, probe size~500Å, larger than unit cell but smaller than crystal (Resolution limit 20Å). Shape transforms are not seen and diffraction disks do not overlap.

Beam smaller than single unit cell —— interference fringes help phasing

In coherent X-ray microdiffraction, the spatial resolution in current use is about 100nm such as Linac coherent light source (LCLS) and could be pushed to 2nm in near future. Therefore, it is of potential importance to discuss the properties of CCB XRD pattern when beam is smaller than single unit cell. In order to form such a small beam, the convergence semi-angle used should be comparable to the Bragg angle θ_B according to Rayleigh's criterion and Bragg's law with small angle approximation as follows:

$$r_P = \frac{0.61\lambda}{\theta_C} \tag{2.14}$$

$$\theta_B = \frac{\lambda}{2b} \tag{2.15}$$

If we define the probe size d_P as the radius of Airy disk r_P, and set it equal to the lattice constant of PS Ⅱ nanocrystal b, then the convergence semi-angle

$$\theta_C = 1.22\theta_B \tag{2.16}$$

Under this condition in which the convergence semi-angle is larger Bragg angle, the neighbor diffraction disks overlap with each other as shown in inset of Fig. 2.5. As a result of CCB illumination, the neighbor disks interfere within the overlap region forming shadow images of the nanocrystal lattice (Cowley & Spence, 1981; John C.H. Spence, 2010). For PS Ⅱ nanocrystal, to implement this condition described by Eqn. (2.16), the convergence semi-angle is set as θ_C=2.7mrad=1.22θ_B and defocus Δf=0Å. The radius of the Bessel function probe is then 228Å which is equal to lattice constant b according to Rayleigh's criterion Eqn. (2.14). Fig. 2.5 is the schematic diagram of the relative sizes and postions of probe, unit cell and diffraction disks. Fig. 2.6 is a simulated diffraction pattern for the case where the probe size is equal to lattice constant b corresponding to the condition shown in Fig. 2.5 expect for the non-zero defocus. In this pattern, both dark and bright fringes are seen in the 22% overlap region between neighbor diffraction disks, which indicates the interference between Bragg orders. However, no more than one fringe is seen in each overlap region, this might be attributed to the relatively small

overlap fraction.

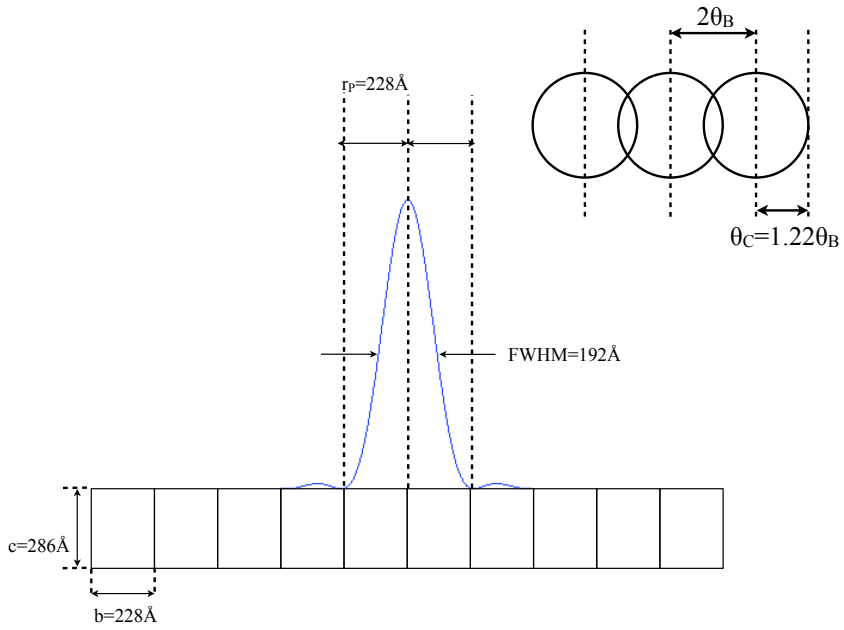

Fig. 2.5. Relative sizes of beam, PS Ⅱ nanocrystal unit cell, and diffraction disks, for the case where 22% overlap of orders makes the FWHM of the beam just equal to the period of the crystal. Upper right inset shows the corresponding diagram of the diffraction disks. This condition requires θ_C=2.7mrad=1.22θ_B, defocus Δf=0Å, Gaussian cutoff σ=500Å.

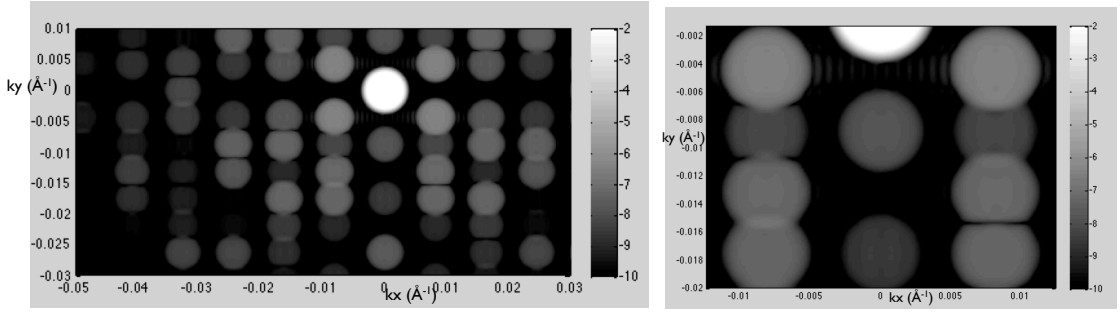

(a) (b)

Fig. 2.6. (a) CCB XRD pattern from 10 x 10 unit cell nanocrystal of PS Ⅱ, with beam

along c-axis, convergence semi-angle θ_C=2.7mrad=1.22θ_B, defocus Δf=-150000Å, Gaussian cutoff σ=500Å, probe at center of nanocrystal, probe size=228Å (Resolution limit 20Å). (b) enlarged view of (a). Interference fringes are seen in overlap region between disks, however the number of fringes in single overlap region is no more than one.

In order to see more interference fringes, larger convergence semi-angle was used which yields a larger overlap region. Fig. 2.7 is simulated diffraction pattern with convergence semi-angle θ_C=4mrad=1.82θ_B, defocus Δf=-150000Å, Gaussian cutoff σ=500Å. This condition gives a probe with radius of 152Å smaller than b and overlap fraction of about 82%. Sinusoidal lattice fringes are seen all over the overlap region. We also notice that circular fringes exist in some Bragg disks in the non-overlap region. This phenomenon is not obviously found in patterns simulated with small convergence and zero defocus conditions. Defocus and Gaussian cutoff might be the causes of this effect.

It is worthwhile to point out that parameters including convergence semi-angle θ_C, defocus Δf, and Gaussian cutoff σ take combined effects on diffraction patterns. To have larger overlap fraction, the convergence semi-angle θ_C is increased so that more lattice fringes come out. However, larger convergence semi-angle will also form a smaller probe, when the probe becomes too small, the periodicity of resulted diffraction pattern degrades and finally vanishes which is not desirable in extraction of structure factors. Also,

defocus affects contrast of lattice fringes in overlap region, but at the same time changes the profile of probe and hence spread its size. Additionally, Gaussian cutoff is chosen to avoid artifacts induced by the rapid oscillating probe tails. As a side effect, diffraction disks that are mathematically the Fourier transform of probe function are no longer uniform circular function. Therefore, based on the above discussion, an optimized condition should be chosen to form CCB XRD patterns. Fig. 2.7 is the simulated diffraction pattern with the optimized condition found.

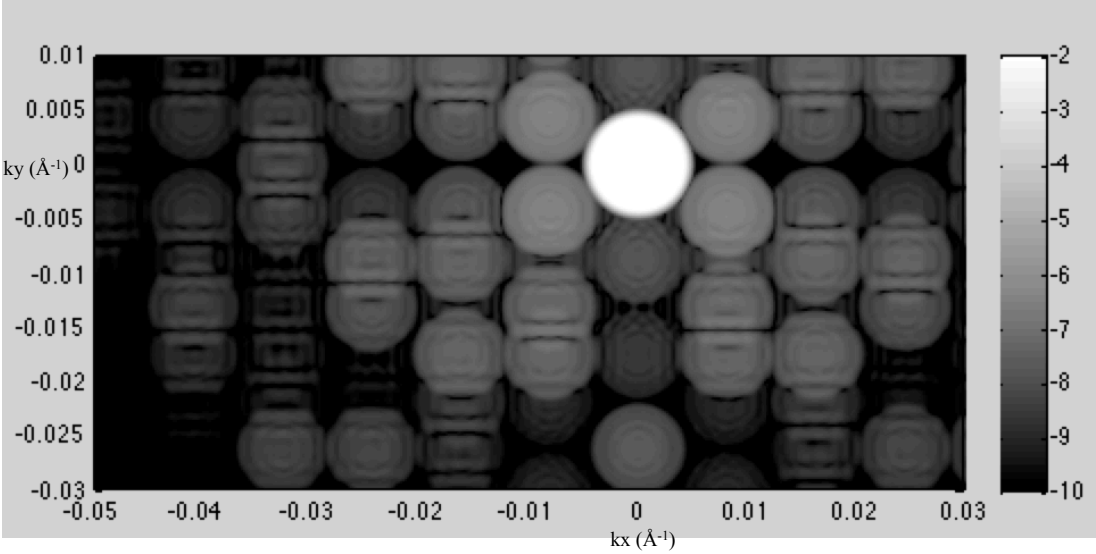

Fig. 2.7. CCB XRD pattern from 10 x 10 unit cell nanocrystal of PS Ⅱ, with convergence semi-angle θ_C=4mrad=1.82θ_B, defocus Δf=-150000Å, Gaussian cutoff σ=500Å, probe at center of nanocrystal, probe size smaller than unit cell (Resolution limit 20Å). Sinusoidal interference fringes are clearly seen in overlap region between disks.

These diffraction patterns with lattice fringes in the overlap region are sensitive to probe

position and have the same periodicity as the lattice. The fringes shift with the change of probe position, and the contrast reverses when the probe is moved away from its original position by half the unit cell constant. Furthermore, if many low order Bragg disks overlap all at the optic center using large convergence but maintaining the translational periodicity of the pattern, the interference pattern will ideally become a 2-D projected lattice image of the nanocrystal instead of fringes we seen in Fig. 2.7. With detectors properly positioned at different overlap regions of the diffraction patterns, STXM images with atomic resolution can be acquired with the beam scanning across the nanocrystal, which is similar to the STEM images in principle. An important feature of the interference pattern is that although intensity of fringes in overlap region is dependent on defocus and aberrations of optic system, the intensity of center point of overlap region is not by assuming only even-order aberrations are existent. This feature makes the potential atomic-resolution STXM images more stable and approachable with detectors positioned around the center points.

Another interesting case is when the probe is much smaller than single unit cell. As the Bragg disks gets larger and probe size shrinks with large convergence semi-angle, only information of only a few unit cells around the probe center is reflected in the pattern. Patterns resulted in this case are simulated and shown as in Fig. 2.8. Instead of periodic disk array such as shown in Fig. 2.6 and Fig. 2.7, cloud-like diffraction patterns are obtained as predicted previously. No translational periodicity is reflected in these patterns

while symmetries are shown. Comparing Fig.8 (a) generated with probe at an asymmetric point of nanocrystal and (b) generated with probe at an inversion center of nanocrystal, we see that point group symmetries of the projected 2-D lattice regarding the probe position could be reflected by the diffraction patterns. These patterns combined with interference fringes in overlap regions discussed previously indicate potential lensless imaging technique with CCBXRD not relying on phase retrieval algorithms.

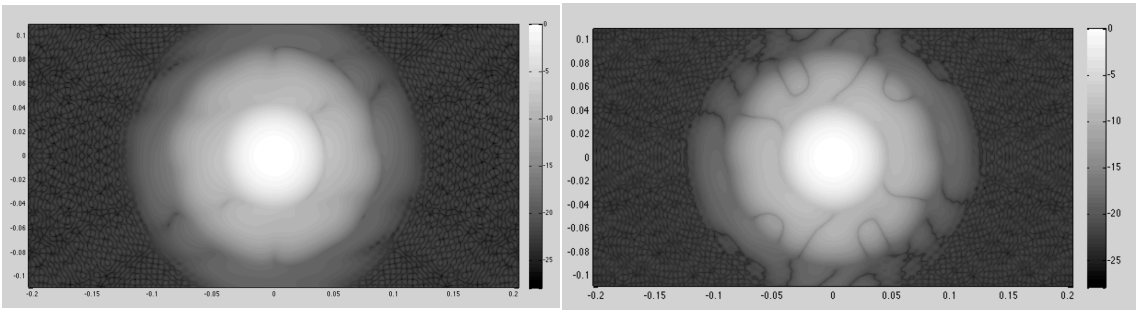

(a) (b)

Fig. 2.8. CCB XRD patterns with from 10 x 10 unit cell nanocrystal of PS Ⅱ with probe much smaller than unit cell. Convergence semi-angle θ_C=20mrad=9.09θ_B, defocus Δf=0Å, Gaussian cutoff σ=100Å. (a) probe at an asymmetric point of nanocrystal (b) probe at an inversion center of nanocrystal.

The extraction of structure factors from patterns with interference fringes requires collection of a large number of patterns with probe at random positions. Monte Carlo method averages the intensity of fringes with respect to probe coordinates. In case where only adjacent Bragg orders overlap such as shown in Fig. 2.6 and 7, intensity of fringes is expressed as (Cowley & Spence, 1981):

$$
\begin{aligned}
I_M &= \psi_M \psi_M^* \\
&= \left|(\psi_h \exp\{i\chi(u_h) + if(u_h)\} + \psi_g \exp\{i\chi(u_g) + if(u_g)\})\right|^2 \\
&= \left|\psi_h\right|^2 + \left|\psi_g\right|^2 + 2\left|\psi_h\right|\left|\psi_g\right|\cos(\chi(u_h) - \chi(u_g) + f(u_h) - f(u_g) + \Delta\theta) \\
&= \left|\psi_h\right|^2 + \left|\psi_g\right|^2 + 2\left|\psi_h\right|\left|\psi_g\right|\cos(\chi(u_h) - \chi(u_g) + 2\pi(u_h - u_g)x_P + \Delta\theta)
\end{aligned}
\tag{2.17}
$$

where ψ_h and ψ_g are amplitude contributions of h and g Bragg orders at the M point, χ represent the aberration of optic system and $f(u) = 2\pi u x$ is the probe position dependent phase shift. u is the spatial frequency and b is the lattice constant. Here, $\Delta\theta$ is the phase difference between ψ_h and ψ_g. For an arbitrary point M at the fringe region, the integration of Eqn. (2.17) with respect to probe coordinate x_P as the average will only keep the first two terms:

$$
\begin{aligned}
\overline{I_M} &= \left|\psi_h\right|^2 + \left|\psi_g\right|^2 + 2\left|\psi_h\right|\left|\psi_g\right| \frac{\int_{unit\ cell} \cos(\chi(u_h) - \chi(u_g) + 2\pi(u_h - u_g)x_P + \Delta\theta)\, dx_P}{\int_{unit\ cell} dx_P} \\
&= \left|\psi_h\right|^2 + \left|\psi_g\right|^2
\end{aligned}
\tag{2.18}
$$

Eqn. (2.18) indicates that Monte Carlo method averaging the interference fringes with respect to probe location will give us results exactly the same as the incoherent illumination case.

As shown in Eqn (2.17), the interference fringes in the overlap region between adjacent Bragg orders contain information on the phase differences of structure factors. Now we consider the extraction of phases from the CCBXRD patterns in an approach developed from conventional ptychography. Combined with other model-based phasing approaches such as molecular replacement, this ab-initio information can be used as strong

constraints to counteract potential model-biased effects in the phasing process. Ignoring all aberrations of the optical system other than the defocus effect, the phase term in the sinusoidal expression of the fringe intensity between overlapping Bragg orders shows a linear dependence on both probe position and the scattering angle, with the offset being the phase difference between the structure factors of the overlapping Bragg orders (Cowley & Spence, 1981). Since the fractional coordinate of the probe relative to the unit cell is random and vary from pattern to pattern, a common choice of phase origin must be used for all patterns. This can be achieved by summing up the phase differences along an enclosed triangle in a diffraction pattern to determine the relative probe position for each shot, because this sum only depends on the fractional coordinate of the probe. With corrected phase origin for each pattern, one can obtain the phase differences between each two Bragg orders that overlap in the pattern. Then, in cases of small protein molecules, phase invariants deduced from direct methods (Hauptman, 1997) as additional constraints along with the phase differences obtained above uniquely give the phases of all Bragg orders in low resolution region. Another issue in this phasing approach is the ambiguity in the sign of the phase difference $\Delta\theta$ as shown in Eqn. (2.17) due to the even cosine function. To resolve this ambiguity, different patterns with probe coordinates that differ by less than half of the lattice constant are compared. The increase or decrease of the intensity at the mid-point between Bragg disks determines the sign of $\Delta\theta$.

One remarkable feature of this phasing method is that the sensitivity of the interference

fringes to the probe position, hence the mechanical stability of the system is not a problem in the case of SFX.

Beam at edge of nanocrystal —— shadow image tells "impact parameter"

In XFEL diffraction experiments, a practical problem arises when the small convergent beam probe hits or approaches the edges of nanocrystals. To analyze the feasibility of extracting structure factors from diffraction patterns with probe at edges of nanocrystal, patterns are simulated as shown in Fig. 2.10 for four different probe positions indicated in Fig. 2.9. For probe at center of crystal (position A), clear and sharp Bragg disks form a reciprocal lattice array (Fig. 2.10 (a)). For pattern resulted with probe at edges of long and short sides of nanocrystal (position B and C), the Bragg disks are smeared in the direction perpendicular to the side which the probe is at (Fig. 2.10 (b) and (c)). For probe at the corner of nanocrystal, Bragg disks are smeared in both directions and cloud-like features occur in the pattern (Fig. 2.10 (d)).

Since the diffraction pattern and intensity of Bragg disks are sensitive to the probe position when the probe is approaching boundaries of nanocrystal, the ratio of intensity of first and second-order Bragg disks were calculated as the probe scans across the edges and compared to the ratio of corresponding structure factors. Fig. 2.12 shows plot of this ratio regarding (110) and (220) Bragg orders. Different convergence semi-angles from 1mrad to 4mrad were considered. It is found that in the cases where adjacent Bragg disks do not overlap ($\theta_C < \theta_B$=2.2mard), the ratio approaches its correct theoretical value 9.138

when probe is well within the crystal. As probe approaches the edges, the ratio deviates from the correct value. This deviation could be positive (greater than 9.138) and negative (less than 9.138) depending on the scanning direction. In Fig. 2.12 (a) where probe scans along a-axis, the ratio increases from 9.138 by less than 3% with beam approaching the edge at x_p=610Å. In Fig. 2.12 (b) where probe scans along b-axis, the ratio decreases by less than 10% at the edge. The convergence semi-angle seems to have an effect on the deviation of the ratio from the correct value when probe approaches the edges of nanocrystal. As shown in Fig. 2.12, the larger convergence, the larger the deviation.

For the cases where adjacent Bragg disks overlap (i.e. θC >θB=2.2mard), the ratio oscillates with probe scanning along b-axis as shown in Fig. 2.12 (b). This oscillation is resulted from the interference between overlapping Bragg orders and has a period of around 228 Å which is exactly the lattice constant of PS II nanocrystal. The periodicity of ratio oscillation is consistent with previous prediction by Eqn. (2.17). It is worthwhile to point out that though this oscillation is periodic and sinusoidal-like, it is not necessarily or rigorously sinusoidal. For convergence semi-angle 2.68mrad and 4mrad, the median value of the oscillating ratio of (110) and (220) Bragg disk intensity is approximately around the correct value. Extraction of structure factors is therefore possible based on Monte Carlo method averaging over large number of probe positions.

The proceeding discussions show that the Bragg reflection intensities deviate from the structure factors when the X-ray probe is close to the edges of nano-crystals, and

significantly in the case of large beam divergence. Hence, the extraction of structure factors by Monte-Carlo merging becomes invalid if the patterns from the "edge-hits" are merged towards the whole dataset. In order to reject these "edge-hit" patterns before the Monte-Carlo merging process so that to maintain the validity of the structure factor extraction, the concept "impact parameter" needs to be introduced which describes the relative position of the beam to the center of mass of the illuminated nano-crystal. Assigning a threshold value for the "impact parameter", the "edge-hits" that affect the merging quality can be distinguished from other events and rejected.

This rejection process can be implemented by a simple filter module, using the shadow image in Bragg disks in CCBXRD mode. Diffraction pattern simulation shows that the Bragg spots follow annular intensity distribution along with "spot splitting" when the X-ray probe spans the long edge of the nano-crystal (Fig. 2.10 (e)), which is consistent with earlier work for STEM imaging (Spence, 2010). The diffuse scattering due to partial breaking of the crystal periodicity smears the Bragg spots along the direction perpendicular to the edge where the probe spans(Fig. 2.10 (b)(c)(d)). The direction of diffuse scattering combined with the "spot-splitting" thus gives the orientation of the edge of the nanocrystal. This is also true for the cases where the probe is at the corner of the nano-crystal. In addition, the shadow image inside the Bragg orders shows the local shape of the nano-crystal around the beam at optimal beam defocus (Fig. 2.10 (f)), hence allows us to estimate the "impact parameter" for each hit event. Therefore, by analyzing

the intensity distribution of the Bragg orders in CCB diffraction patterns, the filter module is able to reject the patterns from "edge hit" events. This shadow image based estimate of "impact parameter" and "edge hit" rejection strategy also applies to single particle diffraction where "edge-hit" could be even a more significant issue.

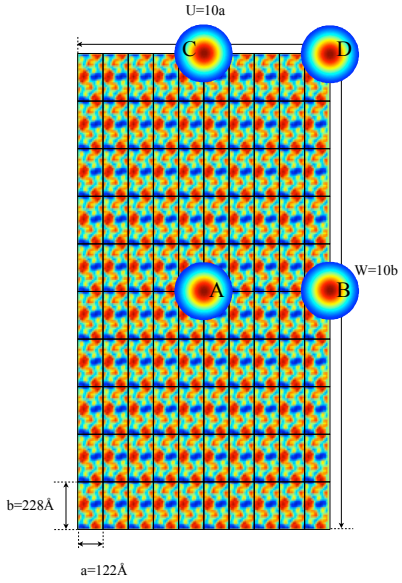

Fig. 2.9. Schematic diagram of probe positions relative to the nanocrystal. Black mesh grid indicate all unit cells that make up the nanocrystal. Probe was placed respectively at four different positions **A**, **B**, **C** and **D**.

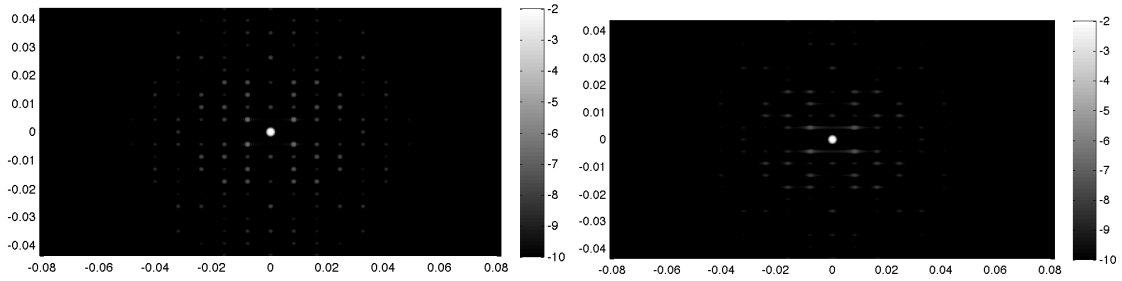

(a) (b)

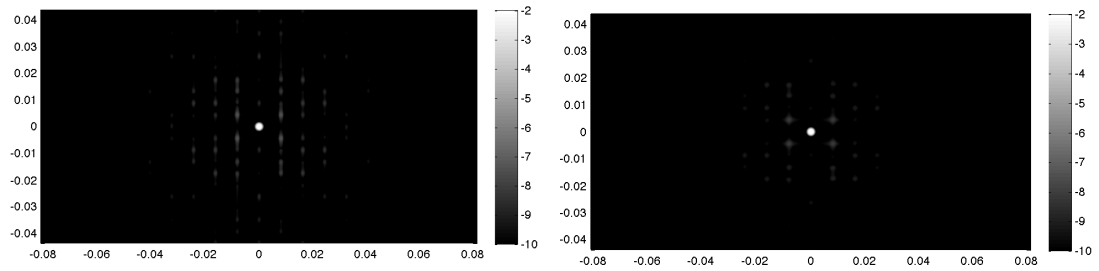

(c) (d)

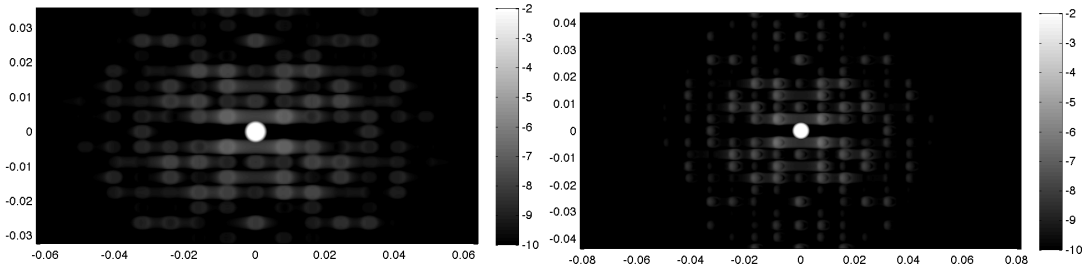

(e) (f)

Fig. 2.10. CCB XRD patterns from 10 x 10 unit cell nanocrystal of PS Ⅱ with probe locating at different positions. Convergence semi-angle θ_C=0.5mrad, defocus Δf=0Å, Gaussian cutoff σ=500Å. (a) probe at center (position **A** shown in Fig. 2.9) (b) probe at the edge on long side of nanocrystal (position **B**) (c) probe at the edge on the short side of nanocrystal (position **C**) (d) probe at corner of nanocrystal (position **D**). (e) θ_C=2mrad, Δf=0Å, Gaussian cutoff σ=500Å, probe at the long edge (f) $_C$=2mrad, Δf=-150000Å, Gaussian cutoff σ=500Å, probe at the long edge.

Extraction of structure factors by Monte Carlo method

To analyze the feasibility of structure factor extraction in all 3 cases, numerical

simulation f was conducted in Matlab environment (version R2013a). assuming an uniform random distribution of the probe positions. The distribution range was set to be a few unit cells larger than the nano-crystal size to enable the study of effect when the probe is scanning across the edge. For each of these randomly generated probe positions, probe intensity profile was evaluated according to the Bessel function described as Eqn. (2.9). Diffraction patterns were simulated under weak phase object approximation (WPOA) and by preforming Fourier transform to the exit wave function. For both Bragg orders (110) and (220) in each of these simulated patterns, intensities of all pixels within Bragg disks were summed up. These sums were then averaged over all patterns to obtain an estimate of structure factors of (110) and (220). Finally, to avoid the normalization problem, the ratio of (110) Bragg order intensity to (220) was taken as relative structure factor.

However, during the summation of intensities of all pixels within a Bragg disk for cases where adjacent Bragg disks overlap, an important question arises. That is, how do we handle the intensities of pixels in the overlap region: should they count towards one Bragg order or the other, or even both of them? Although Eqn. (2.18) shows that the average intensity of anbitrary point M in the overlap region over different probe positions is the sum of intensities of two adjacent Bragg orders at M, it is still necessary to split intensity of M point into contributions from two Bragg orders. Implementation of this will affect the relative structure factor extracted from Monte Carlo process. In this

simulation, relative structure factor was extracted based on Monte Carlo approach by both summing over whole Bragg disks (Fig. 2.12 (a)) and summing over only the non-overlap region (Fig. 2.12 (b)).

(a) (b)

Fig. 2.11. Two different ways of handling intensity in overlap region (red shaded area) between two adjacent Bragg disks. (a) sum over whole Bragg disks and intensity in overlap region counts towards both Bragg orders (implemented by script "MCconvergence1.m"); (b) sum over non-overlap areas within dashed circles (implemented by script "MCconvergence2.m").

To investigate the accuracy of structure factor extraction based on Monte Carlo approach and the speed of convergence, simulations were conducted using different parameters

including beam convergence angle from 1mrad to 4mrad, number of patterns from randomly generated probe positions up to 5000 and areas over which the intensity was summed over. Because generating probe function for a non-zero defocus value takes approximately 10 times the time for generating one for zero defocus, defocus parameter was set to be zero throughout the simulation process.

As Eqn. (2.17) shows, when the coherent convergent X-ray probe scans over the PS II nanocrystal, the intensity of fringes in the overlap region oscillates sinusoidally and the period is the lattice constant. To verify this prediction, ratio of (110) to (220) Bragg order intensity was computed as a function of the probe position for varying beam convergence semi-angles (Fig. 2.12(a) for scanning along a-axis; Fig. 2.12(b) for scanning along b-axis). For beam convergence 1mrad, 1.5mrad and 2mrad, which give non-overlap Bragg disks, this ratio was stable as the probe scanned along a-axis and was around its correct value of 9.138 (Fig. 2.12(a)). The ratio approached its correct value when probe was well within the nanocrystal but increased from 9.138 by less than 3% as beam got close to the edge at x_p=610Å. In Fig. 2.12(b), for beam convergence 1mrad, 1.5mrad and 2mrad corresponding to non-overlap disks, the ratio was maintained to be constant and very close to the correct value when the probe was not too close to the edge at y_p=1140Å. When probe got right at the edge, the ratio decreased by less than 10%. For the cases where adjacent Bragg disks overlap (i.e. θ_C =2.68mrad and 4mrad >θ_B=2.2mard), the ratio oscillated with probe scanning along b-axis as shown in Fig. 2.12 (b). This

oscillation is resulted from the interference between overlapping Bragg orders and has a period of 228 Å which is exactly the lattice constant of PS Ⅱ nanocrystal. The periodicity of ratio oscillation is consistent with previous prediction by Eqn. (2.17). Nevertheless, it is worthwhile to point out that though this oscillation is periodic and sinusoidal-like, it is not necessarily or rigorously sinusoidal. An obvious evidence is that the "crest" of the oscillating curve is sharper than the "trough" indicating the oscillation profile is not symmetric. For convergence semi-angle 2.68mrad and 4mrad, the median value of the oscillating ratio is around the correct value. Extraction of structure factors is therefore possible based on Monte Carlo approach averaging over large number of probe positions.

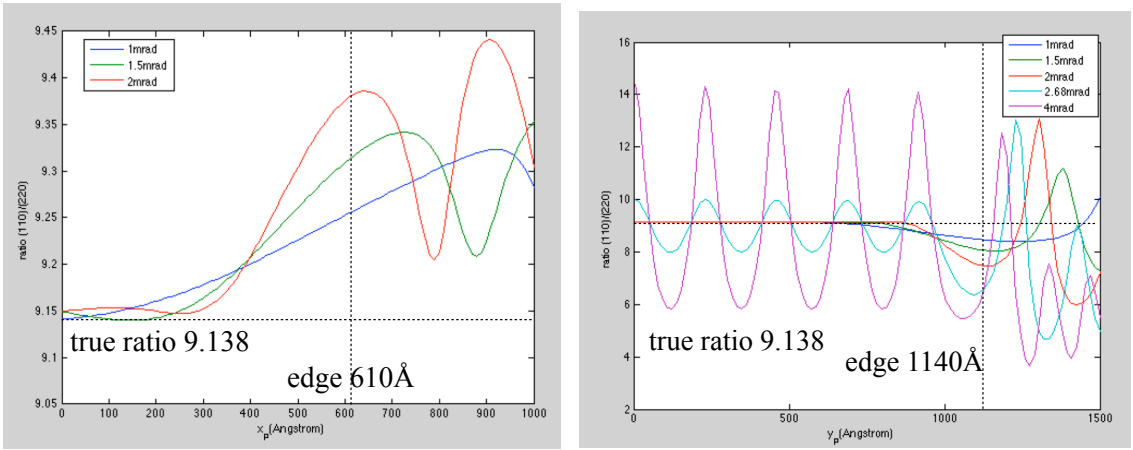

(a) (b)

Fig. 2.12. Ratio of total intensity within (110) to (220) Bragg disks as a function of beam

position as it scans from the center of nanocrystal (x_p=0Å, y_p=0Å) to the edge. The ratio approaches the correct value 9.138 when the beam is well within the crystal. (a) probe scans along the a-axis direction from center (x_p=0Å) and across the edge (x_p=610Å), convergence semi-angle was set to be θ_C=1mrad, 1.5mrad and 2mrad, Gaussian cutoff σ=500Å. (b) probe scans along the b-axis direction from center (y_p=0Å) and across the edge (y_p=1140Å), convergence semi-angle was set to be θ_C=1mrad, 1.5mrad, 2mrad, 2.68mrad and 4mrad, Gaussian cutoff σ=500Å.

Assuming uniform distribution for probe position, diffraction patterns were simulated and ratio of (110) to (220) Bragg order intensity was calculated based on Monte Carlo method that averages over all patterns resulted from different random probe positions. We conducted the simulation in both ways of handling the intensity in overlap region (Fig. 2.11). Various beam convergence semi-angles 1mrad, 1.5mrad, 2mrad, 2.68mrad and 4mrad were considered. In cases where no Bragg orders overlap, the ratio converges to correct value 9.138 with errors less than 0.5% from 10000 patterns. For cases where Bragg disks overlap (2.68mrad and 4 mrad), the ratio converges to a particular value that deviates from the correct value as in Fig. 2.13 (b). This deviation can be attributed to the non-sinusoidal oscillation and the considerable contribution from intensity of the overlap region and the way it was processed. Fortunately, as long as the beam convergence is kept sufficiently small, Monte Carlo method gives an averaged ratio with a tolerable error which is good enough for estimate purpose. For example, convergence semi-angle of

2.68mrad provides an estimate of relative structure factor within 1.5% error from 10000 patterns.

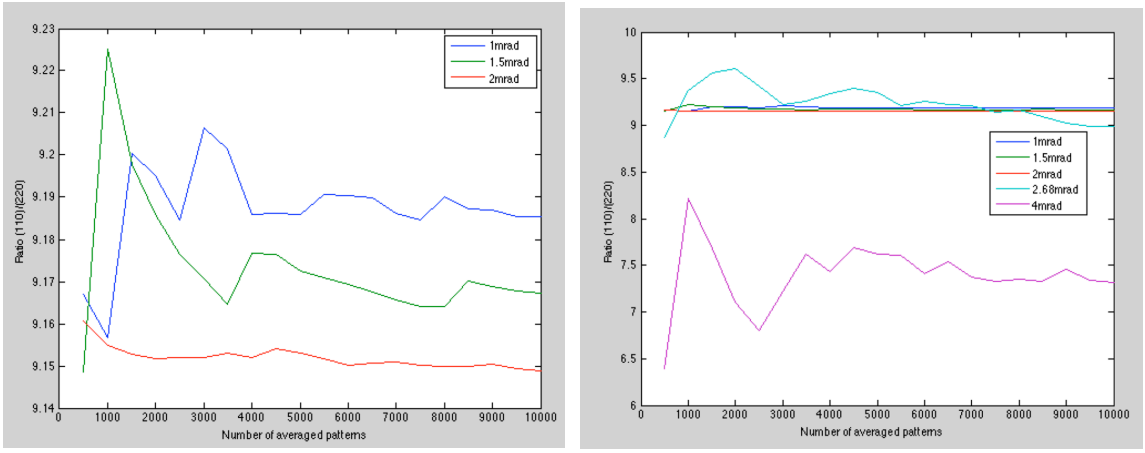

(a) (b)

Fig. 2.13. Monte Carlo averaged ratio of (110) to (220) Bragg order intensity as function of number of patterns (in the way shown in Fig. 2.11(a)). Defocus Δf=0Å, Gaussian cutoff σ=500Å, uniform distribution of probe position assumed. (a) Convergence semi-angle θ_C =1mrad, 1.5mrad and 2mrad ($<\theta_B$=2.2mard, no overlap) (b) Convergence semi-angle θ_C =1mrad, 1.5mrad, 2mrad, 2.68mrad and 4mrad.

Fig. 2.14 shows the plot of change of averaged ratio every when 500 additional patterns are taken into use versus number of patterns. Among beam convergence of 1mrad, 1.5mrad and 2mrad considered, larger convergence results in faster convergence speed of Monte Carlo process. However, when beam convergence is larger than Bragg angle,

accuracy of structure factor extraction and convergence speed of Monte Carlo process is largely dependent on how the intensity contribution from the overlap region is handled.

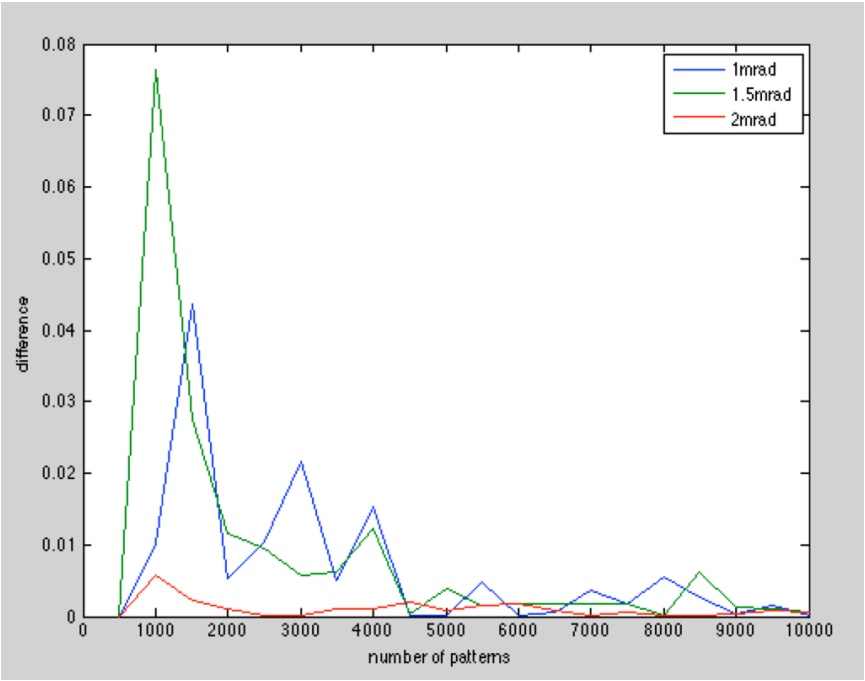

Fig. 2.14. Change of averaged ratio every time another 500 patterns were added into use as function of number of patterns used with beam convergence of 1mrad, 1.5mrad and 2mrad. Larger beam convergence promotes convergence of Monte Carlo average process.

Although Monte Carlo approach based on summing up intensity over whole Bragg disks (Fig. 2.11(a)) provided an accurate estimate of relative structure factor when adjacent disks overlap by a small amount (Fig. 2.13(b), 2.68mrad), extraction of structure factors is not considered accurate when beam convergence got larger and disks overlapped more (Fig. 2.13(b), 4 mrad). As an alternative, Monte Carlo simulation was again conducted

based on summing up intensity over the non-overlap areas of Bragg disks (Fig. 2.11(b)). To investigate the effect of the way we handle the overlap region, ratio of (110) to (220) Bragg order intensity was computed as a function of probe position and then accuracy as well convergence speed of relative structure factor extraction were computed.

In order to see how different ways of handling the intensity of the overlap region affect extraction of structure factors, the ratio of (110) to (220) Bragg order intensity as function of probe position computed in both ways as indicated in Fig. 2.11(a) and (b) are shown in comparison (Fig. 2.15). Similar oscillation behavior of the ratio value with the probe scanning in the b-axis direction was observed for both ways. However, compared to Fig. 2.15(a) the amplitude of this oscillation was obviously smaller in Fig. 2.15(b) and the profile of the curve seemed much more symmetric offering us a possibility of structure factor extraction with a better accuracy.

Relative structure factor was estimated based on Monte Carlo approach for beam divergence of 2.68mrad and 4mrad in the way shown in Fig. 2.11(b) and convergence speed was shown (Fig. 2.16). In contrast with the result shown in Fig. 2.13(b), our estimated value of relative structure factor was approximately from 9.0 to 9.1 which is much more accurate than that obtained from the way indicated by Fig. 2.11(a). The convergence speed of this Monte Carlo process was characterized by the change of relative structure factor every 500 more patterns were taken into use. In the cases where we have overlap Bragg orders and extract the relative structure factor summing up the

intensity only over the non-overlap areas, smaller beam convergence yielded result closer to the true value 9.138 and faster convergence speed.

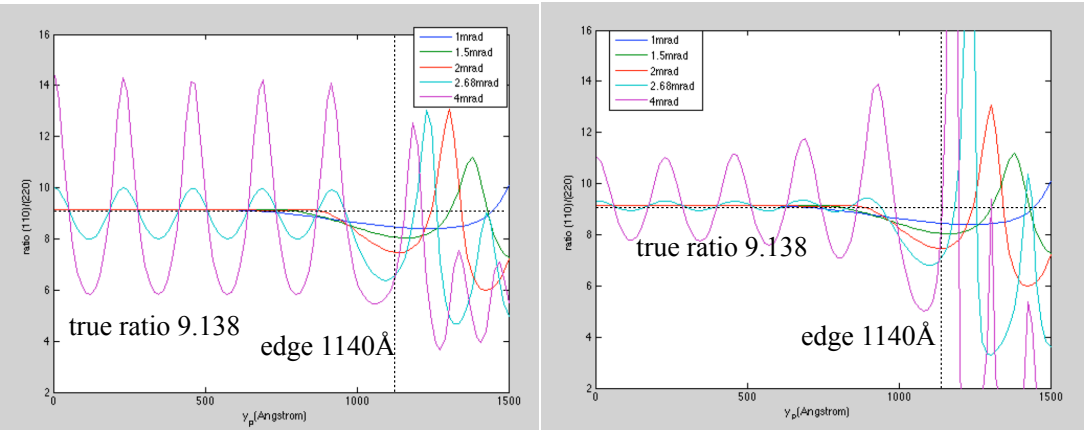

(a) (b)

Fig. 2.15. Ratio of total intensity within (110) to (220) Bragg disks as a function of beam position as it scans from the center of nanocrystal (x_p=0Å, y_p=0Å) to the edge, scanning in the b-axis direction. (a) summing up intensity over whole Bragg disks (Fig. 2.11(a)); (b) summing up intensity over non-overlap region of Bragg disks (Fig. 2.11(b)).

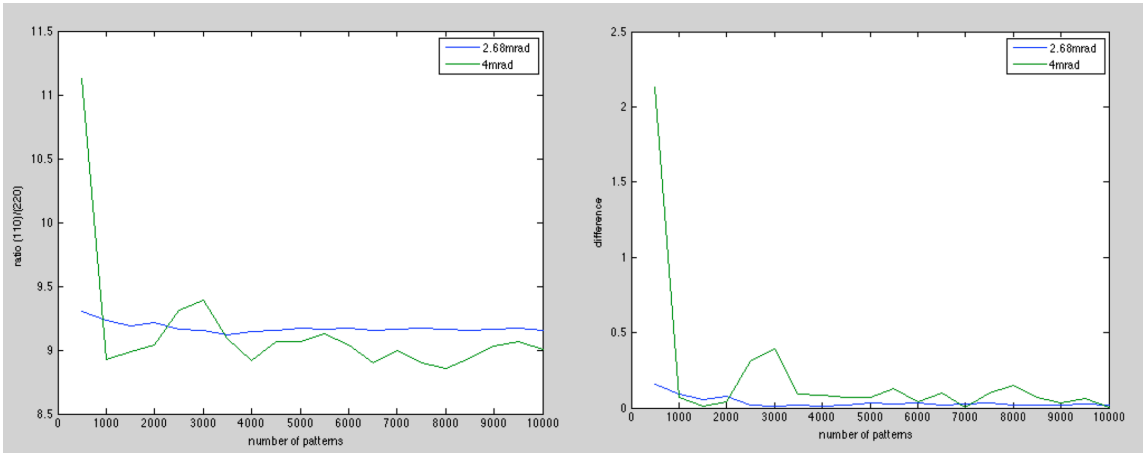

(a) (b)

Fig. 2.16. (a) Monte Carlo averaged ratio of (110) to (220) Bragg order intensity as

function of number of patterns (in the way shown in Fig. 2.11(b)). Defocus Δf=0Å, Gaussian cutoff σ=500Å, uniform distribution of probe position assumed. (b) Change of averaged ratio every time another 500 patterns were added into use as function of number of patterns used with beam convergence of 2.68mrad and 4mrad.

Conclusions

This work discussed possibility of coherent convergent beam X-ray microdiffraction (CCB XRD) from nanocrystals which may find its use in time-resolved crystallography and structural biology. To overcome the difficulty of Laue mode implementation in traditional monochromatic illumination provided by XFELs and disadvantage that huge number of diffraction patterns are need to determine the structure of crystal, CCB configuration was considered and expected to give intensity of all points of shape transform at the same time with a single shot. Diffraction patterns from 10×10×10 unit cell PS II nanocrystal were simulated under projection approximation with beam along c-axis in three different cases: beam larger than nanocrystal, beam smaller than nanocrystal but larger than unit cell and beam smaller than single unit cell. Spatial resolution limit was set to be 20Å according to projection approximation. For case where beam much larger than nanocrystal, shape transforms are clearly observed in the simulated diffraction pattern. When beam is smaller than nanocrystal but larger than unit

cell, Bragg disks with no apparent shape transforms are seen in simulated patterns. Extraction of structure factors is simply implemented by angular integration over these disks. As the beam gets smaller than single unit cell, Bragg disks start to overlap which produces interference fringes in the overlap regions. These fringes are shadow images of lattice of nanocrystal, and depend sensitively on the probe coordinate. As the beam convergence gets even larger, periodicity of diffraction pattern vanishes and point group symmetry of nanocrystal with respect to the scanned point is reflected. Together with lattice images, a new lensless X-ray imaging technique similar to STEM is indicated.

Extraction of structure factors based on Monte Carlo method was also discussed in cases where the probe is at edges of nanocrystal, and where adjacent Bragg orders overlap. Ratio of (110) to (220) Bragg order intensity was simulated as function of probe position and number of diffraction patterns. For beam convergence less than Bragg angle, this ratio approaches its correct value when probe is well within the nanocrystal and deviates by less than 10%. Results show that larger beam convergence with non-overlapping Bragg orders yields more accurate structure factors and faster convergence of Monte Carlo average over probe positions. With convergence larger than Bragg angle, ratio of (110) to (220) oscillates in a sinusoidal-like manner and gives structure factors slightly deviated from the correct value using Monte Carlo average. This can be improved by refined processing of intensity contribution from the interference region between Bragg orders. For “edge-hit” events, the shadow image inside Bragg disks can be used to

estimate the “impact parameter” for each pattern. A filter software module can be devised to reject “edge-hit” patterns from later merging process to improve the final quality of structure factor measurement.

An ab-initio phasing approach based on the interference fringes between overlapping Bragg disks is discussed. This ab-initio information combined with other traditional phasing approaches including both algorithmic, such as Hybrid Input and Output (HIO) and model-based, such as molecular replacement, can advance the phasing capability and push the resolution for SFX.

CHAPTER 3

TWO-COLOR DIFFRACTION SCHEME AND COMPARISON BETWEEN DIFFERENT DIFFRACTION METHODS FOR DATA COLLECTION STRATEGIES

Introduction

In recent experiments aimed at the measurement of structure-factors using a free-electron laser (XFEL) (Spence et al., 2012), protein nanocrystals are sprayed in single-file across a pulsed hard-X-ray beam, using a technique known as serial femtosecond X-ray diffraction (SFX). The crystals, often of submicron dimensions, vary in size, are randomly oriented, and are destroyed by the beam after providing a high-resolution diffraction pattern. In addition, the intensity of the X-ray beam may vary from shot to shot by up to 15%, and the time-structure of the femtosecond pulses used also varies from shot to shot. Diffraction patterns are read out at perhaps 120 Hz, so that large amounts of data are collected. Nevertheless, using improved data analysis methods, the number of diffraction patterns needed to determine a structure at better than 0.2 nm resolution has recently been reduced to less than 6000 (Ginn et al., 2015). The extraction of structure factors then requires integration across the angular width of the Bragg reflections from these many "stills", snapshots, or partial reflections, in each of which the Ewald sphere cuts through a small slice of the intensity distribution around each Bragg condition. For the smallest nanocrystals, containing perhaps just a few dozen unit cells,

since the XFEL is spatially coherent, and assuming that the beam is wider than the crystal, the Bragg spots are broadened by "shape transform" functions(Kirian et al., 2010; Spence et al., 2012); for larger crystals mosaicity may be present (Hattne et al., 2014). The case of a coherent beam smaller than the crystal (or smaller than one mosaic block, or unit cell) is discussed elsewhere (Spence et al., 2014). Where a wide beam illuminates a mosaic crystal, slightly tilted blocks of crystal monochromate different component wavelengths of the beam, scattering them into slightly different directions around the Bragg spots, across which an integration is required. The divergence of the incident beam and the energy-spread in the beam must also be considered, since these contribute to the "thickness" of the Ewald sphere. These considerations lead to the well-established multiple-scattering theory of primary and secondary extinction in mosaic crystals (Zachariasen, 1967), which assumes incoherent multiple scattering between blocks but coherent multiple scattering within each block. We do not consider that here, since a modern XFEL coherent beam diameter of 200nm is comparable with a typical mosaic block size, and the mosaic block model may not apply to layer structures such a membrane proteins (Snell et al., 2003). In all cases, the precise deviation of the diffraction conditions from the ideal Bragg condition is needed for each spot in every shot in order to estimate the degree of partiality for each reflection. So far is has not been possible to measure this quantity directly, however several groups have recently used optimization methods to estimate partiality (Hattne et al., 2014; White, 2014).

Building on earlier synchrotron work [21], pump-probe SFX experiments (Aquila et al., 2012; Kupitz et al., 2014; Tenboer et al., 2014), have also been undertaken, aimed at imaging time-resolved changes (TR-SFX) in three-dimensional protein charge-density maps due to optical illumination, such as that which occurs in photosynthesis. In a typical experiment, alternate nanocrystals in a liquid jet stream might be illuminated optically (causing a change in structure factors) and the difference in the measured intensities between illuminated (bright) and un-illuminated (dark) angle-integrated Bragg reflections are used, after phasing, to provide a real-space density map showing the change in molecular structure due to illumination. The differences are taken between a very large number of bright and dark nanocrystals of different sizes (leading to large scale-factor differences covering orders of magnitude). In this chapter we obtain expressions for the number of patterns needed to reduce the errors in structure factor measurement to below that needed to observe optical pumping effects, using three different methods, which we compare.

In order to merge data (by adding together Bragg partial reflections with the same Miller indices from nanocrystals of different sizes), subject to these many sources of stochastic variation, it was suggested that the only reasonable method is a Monte Carlo type of angular integration across the Bragg reflections, in which the angular coordinate then consists of a random sample of abscissa (crystal orientation) values. This integration will then average over all stochastic fluctuations, such as shot-to-shot beam intensity

variation and differences in crystal size. The contributions of these fluctuations to the final structure factor measurement might then be expected to add in quadrature, giving a signal-to-noise ratio (SNR) which improves as the square root of the number of diffraction patterns, and this behavior has been confirmed experimentally (Kirian et al., 2011). Thus a hundred times more data are needed to add one significant figure to the results. Improvements on this behavior require experimental characterization of the sources of error and their distributions and more accurate specification of experimental parameters, such as the assignment of a scattering vector to each pixel on the area detector and deviation from the exact Bragg condition. Model-based data analysis methods using the EMC algorithm also show great promise for the smallest crystals (Ayyer et al., 2014)

More recently we have been involved with experiments in which data are collected from larger crystals in a fixed orientation mounted on a goniometer, with provision to scan the sample to a new position laterally. For pump-probe experiments, the incident X-ray intensity can be adjusted for either destructive readout (in which case the sample must be translated after each shot has drilled a hole in the sample) or defocussed to a level below the damage threshold, giving poorer statistics (Frank et al., 2014; Stevenson et al., 2014). In principle this method allows measurements at equally spaced increments across the rocking curve, with a known abscissa error, however the total dose for all exposures must fall below the Henderson safe dose (Henderson, 1995) .

Finally, new modes of XFEL operation have been demonstrated, dubbed "split and delay", in which the coherent X-ray beam is split into two beams of slightly different wavelengths, with the femtosecond pulse in one beam delayed relative to the other (Lutman et al., 2013; Spence, 2014; Zhu et al., 2012). Several methods are possible including a "slotted foil", the use of mirrors (for softer X-rays with high efficiency) and Bragg crystal splitters (harder X-rays with lower efficiency). The two beams can be focused onto the same sample, arriving at slightly different times and beam energies, or from slightly different directions at the same energy. Delays are currently in the range of 100 femtoseconds, but could in principle be extended to the range more useful for biology or organic chemistry (with very long path lengths), in which case a pump laser could be inserted between the two pulses of a pair, and both diffraction patterns then impressed on the same detector readout. For larger nanocrystals, the sharp partial Bragg spots at the two slightly different beam energies will then be displaced on the detector, and the intensity differences merged to provide a difference density map after phasing. By obtaining pairs of diffraction patterns from the *same* nanocrystal (before and after optical illumination), errors due to both size and orientation variation are eliminated, however the first pulse must clearly not destroy the sample, resulting in poorer SNR relative to the diffract-and-destroy mode. Among the methods developed at LCLS for split-and-delay research, different limitations apply. Use of mirrors limits the X-ray energy to below 2 keV and a short time delay, thus cannot provide high-resolution

reflections needed for biological imaging. Bragg crystals used as beam splitters result in excessively collimated and monochromatic pulses giving low efficiency in structure factor measurement. Similarly, a two-color scheme based on use of two sets of undulators generates two X-ray pulses at slightly different energies (2% difference) and separated in time with an adjustable delay up to 40fs, potentially extendable to up to 200fs (Lutman et al., 2013). This two-color approach, which is also applicable to hard-X-rays with time delay from a few femtoseconds up to 200fs, is most suitable for the study of the earliest stages of conformational change and bond formation in biochemistry. We therefore focus our analysis and discussion on these two-color approaches in the following sections.

In this chapter we compare the accuracy of structure factor measurement for each of these modes for pump-probe time-resolved diffraction experiments, in which the error should be less than the changes in structure factor due to pump illumination. Since many poorly-characterized experimental factors influence such a complex comparison (such as crystal quality, jet hit rate, sample concentration and fixed-sample scan time) we make here a simplified comparison which focuses on establishing signal-to-noise ratio as a function of number of shots for each method, with other factors equal. Some of the many additional experimental considerations might include the following. For irreversible processes, the pump laser must be directed to a new area (or crystal) for each shot. Since Laue diffraction is not possible using an XFEL, many shots (both bright and

dark) are needed in the vicinity of every Bragg condition to perform the required angular integration over these partial reflections. With many pixels within the angular profile of the Bragg reflection, the intensity of these partial reflections is proportional to the square of the number of electrons in the illuminated region of the sample, while the angle-integrated intensity is proportional to the number of electrons or molecules. A doubling of beam size on a large crystal by defocus (with constant number of photons per shot) leaves the intensity of Bragg beams unchanged (in the absence of damage). The ideal maximum of diffraction information is obtained with the largest possible ideally imperfect crystal fully illuminated at a level below the Henderson safe dose. (This maximizes the number of undamaged molecules contributing to the diffraction pattern). The use of diffract-and-destroy methods allows a dose of up to 100 times this safe dose without damage, in principle providing much more intense high angle scattering and so better resolution, with data obtained from submicron regions of crystals, in some cases thereby reducing the contribution from defects.. The use of femtosecond pulses allows us to outrun radiation damage effects at all beam intensity levels (including low intensity), while subsequent vaporization of the crystal at high intensities prevents the collection of pumped data from the same crystal. The theory of diffraction from protein nanocrystals is given elsewhere[5]; the theory of diffraction from larger mosaic crystals is given in textbooks (Zachariasen, 1967).

XFEL-based approaches for structure factor measurement

A. Monte-Carlo approach

The Monte-Carlo (MC) approach[5] merges all diffraction data from many crystal sizes and sample orientations. For different patterns, the Ewald sphere intersects the Bragg orders in reciprocal space at different points on the intensity distribution. The intensity of the reflection is thus dependent on the crystal size and orientation and can be expressed as (Kirian et al., 2010):

$$I^{(i)} = I_0^{(i)} \left|F(\Delta\mathbf{k})\right|^2 r_e^2 P(\mathbf{k_0}) \frac{\sin^2(N_1^{(i)}\Psi_1^{(i)})}{\sin^2(\Psi_1^{(i)})} \frac{\sin^2(N_2^{(i)}\Psi_2^{(i)})}{\sin^2(\Psi_2^{(i)})} \frac{\sin^2(N_3^{(i)}\Psi_3^{(i)})}{\sin^2(\Psi_3^{(i)})} \Delta\Omega \tag{3.1}$$

where N(i)'s represent the number of unit cells in a given dimension (hence crystal size), and

$$\Psi_1^{(i)} = \pi\Delta\mathbf{k}\cdot\mathbf{a}^{(i)} \; ; \; \Psi_2^{(i)} = \pi\Delta\mathbf{k}\cdot\mathbf{b}^{(i)} \; ; \; \Psi_3^{(i)} = \pi\Delta\mathbf{k}\cdot\mathbf{c}^{(i)} \tag{3.2}$$

The superscript index "(i)" indicates the "i"th shot event. $a^{(i)}$,$b^{(i)}$ and $c^{(i)}$ are the lattice vectors of the nano-crystal in the frame fixed to the laboratory at the "i"th shot. The extracted structure factor is estimated from the average intensity of the Bragg beam over all shots with index $^{(i)}$:

$$\left\langle I^{(i)} \right\rangle = \left\langle I_0^{(i)} \left|F(\Delta\mathbf{k})\right|^2 \frac{\sin^2(N_1^{(i)}\Psi_1^{(i)})}{\sin^2(\Psi_1^{(i)})} \frac{\sin^2(N_2^{(i)}\Psi_2^{(i)})}{\sin^2(\Psi_2^{(i)})} \frac{\sin^2(N_3^{(i)}\Psi_3^{(i)})}{\sin^2(\Psi_3^{(i)})} \right\rangle r_e^2 P(\mathbf{k_0}) \Delta\Omega$$

$$\approx \left\langle I_0^{(i)} \right\rangle \left|F(\Delta\mathbf{k})\right|^2 \left\langle \frac{\sin^2(N_1^{(i)}\Psi_1^{(i)})}{\sin^2(\Psi_1^{(i)})} \frac{\sin^2(N_2^{(i)}\Psi_2^{(i)})}{\sin^2(\Psi_2^{(i)})} \frac{\sin^2(N_3^{(i)}\Psi_3^{(i)})}{\sin^2(\Psi_3^{(i)})} \right\rangle r_e^2 P(\mathbf{k_0}) \Delta\Omega$$

$$\approx \left\langle I_0^{(i)} \right\rangle \left|F(\Delta\mathbf{k})\right|^2 \left\langle \frac{\sin^2(N_1^{(i)}\Psi_1^{(i)})}{\sin^2(\Psi_1^{(i)})} \right\rangle \left\langle \frac{\sin^2(N_2^{(i)}\Psi_2^{(i)})}{\sin^2(\Psi_2^{(i)})} \right\rangle \left\langle \frac{\sin^2(N_3^{(i)}\Psi_3^{(i)})}{\sin^2(\Psi_3^{(i)})} \right\rangle \times r_e^2 P(\mathbf{k_0}) \Delta\Omega$$

(3.3)

If we use $C_{(hkl)}^{(i)}$ to denote the combined effect of crystal size, orientation and other constants, then Eqn. (3.3) can be written in the following form:

$$I^{(i)} = I_0^{(i)} \left|F(\Delta\mathbf{k})\right|^2 \cdot C_{(hkl)}^{(i)} \tag{3.4}$$

$$C_{(hkl)}^{(i)} = \left(\frac{\sin^2(N_1^{(i)}\Psi_1^{(i)})}{\sin^2(\Psi_1^{(i)})} \frac{\sin^2(N_2^{(i)}\Psi_2^{(i)})}{\sin^2(\Psi_2^{(i)})} \frac{\sin^2(N_3^{(i)}\Psi_3^{(i)})}{\sin^2(\Psi_3^{(i)})} \right) r_e^2 P(\mathbf{k_0}) \Delta\Omega \tag{3.5}$$

$$\left\langle I^{(i)} \right\rangle = \left\langle I_0^{(i)} \right\rangle \left|F(\Delta\mathbf{k})\right|^2 \left\langle C_{(hkl)}^{(i)} \right\rangle \tag{3.6}$$

The structure factors can then be estimated from the average Bragg beam intensity using the following relation:

$$\left|F_{(hkl)}^{\exp}\right|^2 = \frac{\left\langle I^{(i)} \right\rangle}{\left\langle I_0^{(i)} \right\rangle \left\langle C_{(hkl)}^{(i)} \right\rangle} \tag{3.7}$$

where $\left\langle C_{(hkl)}^{(i)} \right\rangle$ includes the average shape transform, which can be modeled, based on experimental parameters. As shown elsewhere[23], this average shape transform is a smooth curve, rather than the sinc-function profile of a single cubic nano-crystal.

B. Two-color approach for pump-probe experiments.

The two-color approach offers the possibility of eliminating the randomness of several stochastic variables, as shown below. The first of a pair of pulses hits a nano-crystal and, after a set time delay, the second hits the same crystal in an identical orientation, since the rotational diffusion time of micron-sized microcrystals in solution is much larger than the delay. Between these two pulses, the crystal may be pumped optically, however the first X-ray pulse must not cause damage, and if it excites the crystal, sufficient time must be allowed for the excitation to decay before optical pumping. Both patterns are recorded by the detector within the same read-out event. Since the two patterns are from two pulses with slightly different wavelengths, they can be separated in data analysis, if the crystals are large enough to minimize overlap of the diffraction spots at the two wavelengths. Since the two diffraction patterns are from almost the same scattering geometry, the intensities may be expressed as:

$$I_{1,(hkl)}^{(i)} = I_{01}^{(i)} \cdot \left|F_{1,(hkl)}\right|^2 \cdot C_{1,(hkl)}^{(i)} \tag{3.8}$$

$$I_{2,(hkl)}^{(i)} = I_{02}^{(i)} \cdot \left|F_{2,(hkl)}\right|^2 \cdot C_{2,(hkl)}^{(i)} \tag{3.9}$$

$$C_{1,(hkl)}^{(i)} \approx C_{2,(hkl)}^{(i)} \tag{3.10}$$

where the indices "$_1$" and "$_2$" indicates the first and the second of the paired pulses, or ground state and excited state. As can be seen from Eqn. (3.8) – (3.10), the beauty of the two-color approach is that we can divide out the common orientation factor to obtain the change in structure factor amplitude:

$$R_{(hkl)}^{(i)} = \frac{\Delta\left(\left|F_{(hkl)}\right|\right)}{\left|F_{1,(hkl)}\right|} = \left|\frac{\left|F_{2,(hkl)}\right| - \left|F_{1,(hkl)}\right|}{\left|F_{1,(hkl)}\right|}\right|$$

$$= \sqrt{\frac{\left|F_{2,(hkl)}\right|^2}{\left|F_{1,(hkl)}\right|^2}} - 1 = \sqrt{\frac{I_{2,(hkl)}^{(i)}}{I_{1,(hkl)}^{(i)}} \cdot \frac{I_{01}^{(i)}}{I_{02}^{(i)}}} - 1 \tag{3.11}$$

$$= \sqrt{\frac{I_{2,(hkl)}^{(i)}}{I_{1,(hkl)}^{(i)}} \cdot k_{12}^{(i)}} - 1 = \sqrt{A_{(hkl)}^{(i)}} - 1$$

$$k_{12}^{(i)} \equiv \frac{I_{01}^{(i)}}{I_{02}^{(i)}}; A_{(hkl)}^{(i)} \equiv \frac{I_{2,(hkl)}^{(i)}}{I_{1,(hkl)}^{(i)}} \cdot k_{12}^{(i)} \tag{3.12}$$

where $k_{12}^{(i)}$ denotes the ratio of the first pulse intensity to the second for the (i)th shot. The ratio of the change in Bragg beam intensity is independent of crystal size and orientation. It is equal to the ratio of change in the squared structure factor magnitudes. Experimentally, this means that each frame from paired pulses which contains two slightly displaced diffraction patterns gives exactly the same ratio of the change in the Bragg beam intensity. The randomness in crystal size and orientation is therefore eliminated, suggesting that this two-color approach might be superior to a Monte-Carlo approach. However, the weak signal from the first pulse (needed to avoid damaging the sample) degrades SNR.

C. Large crystal fixed on a goniometer

For fixed-sample experiments, the sample orientation can be controlled using a goniometer to allow a slow scan across reflections from a large single crystal at controlled increments for both bright and dark conditions. The total dose deposited in the

sample must be lower the Henderson safe dose to obtain damage-free data. If the diffract-and-destroy mode is used (drilling holes with the beam in a large crystal) the many orientations and bright and dark conditions must all be obtained from different regions of the same crystal, separated by several microns to allow for the range of damage and strain caused by hole-drilling. This approach has the advantage of allowing a much higher dose (Redecke et al., 2013) (with resulting stronger high-angle scattering) and the absence of radiation damage on the Bragg data. A third possibility uses microcrystals trapped, perhaps by filtration, on the sites of a calibrated lattice in random orientations. Then, under diffract-and-destroy conditions, bright and dark data are collected from different microcrystals, and the methodology is similar to the GDVN liquid jet, but with a hit rate approaching 100% and possibly slower readout, depending on scan speed. If a goniometer and large crystal is used (either above or below the damage threshold), the extracted structure factor from a series of exposures around Bragg conditions is

$$\begin{aligned} \left|F_{es}\right|^2 &= \sum_{i=1}^{N_s}\left(I_i \cdot \Delta\Psi\right) \\ &= \Delta\Psi \sum_{i=1}^{N_s} I_i \\ &= \Psi_T \frac{\sum_{i=1}^{N_s} I_i}{N_s} \end{aligned} \tag{3.13}$$

where Ψ_T is the effective angular width of the abscissa of Bragg reflection that is

scanned across and $\Delta\Psi$ is the sampling increment of the scanning process. I_i is the measured intensity of the ith sampled point, and N_s is the number of sampling points across the reflection.

Error metrics

In order to determine if the two-color (or split-and-delay) approach is more accurate than the Monte- Carlo method, the errors in structure factor extraction are estimated below for both approaches. In addition, we determine approximately the number of patterns needed to achieve a given accuracy in structure factor, and whether it is feasible for both approaches, with a 15% beam intensity fluctuation, to identify a 1% change in structure factors.

A. Monte-Carlo approach

The extracted structure factor converges to its true value by Monte-Carlo integration over crystal size, orientation and beam intensity fluctuation (Kirian et al., 2011). This convergence has a diminishing efficiency described by error reduction as $1/\sqrt{N}$, which makes Monte-Carlo approach wasteful of protein sample and beam resources. For the study of radiation damage dynamics or sub-pico-second time-resolved imaging, the change in structure factor is very small and likely to be less than 10 % at best, and 1% in some cases. To recognize this small change from random errors, a huge number of patterns may be needed; nevertheless near-atomic resolution " movies" of the

photo-detection cycle in photo-sensitive bacterial yellow protein have recently produced by this approach[20]. In the following, we estimate this number based on error analysis.

The error in structure factor from each shot can be derived from Eqn. (3.7) based on error propagation as (Bevington & Robinson, 1992):

$$\frac{\sigma_{MC}^{(i)}\left(|F|\right)}{\left\langle |F| \right\rangle} = \frac{1}{2}\sqrt{\left(\frac{\sigma\left(I^{(i)}\right)}{\left\langle I^{(i)} \right\rangle}\right)^2 + \left(\frac{\sigma\left(C^{(i)}\right)}{\left\langle C^{(i)} \right\rangle}\right)^2 + \left(\frac{\sigma\left(I_0^{(i)}\right)}{\left\langle I_0^{(i)} \right\rangle}\right)^2} \tag{3.14}$$

where "σ" denotes the error (or standard deviation) in each random variable and "<>" represents the average value. After merging N patterns by Monte-Carlo integration over crystal size and orientation, the error in the structure factor is reduced by a factor of $1/\sqrt{N}$:

$$\frac{\sigma_{MC}^{(N)}\left(|F|\right)}{\left\langle |F| \right\rangle} = \frac{1}{2\sqrt{N}}\sqrt{\left(\frac{\sigma\left(I^{(i)}\right)}{\left\langle I^{(i)} \right\rangle}\right)^2 + \left(\frac{\sigma\left(C^{(i)}\right)}{\left\langle C^{(i)} \right\rangle}\right)^2 + \left(\frac{\sigma\left(I_0^{(i)}\right)}{\left\langle I_0^{(i)} \right\rangle}\right)^2} \tag{3.15}$$

If we now neglect the error in intensity detection due to shot noise for a relatively strong Bragg beam, then the first term in the parenthesis in Eqn. (3.15) vanishes. Also, for the purpose of approximation, a Monte-Carlo simulation has been conducted to obtain the approximate percentage error (ratio of standard deviation to mean) in the $C^{(i)}$ factor, which represents the effect of crystal shape and orientation. For crystals of Trypanosoma brucei cysteine protease cathepsin B (TbCatB) used recently (Redecke et al., 2013), the value of the relative error in $C^{(i)}$ was found to be 5.7 for micocrystals of 0.9×0.9×11μm

average size and 10% deviation, with Gaussian distribution (see Appendix A.). The shot-to-shot beam intensity fluctuation is 15%, so that the percentage error in a structure factor extracted using the Monte-Carlo approach is:

$$\frac{\sigma_{MC}^{(N)}\left(|F|\right)}{\left\langle |F| \right\rangle} = \frac{1}{2\sqrt{N}} \sqrt{5.7^2 + 15\%^2 + 0\%^2} = \frac{2.85}{\sqrt{N}} \tag{3.16}$$

Therefore, for a 1% error tolerance in structure factor magnitude |F |, up to 8.12×10^4 patterns with the Bragg order (hkl) sampled are needed to achieve this accuracy.

From the above analysis, the dominant error contribution comes from the random variation in crystal size, shape and orientation represented by the first term under the root sign in Eqn. (3.16). The contribution from the shot-to-shot intensity fluctuation represented by the second term could be reduced or even eliminated by measuring the intensity of the incident beam for each shot, however this required the assumption that the beam hits the center of the crystal , not the side, and these "impact parameters" also affect scaling. Although this effect is relatively small compared to the first term, it does make the Monte-Carlo integration converge faster, and the extracted structure factors achieve a higher accuracy.

B. Two-color approaches for time-resolved Serial femto-second crystallography (TR-SFX)

The two-color approach determines changes in structure factors from two diffraction patterns that are recorded by pulse pairs from the same crystal in the same orientation.

Therefore, for each shot (i), $R^{(i)}_{(hkl)}$ is independent of the crystal size, shape, and orientation:

$$R^{(i)}_{(hkl)} = \sqrt{\frac{\left\langle I^{(i)}_{2,(hkl)} \right\rangle\Big|^{\text{intensity}}}{\left\langle I^{(i)}_{1,(hkl)} \right\rangle\Big|^{\text{intensity}}} k^{(i)}_{12}} - 1 = R_{(hkl)} \tag{3.17}$$

where $R_{(hkl)}$ denotes the true value of the change in magnitude of the structure factor (hkl), and k_{12} is given by equation 12.

We estimate $R^{(i)}_{(hkl)}$ with $R'^{(i)}_{(hkl)}$ by replacing k_{12} and the recorded intensities with their expectation values, giving,

$$R'^{(i)}_{(hkl)} = \sqrt{\frac{I^{(i)}_{1,(hkl)} \cdot \left\langle k^{(i)}_{12} \right\rangle}{I^{(i)}_{1,(hkl)}}} - 1 = \sqrt{A^{(i)}_{(hkl)}} - 1 \tag{3.18}$$

Thus, for each shot (i), the error in the estimate of the change in magnitude of structure magnitude $R'^{(i)}_{(hkl)}$ is:

$$\sigma\left(R'^{(i)}_{(hkl)}\right) = \frac{\left\langle \sqrt{A_{(hkl)}} \right\rangle}{2} \cdot \sqrt{\frac{1}{I^{(i)}_{1,(hkl)}} + \frac{1}{I^{(i)}_{2,(hkl)}} + \alpha^2}$$
$$\alpha \equiv \frac{\sigma\left(k_{12}\right)}{\left\langle k_{12} \right\rangle} \tag{3.19}$$

The percent error in $R'^{(i)}_{(hkl)}$ for one shot is inversely related to the intensity of the Bragg beam and directly related to the percentage error in k_{12}, which is denoted by α. Thus brighter Bragg beams give smaller errors and weaker ones give larger errors. Even for a particular Bragg order and constant incidence fluence, different shots correspond to

different points on the rocking curve and thus give different Bragg beam intensities. Therefore, to reduce the error in determination of the percent change in structure factor magnitude, we make use of data from all shots by assigning a weighting function that weighs brighter reflections more than weaker ones (Eqn. (3.20)). Alternatively, we may simply sum up the intensities from all shots for the same Bragg reflection (hkl), and take the ratio of the sums (Eqn. (3.21)). This is actually a self-weighted average with the weighting function being the intensity itself. These two methods can be shown to be equivalent, with a proper choice of the weighting function $W_{op}^{(i)}$ as shown in Eqn. (3.24):

$$1: \quad A_{(hkl)}^{(N)} = \sum_{i=1}^{N} W^{(i)} A_{(hkl)}^{(i)} \quad ; \quad R_{(hkl)}^{'(N)} = \sqrt{A_{(hkl)}^{(N)}} - 1 \tag{3.20}$$

$$2: \quad A_{(hkl)}^{(N)} = \frac{\sum_{i=1}^{N} I_{2,(hkl)}^{(i)}}{\sum_{i=1}^{N} I_{1,(hkl)}^{(i)}} \cdot k_{12} - 1 \quad ; \quad R_{(hkl)}^{'(N)} = \sqrt{A_{(hkl)}^{(N)}} - 1 \tag{3.21}$$

$$W_{op}^{(i)} = \frac{I_{1,(hkl)}^{(i)}}{\sum_{i=1}^{N} I_{1,(hkl)}^{(i)}} \tag{3.22}$$

It is shown that $R_{(hkl)}^{'(N)}$ is indeed a valid estimate of $R_{(hkl)}$, the true value of relative change in structure factor magnitude $\left|F_{(hkl)}\right|$, and shows that the average value of $R_{(hkl)}^{'(N)}$ approaches the true value $R_{(hkl)}$ if the number of shots N is sufficiently large (Appendix B.).

According to the theory of error analysis (Bevington & Robinson, 1992), the errors in

measured variables propagate into R′ according to:

$$\begin{aligned}\sigma(R') &= \sigma\left(\sqrt{A}\right) \\ &= \frac{1}{2}\sqrt{\langle A\rangle}\cdot\sqrt{\frac{1}{\sum_{i=1}^{N} I_2^{(i)}}+\frac{1}{\sum_{i=1}^{N} I_1^{(i)}}+\alpha^2\cdot\frac{\sum_{i=1}^{N}\left(I_2^{(i)}\right)^2}{\left(\sum_{i=1}^{N} I_2^{(i)}\right)^2}} \\ &= \frac{1}{2}\sqrt{\langle A\rangle}\cdot\sqrt{T1+T2+T3}\end{aligned} \tag{3.23}$$

We now discuss the error contributions from terms T1, T2, and T3 above. In Eqn. (3.23), T1, T2, and T3 can be approximately evaluated directly from experimental data, for an given value of the number of shots N. This requires simulations using a full data set of reflections $I_1^{(i)}$ and $I_2^{(i)}$. For a small value of N, this is necessary and can be readily undertaken. However, in case of a large value of N, it is impractical and unnecessary since the sampling can cover the whole intensity distribution of Bragg reflections ergodically, with much less fluctuation than for small values of N. We therefore estimate the error in R′ using the expectation value of the refection intensity $I_1^{(i)}$ and $I_2^{(i)}$ over the entire intensity distribution:

$$\sigma(R') = \frac{1}{2}\sqrt{\langle A\rangle}\cdot\sqrt{T1+T2+T3} \tag{3.24}$$

$$\xrightarrow{N\to\infty} \frac{1}{2}\sqrt{\langle A\rangle}\cdot\sqrt{\frac{1}{\left\langle I_2^{(i)}\right\rangle\Big|_{\text{shots}}^{\text{intensity}}}+\frac{1}{\left\langle I_1^{(i)}\right\rangle\Big|_{\text{shots}}^{\text{intensity}}}+\left(1+\beta^2\right)\alpha^2}\cdot\frac{1}{\sqrt{N}} \tag{3.25}$$

where $\left\langle I_1^{(i)}\right\rangle\Big|_{\text{shots}}^{\text{intensity}}$ and $\left\langle I_2^{(i)}\right\rangle\Big|_{\text{shots}}^{\text{intensity}}$ are the expectation values over the distribution of Bragg reflection intensities from the first and second pulses respectively. β is the relative

standard deviation in $I_2^{(i)}$ over the rocking curve, and α denotes the relative error in k_{12}. The ratio of the intensities of the two pulses k_{12} varies from shot to shot, and this fluctuation is characterized by α and determined by the stability of the emittance spoiler as well as the photon generating process (SASE or self-seeded) (Lutman et al., 2013). Using the two-color approach, this may depend on the stability of the seeding process.

As shown by Eqn. (3.25), with a sufficiently large number of diffraction patterns, the error in R′ depends on the Bragg beam intensity via T1, T2, the accuracy of the incident flux ratio α, and the statistics of nano-crystal size, shape and orientation distribution β (which may be evaluated by Monte- Carlo simulation) via T3. Among the three contributing terms, T1 and T2 are dependent on experimental conditions, such as the flux of the two pulses and their ratio, while T3 is determined by the photon generation stability, and the nano-crystal samples.

Contributions from these terms are determined by the parameters of the sample and the experimental settings, such as the statistics of nano-crystal size, shape, orientation, X-ray flux, the relative intensity of the paired pulses and the stability of the LCLS system. Without involving specific instrumental specifications and parameters, we can discuss below two different regimes of experiments: a relatively high flux of both of the paired pulses with unstable beam intensity ratio (eg two-color), and low flux for the first pulse, with perfect beam intensity control (as expected from a beam-splitting device).

In the case of high X-ray flux and unstable beam intensity, we expect small Poisson noise due to counting at the detector, but a large error in control of the relative intensity of the two pulses. Then, in Eqn. (3.25), T3 would dominate over the negligible terms T1 and T2. Assuming the same value of β = 5.7 as in the Monte-Carlo approach, the error in R′ is

$$\sigma(R') \approx 2.89\sqrt{\langle A \rangle} \cdot \alpha \cdot \frac{1}{\sqrt{N}} \tag{3.26}$$

which indicates that the error in the determination of the relative change of structure factor magnitudes is proportional to the relative error in the intensity ratio of the two paired pulses, and hence depends on the stability of the emittance spoiler and the photon generation process. This error decreases as the square root of the number of patterns recorded, which is similar to the Monte-Carlo approach (Eqn. (3.15)) but with a prefactor $\sqrt{\langle A \rangle} \cdot \alpha$. Comparing Split-and-Delay and Monte-Carlo approaches, we can easily establish a criterion for superiority of the former over the latter:

$$\alpha \cdot \sqrt{\langle A \rangle} < 1 \tag{3.27}$$

For 20% change in structure factor magnitude as an example, the critical value of α is 0.83. In other words, any two-color system with an error of less than 83% in intensity ratio makes the two-color approach preferable.

In the case of a weak first pulse (which does not destroy the sample) but with perfect beam intensity control, the Poisson noise T1 and T2 become the dominant error

contribution rather than the negligible relative intensity fluctuation T3. Then the error in R′ is

$$\begin{aligned}\sigma(R') &\approx \frac{1}{2}\sqrt{\langle A\rangle}\cdot\sqrt{\frac{1}{\sum_{i=1}^{N} I_2^{(i)}}+\frac{1}{\sum_{i=1}^{N} I_1^{(i)}}} \\ &\approx \left(\frac{\sqrt{2}}{2}\sqrt{\langle A\rangle}\cdot\sqrt{\frac{1}{\langle I\rangle}}\right)\frac{1}{\sqrt{N}}\end{aligned} \tag{3.28}$$

Thus, the error is now independent of the specific statistics of the nano-crystal samples, and is only determined by the summed reflection intensities from all patterns. Additionally, a smaller error is expected for a brighter Bragg reflection than a weaker one. For TbCatB crystals of 0.9×0.9×11μm average size, assuming structure factors F~10^4, an X-ray beam with photon energy of 9.4keV and beam diameter of 4um, at the Henderson "safe-dose" limit (Henderson, 1995) of 1MGy at room temperature (allowing study of dynamics), the average number of photons of a reflection in a pattern is estimated to be 77. Hence, the error in R′ is

$$\sigma(R') \approx 0.087\frac{1}{\sqrt{N}} \tag{3.29}$$

For two-color experiments, the intensity or energy of each pulse can be measured by using a in-line spectrometer (Zhu et al., 2012). In this case, the uncertainty in k_{12}, denoted by α , becomes dependent on the accuracy of the intensity measurements. The error in R′ is then equal to that given by Eqn. (3.28).

C. Fixed-sample experiments with goniometer

With sample fixed to a holder and a goniometer, the crystal orientation can be controlled accurately to facilitate scans across the rocking curve. In contrast to the stills obtained from different crystals in random orientations, this scan process may generate a sampling over the angular profile of the Bragg reflections with equally spaced increments and the relative error due to Poisson noise in intensity measurement is

$$\frac{\sigma_R\left(|F_{es}|\right)}{\left\langle |F_{es}| \right\rangle} = \frac{1}{2}\sqrt{\left(\frac{\sigma(\Delta\Psi)}{\Psi_T}\right)^2 \left(1+\beta^2\right) N_s + \frac{1}{\langle I\rangle\Big|_{\text{intensity}}^{\text{shots}} N_s}}$$
$$= \frac{1}{2}\sqrt{E1+E2}$$

(3.30)

where Ψ is the angular variable, as the abscissa of the rocking curve. Ψ_T is the total angular width of the rocking curve and $\Delta\Psi$ is the sampling increment. Ns is the number of sampling points, $\langle I\rangle\Big|_{\text{intensity}}^{\text{shots}}$ denotes the mean intensity of each sample point averaged over both Poisson noise and the entire rocking curve. β is the relative standard deviation in measured intensity over the rocking curve, consistent with previous discussion of the Monte-Carlo and two-color approaches. Beside the error contributions from goniometer control and intensity measurement, another contribution comes from the systematic error resulting from integration by quadrature. For one-point quadrature, the error is proportional to square of the sampling increment $\Delta\Psi$ and the first derivative of the curve f' (Press, Flannery, Teukolsky, & Vetterling, 1988):

$$\sigma_S\left(\left|F_{es}\right|^2\right) = O\left(f' \cdot \Delta\Psi^2\right) \propto \frac{1}{N_s^2} \tag{3.31}$$

In the destructive-readout mode, where the X-ray beam must be translated to a fresh point on the sample sufficiently far away from the hole drilled by the previous shot to avoid damage, fixed-sample experiments sampling rocking curves with even increments and maximum beam intensity would give a random error which goes as $1/\sqrt{N_s}$ as indicated by Eqn. (3.30). (We assume perfect goniometer control). In this regard, fixed-sample experiments and M.C. experiments are essentially equivalent from the point of view of error reduction and data efficiency. However, the prefactor in the M.C. approach is much larger than in the fixed-sample approach since the former uses a random sampling, whereas crystal orientation and sampling is totally controllable using a goniometer. For CXI beam line at LCLS, with a typical pulse energy of 2 mJ, the estimated average photon counts for the same condition is approximately 100 times that of the non-destructive mode resulting in the prefactor of 0.0057. We must also note however, the number of shots we can take on a single large crystal Ns is limited by the crystal size as well as the safe distance between shots to avoid radiation damage caused by previous shots. Therefore, an upper limit might exist for the accuracy in structure factor measurement using this diffract-and-destroy mode in fixed sample experiments.

If the beam intensity is adjusted below the Henderson safe dose threshold so that the sample is not destroyed the error fro a fixed sample is then:

$$\frac{\sigma_{R,\min}\left(\left|F_{es}\right|\right)}{\left\langle\left|F_{es}\right|\right\rangle} = \frac{1}{2}\sqrt{E1+E2}$$
$$\approx \frac{1}{2}\sqrt{E2} = \frac{1}{2}\sqrt{\frac{1}{\left\langle I\right\rangle\Big|_{\text{intensity}}^{\text{shots}} N_s}} \tag{3.32}$$
$$\propto \frac{1}{2}\left|F\right|^{-1}\sqrt{\frac{1}{D_H \rho L A}}$$

where D_H is the Henderson safe dose, ρ is the mass density, L is the attenuation length of the sample, $|F|$ is the magnitude of the structure factor and A is the effective beam area. Eqn. (3.32) indicates that the random Poisson error in detector counts is independent of the number of sampling points on the rocking curve, and is only dependent on the sample and X-ray beam parameters. This is reasonable, since the total photon signal is limited by the Henderson safe dose no matter how many sampling points are used in a scan. Therefore, combining systematic and random errors for consideration, an optimal value of Ns exists for minimal error (Eqn. (3.31) and (3.32)).

To determine the experimental design, detailed simulations need to be carried out to estimate the errors in the different approaches for specific samples. For TbCatB crystals (Redecke et al., 2013) of 0.9×0.9×11μm average size , assuming a structure factor F~104, a photon energy of 9.4 keV and beam diameter of 4 μm, the Henderson dose limit () of 1MGy at room temperature, we show the number of patterns needed to achieve 1% accuracy in structure factor measurement for Monte-Carlo, two-color and goniometer-based XFEL experiments in Fig. 3.1. The error follows the inverse square root rule ($1/\sqrt{N_s}$) in the Monte-Carlo, two-color or split-and-delay approaches. However,

the error falls more rapidly with number of diffraction patterns for the two-color or split-and-delay method than for the Monte-Carlo approach. To identify a 1% change in a structure factor in pump-probe experiments, less than 100 pairs of patterns with the corresponding Bragg order indexed are needed for the two-color or split-and-delay approach, whereas 80000 patterns are required in the conventional Monte-Carlo approach. This improvement in error reduction and data efficiency is a direct result of the elimination of the stochastic factors, such as random orientation and varying size and shape of the crystals. Two-color or split-and-delay experiments have the advantage of sensitivity to change in structure factors over the other approaches, rather than any superior accuracy of direct structure-factor measurement. At the safe dose that minimizes damage, fixed-sample experiments give an error independent of sampling procedure but limited by the X-ray dose the sample can tolerate. Complete data sets must be obtained to solve the time-resolved structure. The number of patterns required for this purpose is definitely much more than the number of patterns needed to achieve a certain accuracy in a single structure factor since we need sufficient patterns that cover the whole reciprocal space to produce the electron density maps. We assume that the number of patterns needed to form a complete data in two-color approach is about the same as that needed in liquid jet sample delivery, based on the Monte-Carlo approach, since the statistics of the crystal orientation distribution is the same for both methods. Also, in case that the crystal is much larger than the typical beam size of 4um, we can expand the beam to match the

size of the crystal by defocussing, to maximize the total signal hence to reduce the error in structure factor measurement. An increase in the beam size by the factor of 25 (100um) reduces the error in fixed sample experiments to approximately 1%, which is comparable to the other approaches. But certainly, larger crystals not only favor the fixed sample experiments, but are also preferred in all modes, since they yield stronger diffraction signals and so higher resolution data unless this is limited by crystal quality.

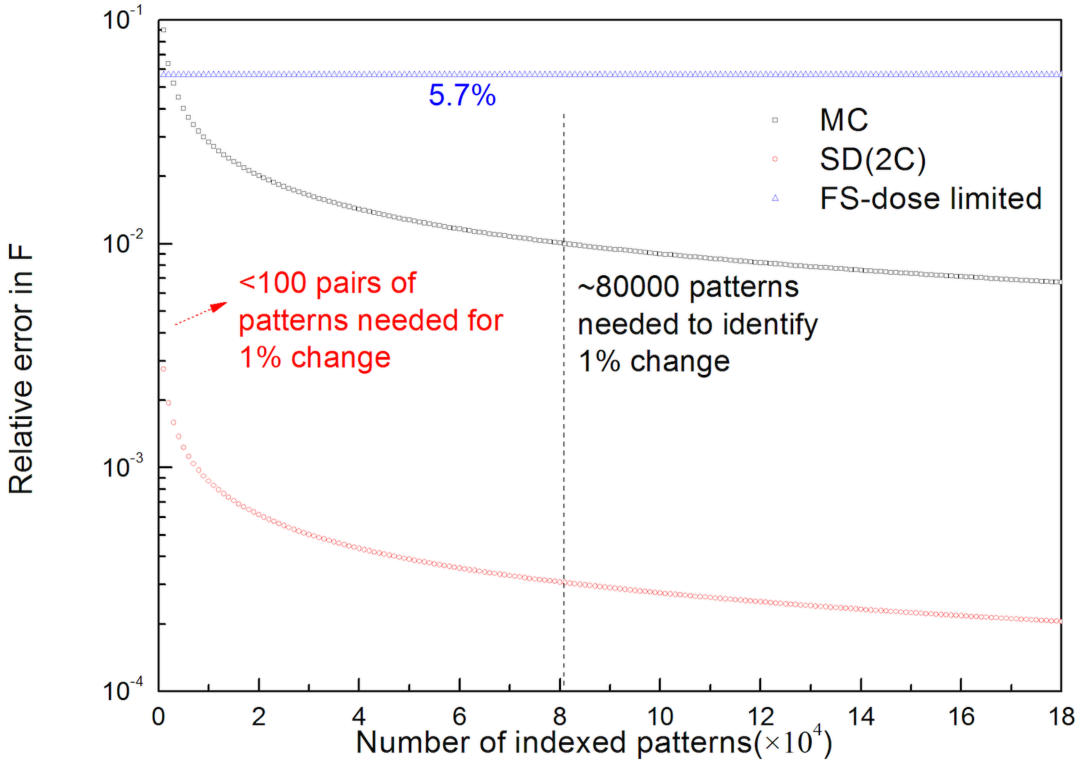

Fig. 3.1. Relative error in structure factor magnitude measured in Monte-Carlo (MC), split-and-delay or two-color (SD, 2C) and non-destructive mode of goniometer-based fixed sample (FS) approaches for time-resolved serial femtosecond X-ray diffraction

(TR-SFX). To identify 1% change in structure factor in pump-probe experiments, less than 100 pairs of patterns are needed in two-color or split-and-delay mode, compared to approximately 80000 patterns required in the Monte-Carlo approach. non-destructive mode of goniometer-based fixed sample approach gives an error limited by the X-ray dose, but independent of sampling. Diffract-and-destroy mode of fixed sample approach yield an error with a prefactor of 0.57%, but the number of patterns collected from one single crystal is limited by the crystal size and the distance between consecutive shots in order to avoid radiation damage. Diffraction from micro-crystals trapped on a calibrated lattice follows the essentially the same error reduction behavior as Monte-Carlo approach using the liquid jet delivery system.

Discussion and conclusion

The Monte-Carlo approach has been widely adopted for serial femto-second crystallography (SFX) in recent years. Using tens of thousands of patterns, merged partial intensities converge accurately to yield the structure factors, allowing structures to be solved at better than 0.2nm resolution, which might not otherwise have been solved due to small crystal size or radiation sensitivity [24]. The low data efficiency mainly results from uncontrollable stochastic variables contributing to the error in structure factors. These contributions add in quadrature, and the large intensity variation of the same Bragg reflection on different shots (covering several orders of magnitude) due to partiality (ie

different deviations from the exact Bragg condition) dominates the error in the Monte-Carlo approach.

To improve on the traditional Monte-Carlo integration and merging procedure, new methods of treating the partial intensities, intensity integration, scaling and post-refinement have been proposed and studied. By modeling the angular profile of the Bragg spots from mosaic crystals (Hattne et al., 2014), an integration mask can be customized for each reflection. Using on a geometrical model for partiality, the diffraction conditions for each pattern can be refined to estimate the partiality, so that full reflection intensities can be predicted, and this refinement procedure repeated iteratively to obtain the best estimate. (White, 2014) Common reflections on different shots also assist scaling, using post-refinement and the Ewald offset correction, which assumes a Gaussian rocking curve for a sufficiently large crystal. (Kabsch, 2014). Our two-color method complements these algorithmic approaches for improved accuracy, going beyond the Monte-Carlo method, for time-resolved diffraction.

The two-color approach eliminates variations in crystal size, shape and orientation that dominate the Monte-Carlo approach, by probing the same crystal twice in the same orientation with two pulses of different energies, separated in time. The ratio of partial intensities of Bragg spots with identical Miller indices from two pulses is recorded for each pattern, and then summed with a weighting to obtain the percentage change in structure factor. The accuracy in structure factor change is determined by the total signal

summed over all patterns. Therefore, in spite of the low dose limit for the first pulse (which must not destroy the crystal) the accuracy improves with the number of patterns collected. For the TbCatB crystals used recently (Redecke et al., 2013), at the Henderson safe dose limit of 1Mgy at room temperature, less than 100 patterns are needed to achieve 1% accuracy, compared to 80000 patterns for the Monte-Carlo approach (Fig. 3.1). From the point of view of error reduction and data efficiency, the two-color approach appears to be a better choice for pump-probe time-resolved experiments, provided a sufficiently long delay between X-ray pulses can be obtained for the process of interest.

A difference Fourier charge-density map is normally applied to study structural changes. The difference map is shows changes in the electron density much more sensitively than a normal Fourier Map (Henderson & Moffat, 1971). With unknown phases, the peak height in a map is half that with phase information if the conditions $\Delta|F|/|F| \ll 1$ and $\sigma(\Delta|F|)/\Delta|F| \ll 1$ are satisfied. For most pump-probe experiments, these conditions are satisfied, making Difference Fourier Map applicable to two-color data.

However our two-color approach and error analysis are based on several essential assumptions, which must be considered here. First, the time interval between the two pulses must be much shorter than the rotational diffusion time of the crystal in solution (typically milliseconds for a one-micron crystallite in buffer) so that it can be treated as stationary. Second, the difference in wavelength between the two pulses must be sufficient to separate the two diffraction patterns in the same readout, but not too large so

that the corresponding Ewald spheres are far from each other intersecting different Bragg reflections. Third, the crystal size must neither be too small so that the broad shape transform will not allow us to separate the two patterns, or too big to invalidate our shape transform analysis. (Our error analysis assumes that the two patterns are taken from almost the same point on the rocking curve). To investigate these assumptions for future two-color experiments, diffraction patterns from I3C ("magic triangle") (Beck & Sheldrick, 2008) micron-sized inorganic crystals were simulated for X-ray pulses at energies of 6.6keV and 6.685keV , as shown in Fig. 3.2. Using the CSPAD detector at LCLS with the minimum working distance of 5mm, the 85eV (1.3%) energy difference shifts the Bragg spots by approximately 20 pixels at the 2Å resolution ring, which corresponds to the side edge of the detector. Since the relative displacement between the Bragg spots of the same Miller index increases with resolution, the Bragg reflections at low resolution can be separated by using a larger working distance or an additional back detector, illuminated by a central hole in the front detector. Over the past year there have been dramatic advances in the ability to model partiality for SFX data from several groups, using iterative optimization algorithms and a suitable model for mosaicity (Helen M. Ginn et al., 2015; Hattne et al., 2014; Kabsch, 2014; White, 2014). If we use these methods to model the partiality for each wavelength separately on the same detector readout, the resulting more realistic results will fall somewhere between the Monte-Carlo error curve and two-color error curve (Figure. 1), since curve "2C" assumes no difference

in partialities of the two wavelengths.

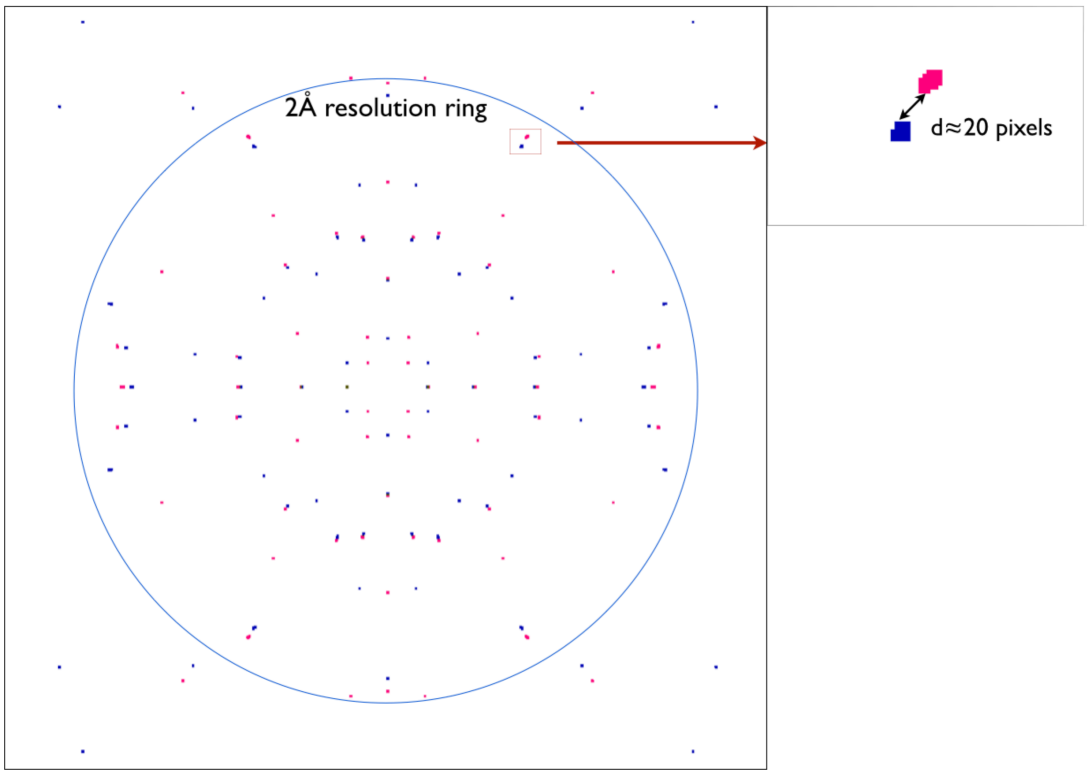

Fig. 3.2. Simulated diffraction pattern ((100) plane) from I3C ("magic triangle") crystals (orthorhombic. Pbca, a=9.214Å, b=15.735Å, c=18.816Å)[27] using X-ray pulses at energies of 6.6keV and 6.685keV in two-color approach. Crystal size is 0.005µm×1.3µm×1.5µm and identical intensity for all Bragg reflections is assumed just to show the Bragg spot positions. Red and blue colors indicate Bragg spots from 6.6keV and 6.685keV respectively. Bragg spots of same index from two colors are clearly separated by detectable displacements. The displacement is approximately 20 pixels at 2Å resolution ring on CSPAD detector at LCLS with the minimum working distance of 5mm.

Goniometer-based fixed-sample experiments provide accurate control of the crystal orientation which our SFX experiments are not capable of. In destructive mode, each X-ray shot drills a hole in the crystal, which must be translated to a fresh point for the next shot. Beam intensity is maximized to obtain the highest SNR and the error decreases

as the inverse square root of the number of patterns, which is similar to the Monte-Carlo approach, except that the prefactor is much smaller due to the accurate control of crystal orientation. With the beam attenuated or defocussed to a level below the damage threshold, goniometer-based experiments allow us to probe the same region of a sample in different orientations from which local information on structures or dynamics can be extracted. The low dose limit gives poorer statistics, and the error in the measured structure factor is found to be independent of the number of sampling points (or patterns from the same region), and is only determined by the total dose deposited into the probed region of the crystal.

CHAPTER 4

IMPROVING AUTO-INDEXING IN SERIAL CRYSTALLOGRAPHY

Introduction

Superior brilliance and ultra-short pulse duration of X-ray Free Electron Lasers (XFEL) enable the studies of bio-molecular structures and conformational dynamics using the diffract-before-destroy method. Snapshot diffraction patterns from different crystals of various shape, size and orientation are recorded in a typical experiment. This differs from the synchrotron diffraction methods, and is termed Serial Femto-second Crystallography (SFX). In synchrotron crystallography, the molecule structure can be typically solved from a few big crystals using the oscillation approach where the crystals are rotated in the process of diffraction recording. In SFX, each of the patterns recorded is a still diffractive image of an individual crystal with certain distribution in shape, size and at a random orientation, these patterns should be merged together to reconstruct the 3-D reciprocal space of the crystal. Finally, Fourier transform is taken to obtain the electron density map of the objective molecule from the reconstructed reciprocal space. This difference compared to synchrotron crystallography becomes the source that complicates the data processing and eventually necessitates the development of data analysis modules specifically for SFX. Each snapshot pattern corresponds to one slice of the reciprocal space by the Ewald sphere that represents the diffraction geometry. Therefore, partial

reflection intensities are recorded in diffraction patterns in contrast to the case of crystallography using synchrotron light source where full reflection intensities can be recorded from rotation series. Monte-Carlo integration approach (Kirian et al., 2010) was first used to merge all patterns to obtain the structure factor list in SFX. It has been proved successful in averaging out the stochastic factors including the partiality and widely accepted as the main method for SFX data analysis. However, millions of patterns are needed to converge to a reliable structure solution using Monte-Carlo integration due to its stochastic nature. Many recent works are published reporting enhanced data quality and efficiency by applying post-refinements and partiality analysis before merging the data (Helen Mary Ginn et al., 2015; White, 2014). Since partiality varies rapidly with orientation change, accurate orientation determination is essential to effective partiality analysis. In addition, data efficiency can be largely increased by improving the indexing rate, especially for those patterns with low resolution and few Bragg spots that can be recognized. This chapter discusses a new algorithm for sparse pattern indexing and also explores new methods to improve the accuracy in orientation determination for individual diffraction patterns using not only the geometrical information but also reflection intensities. Potential synergy may also be expected between this accurate orientation determination and more sophisticated partiality modeling to achieve faster and more accurate structure determination in SFX.

Conventional SFX data analysis pipeline

In SFX data analysis, snapshot diffraction data are generally processed using the software Cheetah and CrystFEL (White et al., 2012). CrystFEL SFX data analysis pipeline (Fig. 4.1) basically starts with hit and peak finding, followed by indexing implemented by calling auto-indexer subroutines such as MOSFLM, and DIRAX, etc., then peak intensity integration, and at last intensity merging which gives a merged reflection list. The auto-indexing and peak intensity integration are conducted in combination using the script "indexamajig" of CrystFEL. For each pattern identified as a hit, this module passes the peak position information as input arguments to external auto-indexers such as MOSFLM (Powell, 1999), DIRAX, and etc. in the library and receives the orientation matrix (including the lattice constants information) as the return. These auto-indexing modules generally work in the following way (Campbell, 1998; Leslie, 2006; Powell, 1999; Steller, Bolotovsky, & Rossmann, 1997). They take the Bragg peak positions as input information and convert them to 3-D lattice vectors in reciprocal space (Fig. 4.2(a)). Then, these reciprocal vectors are projected in a set of discrete directions in a hemisphere followed by Fourier transform of the projected lengths of all vectors (Fig. 4.2(b)). Sharp spikes in the histogram of the Fourier transform indicate that the projection direction lies in the principal axis and the frequency gives the lattice vectors along the principal axis. Then, "indexamajig" module predicts possible Bragg peak positions based on the orientation matrix for each pattern and integrate the intensities over pixels for each peak if the predicted peak position is considered an

acceptable match to the experimental peak position on the detector.

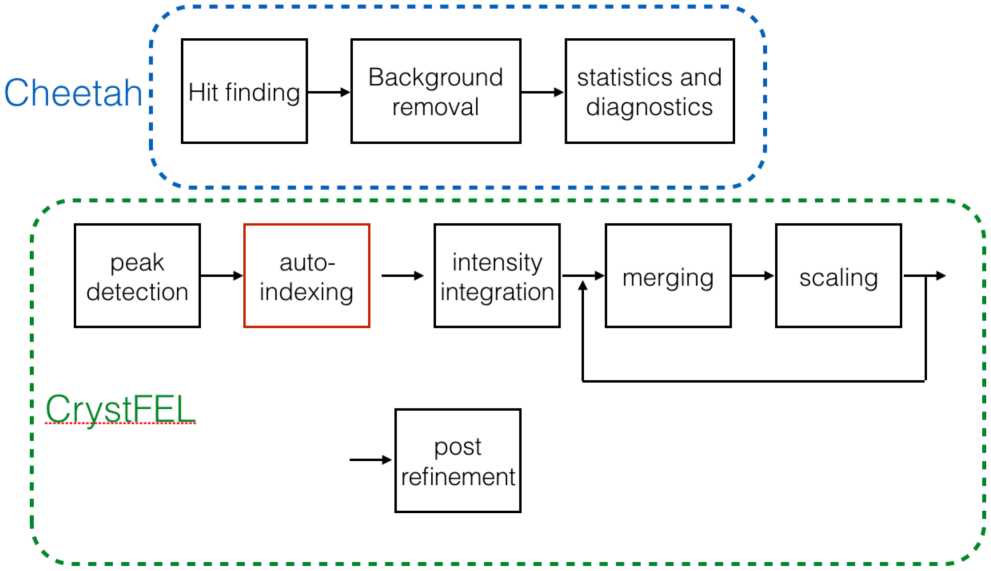

Fig. 4.1. SFX data analysis pipeline using Cheetah and CrystFEL.

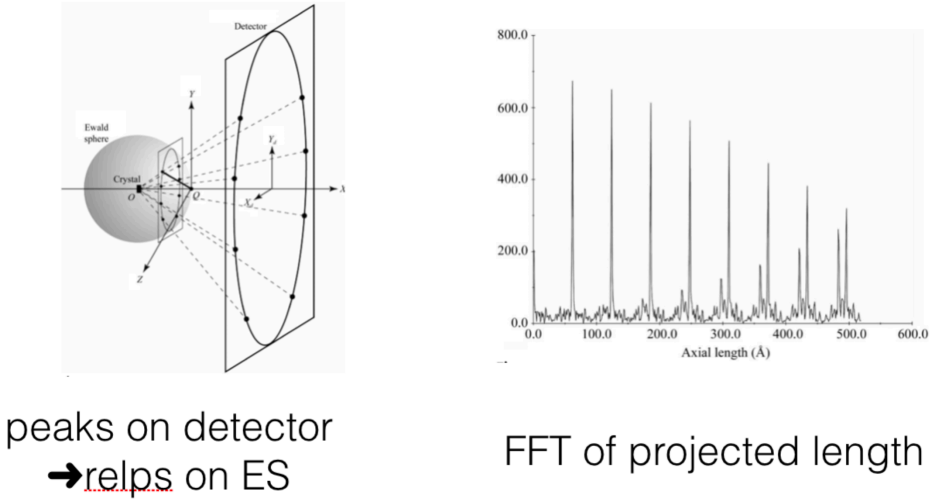

(a) (b)

Fig. 4.2. (a) Diagram of mapping Bragg peaks on detector to 3-D reciprocal space. (b) Histogram of Fourier transform of projected length for all reciprocal vectors. Spikes

indicate a correct principal axis direction, and period gives the lattice vector length along this direction. (Rossmann, Leslie, Abdel-Meguid, & Tsukihara, 1979)

This data analysis pipeline proves widely successful for most of the previous SFX works. However, the Fourier transform algorithm based auto-indexers typically require that each pattern consist of no less than 20 (or even more (Campbell, 1998)) well-identified peaks to yield a reliable orientation matrix. Therefore, these widely used auto-indexers become much less effective for data sets that are comprised of a large portion of sparse patterns. Auto-indexing algorithm for sparse patterns fits in the case to increase the data utilization and dig more out of the sparse pattern data sets.

A new algorithm for sparse pattern indexing

Given only minimal number of peaks can be identified from each pattern, the Fourier transform and projection based auto-indexers cannot be applied effectively to sparse pattern data sets. A new algorithm is devised to index sparse patterns assuming some prior knowledge of lattice constants. This algorithm works in the following way (Fig. 4.3): a) Bragg peaks are identified according to a set criterion for each pattern, and the 2-dimensional peak positions on the detector panel are recorded; b) These peak positions along with its intensity, signal to noise ratio and other properties are written into a plain text file for each pattern; c) The 2-dimensional peak positions on detector panel are converted to 3-dimensional vectors in reciprocal space in the way shown in Fig. 4.2(a); d)

5 best peaks are chosen from the peak list according to intensity, signal to noise ratio or other figure of merits; e) vector lengths and angle between them are calculated for each these 10 possible pairs of peaks; f) the length, ratio and angle between all possible pairs of reciprocal vectors within a certain resolution limit are tabulated based on the prior knowledge of the lattice; g) the calculated vector lengths, ratio and angles of the 10 pairs are compared against the table and all entries that are considered as matches are selected and recorded in the solution pool. The orientation matrix and HKL Miller indices are calculated for each solution; h) One common solution is selected from the solution pool as the intersection set between solution sets for 10 vector pairs. The orientation matrix is calculated and recorded; i) using the obtained orientation matrix, a diffraction pattern is simulated and possible peaks are predicted; j) If the predicted peaks are considered an acceptable match to the experimental pattern, the auto-index solution is accepted, otherwise rejected.

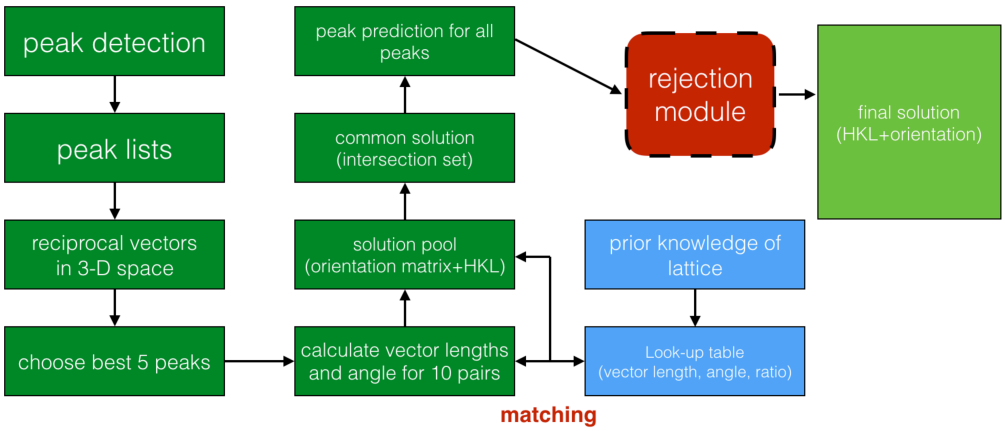

Fig. 4.3. Flowchart of the new algorithm for sparse pattern indexing. 5 best peaks are selected from the pattern and used for indexing. Prior knowledge of lattice is required.

Improve orientation accuracy using Bragg intensity

One important fact in X-ray diffraction physics is that Bragg spots remain essentially at the same positions while the reflection intensities vary sensitively if the crystal is rocked slightly about an axis perpendicular to X-ray beam direction. X-ray diffraction patterns are simulated for a Body center cubic (BCC) lattice with a lattice constant 106 Å at two slightly different orientations (30,45,10) and (30,45,10.1) in Euler angle representation (Fig. 4.4). It is seen that a small rocking angle of 0.1° does not introduce any noticeable changes in Bragg peak positions, but intensities increase and decrease significantly in red and green circles respectively (Fig. 4.4).

Conventional SFX data analysis pipeline only makes use of the peak positions (geometrical information) in the auto-indexing stage. Therefore, it is expected that the accuracy in orientation determination cannot reach the level that is able to distinguish patterns with same Bragg spot positions but different intensities (e.g. Fig. 4.4). For experiments where the intensity measurement is crucial and decisive such as the single wavelength anomalous diffraction (SAD) phasing, high accuracy in orientation determination and hence intensity measurement combined with partiality correction is required to provide convincing results.

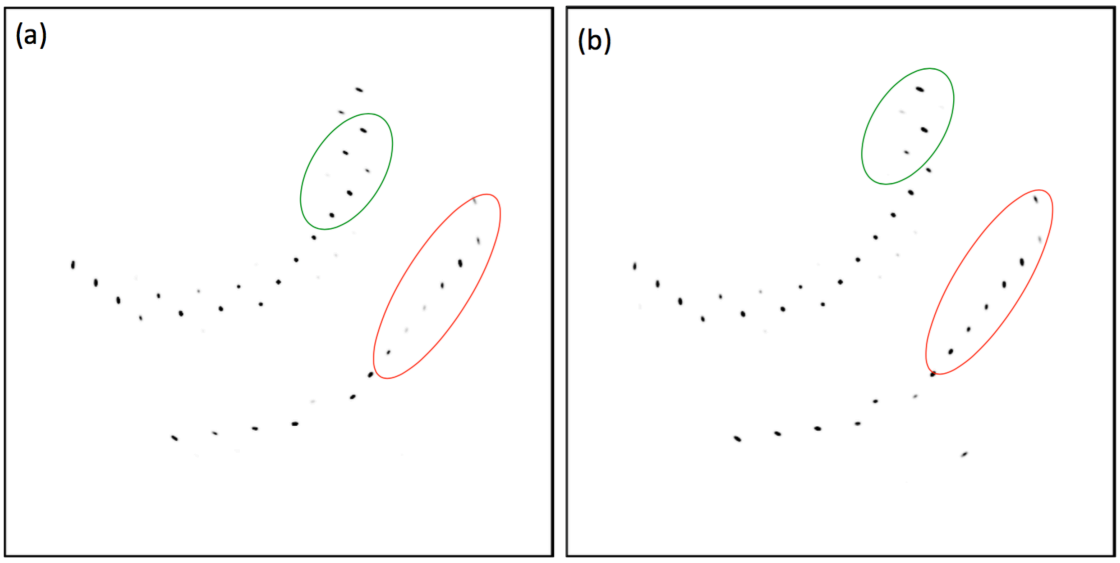

Fig. 4.4. Simulated diffraction patterns from BCC lattice (a=106 Å) at orientations of (a) [30,45,10] and (b) [30,45,10.1] in Euler angle representation. The small rocking does not change the Bragg spot positions essentially while the reflection intensities vary significantly. (Bragg intensity increases and decreases in red and green circles, respectively.)

An approach that makes use of both positions and intensities of Bragg peaks is explored to determine the orientation with a greater accuracy than that provided by current auto-indexers. In this approach, the crystal orientation is represented by a unique set of three Euler angles (Fig. 4.5). To represent a crystal orientation, a reference orientation is selected in such a way that c-axis of the lattice coincides with z-axis of the lab frame, and the a-axis coincides with x-axis. As a theorem of space geometry, an

arbitrary orientation can be achieved from the reference orientation by a unique rotation operation about a certain axis. In Euler angle representation, three Euler angles (φ,θ,α) are defined to index this rotation operation, hence the orientation. φ is defined as the angle between the z-projection of the rotation axis and the x-axis. θ is the angle between the rotation axis and z-axis. α is the rotation angle about the axis. A problem for Euler angle representation is the potential singularities and significant numerical errors when the rotation axis is close to the axes of the coordinate frame. Alternative representations of crystal orientation can be used here, such as quaternion and Cayley-Klein representations to overcome the problems mentioned. Despite the numerical difficulties that Euler angle representation can potentially cause, one big advantage of this representation is that the three Euler angles can be intuitively interpreted and related to the rotation operation.

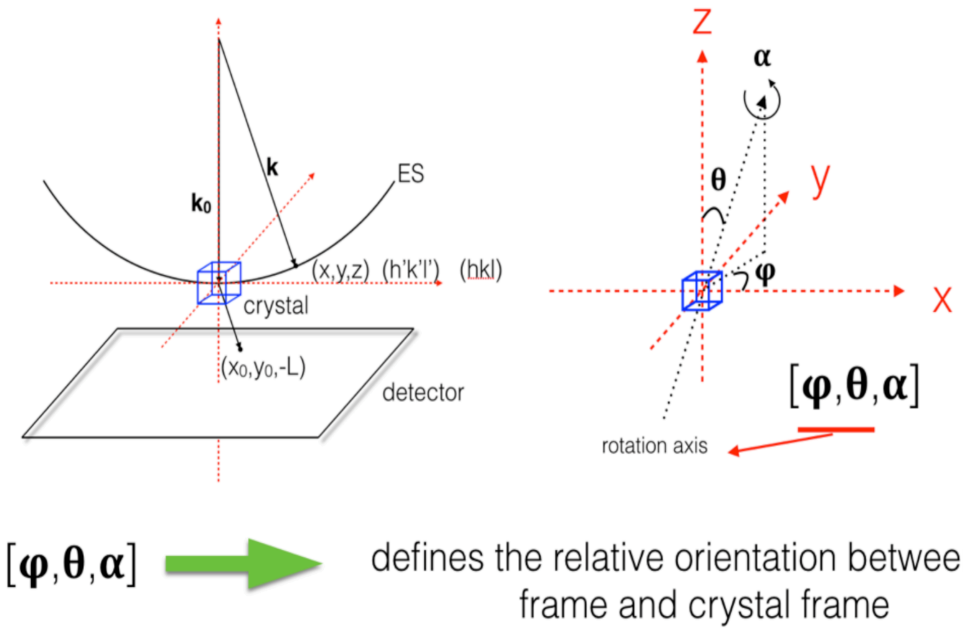

Fig. 4.5. Euler angle representation of crystal orientation. Red dashed axes (xyz) represent the lab frame that is fixed to the incidence beam direction and detector. A reference orientation is selected in such a way that c-axis of lattice coincides with z-axis of the lab frame, and a-axis coincides with x-axis. As a theorem of space geometry, an arbitrary orientation can be achieved by a unique rotation operation about a certain axis (black dashed arrow) from the reference orientation. Euler angle φ is the angle between the z-projection of the rotation axis and the x-axis. Euler angle θ is the angle between the rotation axis and the z-axis. Euler angle α is the rotation angle about the rotation axis to achieve the crystal orientation.

In this new approach to determine the orientation, the intensity correlation between an experimental pattern and a predicted pattern from a specific model is calculated. Since

the reflection intensities vary by orders of magnitude between different Bragg orders, and are sensitive to crystal orientation, maximization of the intensity correlation does not necessarily gives the correct orientation. Considering this fact, correlation coefficients of a rocking series about a rotation axis (φ,θ) are calculated instead of that of separate individual orientations (Fig. 4.6 left). The symmetry of the correlation coefficient as a function of the rocking angle (termed as "virtual rocking curve") (Fig. 4.6 right) around a certain orientation is chosen as a second indicator of the correct crystal orientation.

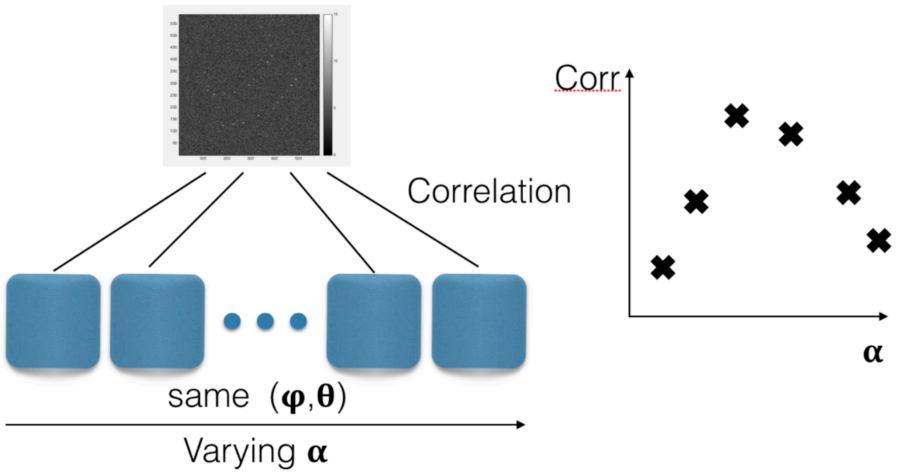

Fig. 4.6. Intensity correlation between calculated pattern and experimental pattern plotted as function of rotation angle (α). ("Virtual rocking" curve)

The intensity correlation does not vary smoothly and continuously through the Euler angle searching space, due to the discrete distribution of Bragg intensity in reciprocal space. Because of this nature, genetic algorithm is chosen as the search engine over other

conventional optimization algorithms such as Newton's method and gradient method. Genetic algorithm is implemented in the orientation searching in the following way (Fig. 4.7). A set of guessed orientations are input to the program as the initial trials. A proper fitness function is chosen that basically combines the intensity correlation and the symmetry metric of the "virtual rocking curve". Fitness is evaluated for each solution in the solution pool and those with the highest scores are kept. Euler angles of these remained solutions are permutated and mutated by a controlled probability and range to produce new solutions of next generation. Iterations of this procedure are carried out till the best solution meets a designated standard or a maximum number of iterations is reached. This implementation of the genetic algorithm in the case of orientation searching exactly mimics the genetic evolution process in nature. The three Euler angles are treated as the "genes" and are freely assorted and mutated in a controllable way. Sorting according to the fitness score is an analogy to the natural selection, which keeps the best solutions in the gene pool.

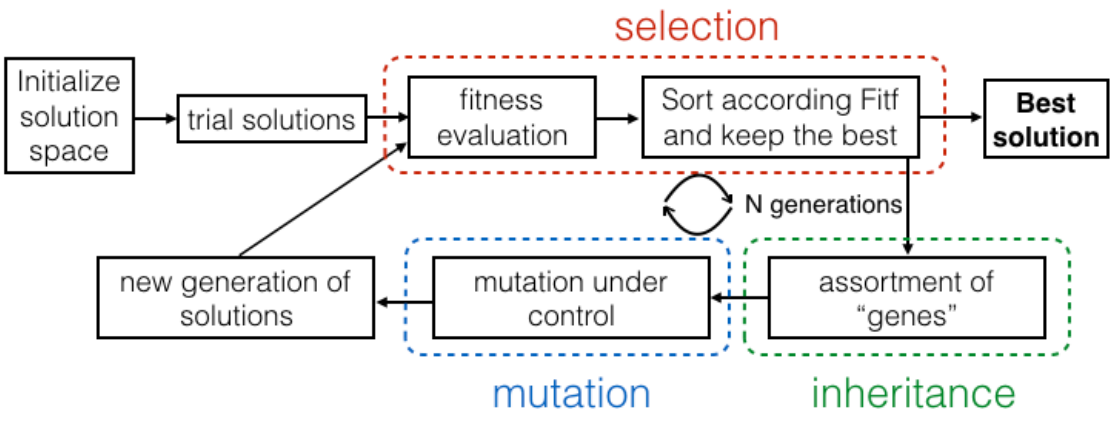

Fig. 4.7. Flowchart of orientation determination based on intensity correlation implemented by genetic algorithm. The genetic algorithm mimics the process of natural evolution that is generally comprised of natural selection, independent assortment of genes and mutation.

Indexing simulated sparse patterns

Sparse pattern auto-indexer module has been developed according to the algorithm mentioned in previous section (Fig. 4.3) in MATLAB environment. 400 Diffraction patterns from I3C ("magic triangle") crystals were simulated for 9.61keV photon energy, 0.5um beam radius, 110um pixels, 53.18 degrees maximum scattering angle and 0.07m working distance at random orientations. Because of its relatively small unit cell and Poisson noise, only 3 to 5 peaks can be identified in each pattern (Fig. 4.8 (a)). These sparse patterns were first used as a first test for the auto-indexer module. The sparse pattern auto-indexer module gave correct crystal orientation as well as Miller indices for all 400 patterns at the cost of millisecond level computation time. In addition to the fast computation time, the orientation was constructed with a great accuracy. Taking an example from the 400 patterns that were indexed successfully (Fig. 4.8), the orientation was reconstructed as (-10.5713,46.8855,139.2) compared to the correct orientation (-10.4676, 46.9022, 139.1443) in Euler angle representation, with an accuracy of less than 0.1 degree.

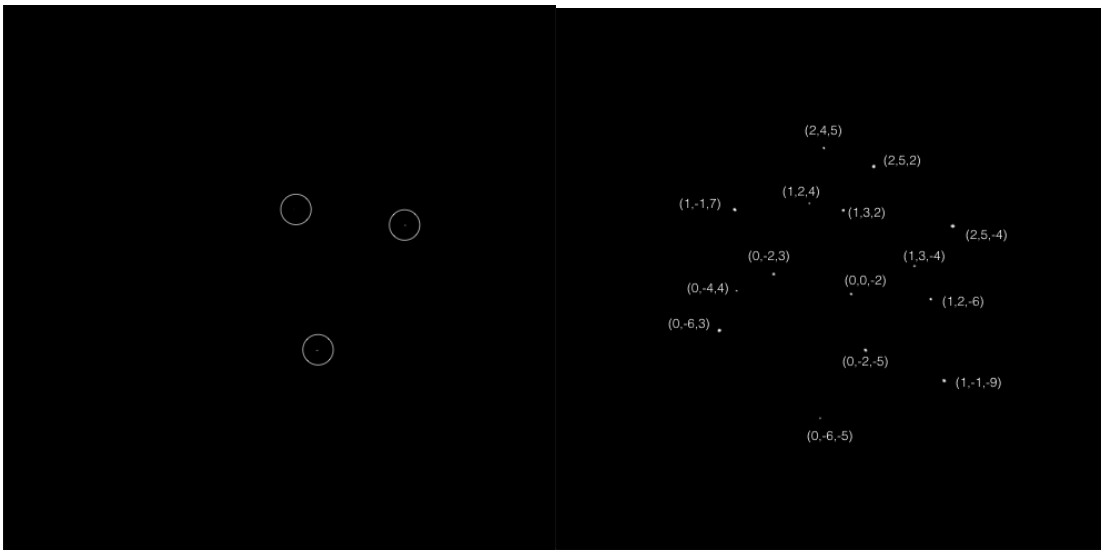

(a) (b)

Fig. 4.8. Simulated I3C patterns indexed by sparse pattern auto-indexer. (a) Sparse diffraction pattern simulated for I3C nanocrystal at the orientation (-10.4676, 46.9022, 139.1443), with 3 Bragg peaks identified. (b) Pattern (a) indexed using the sparse pattern auto-indexer. Reconstructed crystal orientation is (-10.5713 46.8855 139.2). More peaks are predicted for the reconstructed orientation and HKL Miller indices are given.

Indexing experimental patterns in protein crystallography

To extend the algorithm prototype to real experimental application in protein crystallography, the sparse pattern auto-indexer was tested again with data from 5-HT2B receptor protein crystals (Liu et al., 2013). 8 sparse patterns that are barely indexed by CrystFEL were selected from run 34 of the data set and passed to sparse pattern auto-indexer. 4 patterns out of the 8 were successfully indexed and the computation time

varies noticeably from one pattern to another. This pattern-to-pattern variation in auto-indexing success rate and computation time is attributed to the inhomogeneity of the crystal lattice, and presumed value of lattice constants as the input information of the auto-indexer. The computation time is generally much longer than that in the case of I3C crystals. This is mainly because Bragg spots are much denser in reciprocal space and more orders are included within the same resolution limit in protein crystallography. Therefore, more Bragg orders need to be searched and compared against longer look-up tables. To check the consistency of indexing between the conventional auto-indexer and the sparse pattern indexer, orientation matrices are compared from CrystFEL and the new auto-indexer taking pattern "r0034_211432_bd9.h5" as an example (Fig. 4.9). CrystFEL indexing module gives orientation matrix: a_star= +0.0003906 -0.1001362 -0.1275745 nm^{-1}; b_star= -0.0032483 -0.0643020 +0.0497996 nm^{-1}; c_star= -0.0593760 +0.0017830 -0.0018698 nm^{-1}, and the new auto-indexer gives a_star= -0.0035637 -0.0993551 -0.1280000 nm^{-1}; b_star= -0.0064575 -0.0640386 +0.0498872 nm^{-1}; c_star= -0.0592866 +0.0045269 -0.0018632 nm^{-1}. These two orientation matrices are considered consistent with each other since errors caused by deviation in lattice constants are expected.

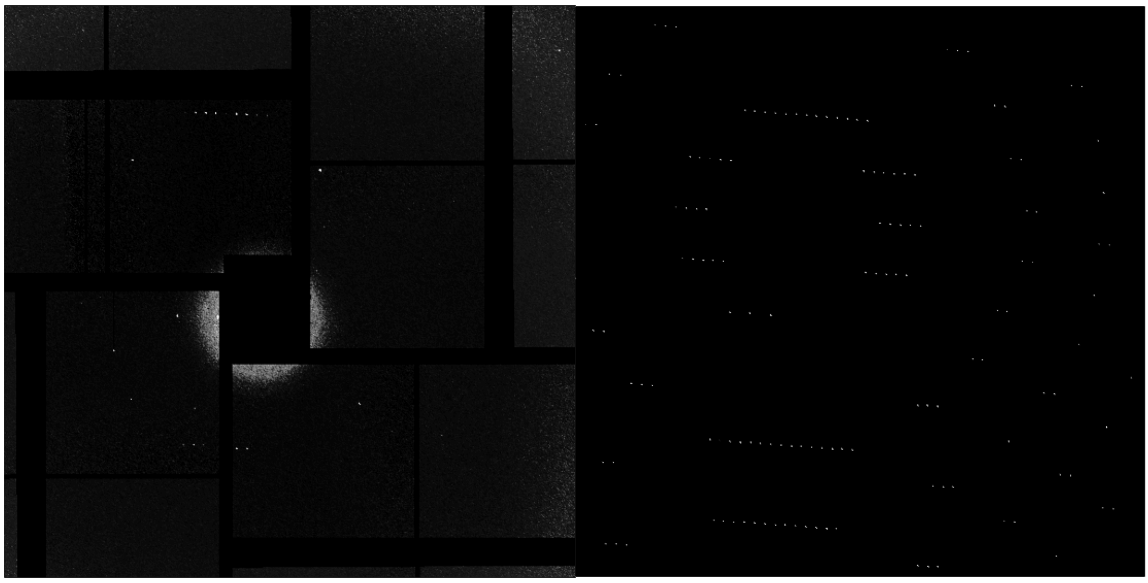

(a) (b)

Fig. 4.9. Experimental diffraction pattern from 5-HT2B receptor protein crystal (Liu et al., 2013) indexed using sparse pattern auto indexer. (a) Assembled diffraction pattern r0034_211432_bd9.h5. (b) Simulated pattern with predicted Bragg peaks from the reconstructed orientation provided by the sparse pattern auto-indexer. Most peaks in the experimental pattern are matched with the predicted ones.

Statistics of auto-indexing for I3C data set

It is has been shown that the new auto-indexer for sparse patterns not only work for simulated data with 100% indexing rate, but also can be applied to experimental data in protein crystallography. To estimate the indexing effectiveness and efficiency for a whole data set, the indexing statistics of "indexamajig" module from CrystFEL and the sparse

pattern auto-indexer are compared for I3C data set collected from beam time LJ69 at LCLS. The first 200 patterns from run 78 that are identified as hits are selected as the sample set. Among these 200 hits, 38 were indexed by "indexamajig" module; 122 were indexed by the sparse pattern auto-indexer; and 34 patterns are indexed by both modules (Fig. 4.10). One question that naturally comes up to this point is are the solutions given by the sparse pattern indexer correct, reliable and accurate. After comparing the orientation matrices from two modules for these 34 patterns, 24 out of them are considered to have consistent indexing solutions, and 4 patterns with inconsistent results. It is interesting that for the other patterns, one of the three reciprocal basic vectors matches between the two modules while the other two do not. A detailed analysis is needed to reveal the reason for this inconsistency. However, a speculative reason could be the insufficient number of peaks that lead the Fourier transform based indexing algorithm to find one correct basis vector but mistake for the others. Other possibilities include the fake artifact pixels that are mistaken for Bragg peaks. Despite these problems, the sparse pattern auto-indexer generally yields an average indexing rate of 65%, approximately 3 times that from CrystFEL pipeline.

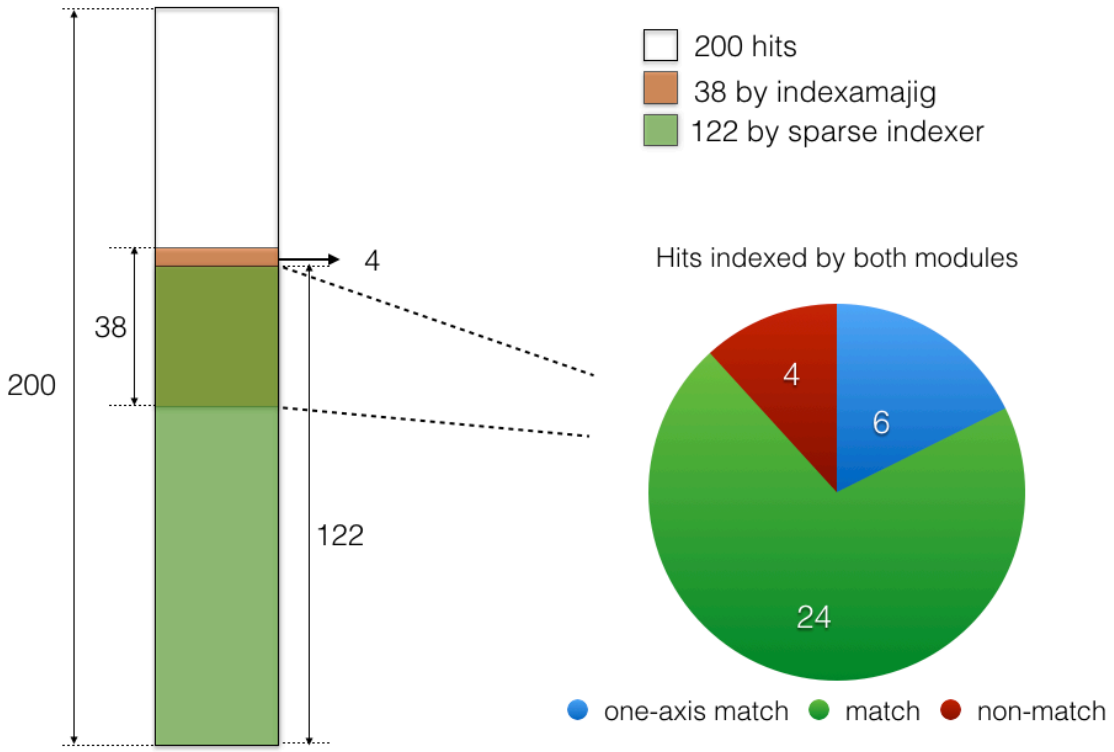

Fig. 4.10. Statistics of auto-indexing for run 78 of beam time LJ69 at LCLS. First 200 patterns identified as hits were selected out of a total number of 543 patterns in run 78. 38 patterns out of 200 were auto-indexed by "indexamajig" module of CrystFEL; 122 patterns were indexed by the sparse pattern auto-indexer; 34 patterns were indexed by both modules. The two auto-indexer modules give consistent orientation matrix (match) for 24 patterns, inconsistent indexing solutions (non-match) for 4 patterns, and match along one of the reciprocal lattice basis directions for 6 patterns.

Orientation determination using Bragg intensity

Diffraction patterns from photosynthesis II (PS II) are simulated (Fig. 4.11(a)) for 9

keV photon energy with resolution limit of 20 Å. Poisson noise are then added to the pattern to degrade the resolution so that less than 15 Bragg peaks can be identified in each pattern (Fig. 4.11(b)). To start the orientation reconstruction, a few random orientations are selected as the initial solutions in the genetic algorithm illustrated in Fig. 4.7. The grid spacing of Euler angle space is set to 5 degrees so that computation time is sensible. Random mutations within 1 degree in Euler angles are allowed with a controlled probability. Since genetic algorithm is a randomized, the reconstruction program was run for multiple times. Generally, 12 to 17 iterations were generally needed to achieve an acceptable solution. With a properly defined fitness function that is basically a combination of intensity correlation coefficients and symmetry of the "virtual rocking curve", the landscape of the searching space can be relatively smooth in the vicinity of correct orientation (Fig. 4.12(a)). The accuracy of the reconstructed orientation depends on the searching landscape and in this case is $\Delta\boldsymbol{\varphi}=0.6,\Delta\boldsymbol{\theta}=0.4,\Delta\boldsymbol{\alpha}=0.05$. One problem of this genetic algorithm based approach is the relatively long computation time. The computation time is at the level of 10^4 s for each pattern with 2.7 GHz Intel Core i7 CPU, 16GB RAM, in MATLAB environment.

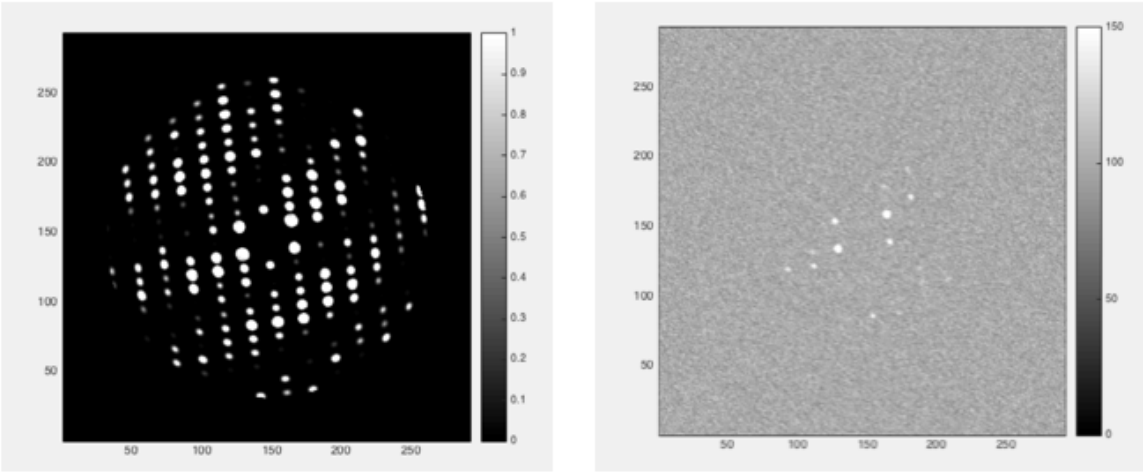

(a) (b)

Fig. 4.11. Simulated diffraction patterns for Photosynthesis (PS2) at the photon energy of 9keV with the resolution limit of 20Å. [a,b,c]=[122,228,286]Å . (a) before adding Poisson noise and background. (b) with Poisson noise and background comparable to experimental condition. Resolution is reduced significantly by Poisson noise, only less than 15 Bragg spots are identified for an individual pattern.

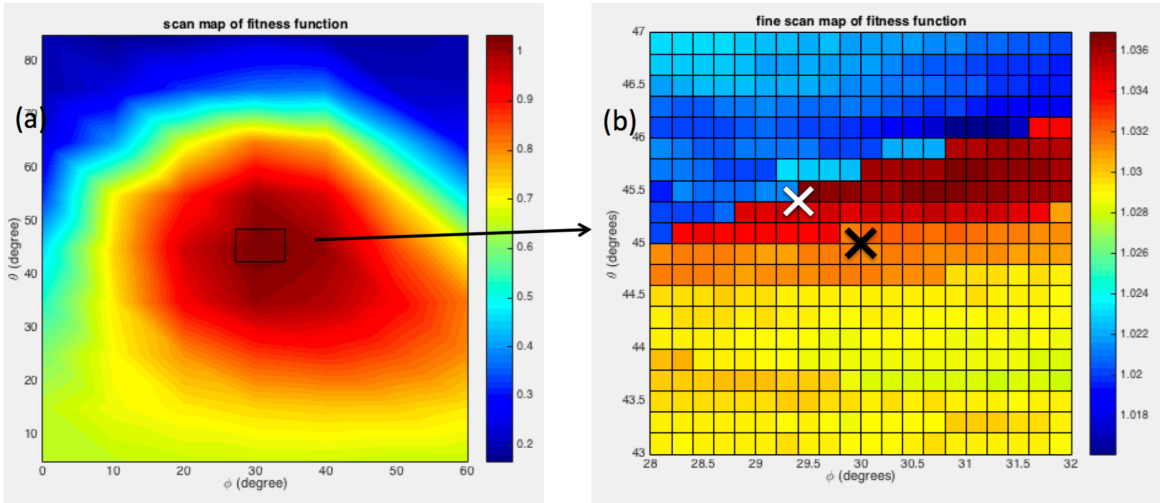

(a) (b)

Fig. 4.12. Landscape of the GA searching process. (a) Fitness value as function of Euler angles. (b) Zoomed in profile for the boxed region in (a). White cross indicates the solution; black cross indicates the true orientation.

Combining geometrical information and intensity correlation in orientation refinement

Accurate orientation is essential to effective partiality correction and hence intensity measurement. Geometrical information such as the peak positions cannot give sufficiently accurate orientation that facilitates effective partiality estimate and correction. Intensity correlation approach helps fine tuning the orientation, but can be very computationally expensive if used independently. Therefore, a natural idea would be to combine the advantage of fast auto-indexing using geometry and the superior accuracy provided by intensity. Bragg peaks are assumed to be exactly on Ewald sphere in auto-indexing stage, however there is an offset between the center of Bragg order and the Ewald sphere. This offset can be corrected by iteratively rocking the crystal slight about the scattering vectors that corresponds to Bragg peaks on the pattern, until the intensity correlation between the pattern and model is maximized (Fig. 4.13). Orientation matrix provided by auto-indexers from geometry can be used as the starting point in the rocking series.

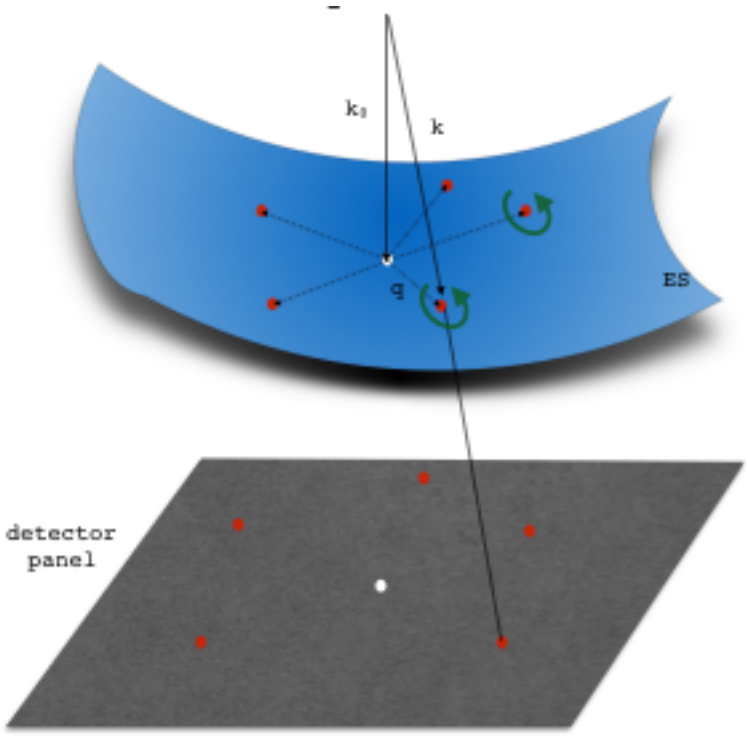

Fig. 4.13. Maximize intensity correlation by iteratively rocking about scattering vectors.

CHAPTER 5

DYNAMICAL INVERSION FROM ELECTRON DIFFRACTION

Introduction

The dynamical inversion problem in transmission electron diffraction can be described as the inverse problem of electron multiple elastic scattering (dynamical diffraction). It has recently received renewed interest in applications such as solving nanocrystals and imaging biomolecules with X-rays (Spence et al., 2012). The aim of dynamical inversion is to reconstruct the object crystal potential (charge density in the case of X-ray scattering) from measured intensity of a transmission diffraction pattern under the multiple-scattering condition. Strong multiple scattering effect prevents direct inversion from the diffraction pattern to a real space object by Fourier transformation (FT) because the first Born approximation (single scattering) is no longer valid (Spence, 2008). Conversely, the dynamical diffraction intensity is sensitively dependent on the phases of crystal structure factors due to the interference between Bragg beams, which suggests the feasibility of dynamical inversion or even probing the phases. A variety of approaches have been reported on inversion from intensity of FT in kinematical diffraction. Since the real space object, estimated from the inverse FT of the measured diffraction intensity, could give the phases of the FT, the inversion from known FT moduli is commonly referred to as phase retrieval. Popular algorithms used are the Gerchberg-Saxton

algorithm for two intensity measurements, error-reduction algorithm, steepest-descent method koch method(Van Den Broek & Koch, 2012), gradient search methods, input-output algorithms (for a comparison of these methods, see (Fienup, 1978, 1982)).

Unfortunately, these frequently used algorithms cannot be directly applied to the dynamical inversion problem simply because the FT relationship between the structure factors and the diffraction data is destroyed by the multiple scattering effect. Although the linear transformation between the real space object and experimental diffraction data may not be necessary, great difficulties still hinder the generalization of existent well-studied algorithms to dynamical inversion. This is because the transformation between the real space object and its diffraction pattern must be a one-to-one mapping without ambiguity, regardless of the properties of the transformation that is not the case in the dynamical inversion. Therefore, it is helpful to study the mathematical properties of the transformation between the real space object (or structure factors) and the dynamical diffraction pattern. In this report, a mathematical model of forward scattering as well as the inversion problem are analyzed based on the Bloch-wave approach with reasonable approximations (John C.H. Spence & Zuo, 1992). Properties of symmetry, othornormality, trace, and determinant are explored for structure matrix A, scattering matrix S and eigenvector matrix C. These results might guide us to design new algorithms for dynamical inversion and allow us to analyze an algorithm's convergence and stability. Several trial algorithms are described and carried out in numerical

experiments before rigorous mathematical understanding and proofs. Additionally an inversion method for two or more specimen thickness is proposed which may eliminate the ambiguity in the transformation from S matrix to A matrix. This implies that it might be possible to apply the existent well-studied algorithms to dynamical inversion such as the error reduction, or generalized projection method(J. C. H. Spence, Calef, & Zuo, 1999), if properly modified.

Due to its paramount importance in crystallography, multiple-elastic-scattering has been studied extensively by numerous researchers with various independent approaches. Examples include the multislice approach, Bloch wave approach and scattering matrix approach etc. Although the dynamical inversion problem has been discussed in other approaches such as steepest-descent method in the artificial neural network (ANN) multi-slice approach (Van Den Broek & Koch, 2012), the Bloch-wave approach is the most relevant to the dynamical inversion problem because of its accuracy and simplicity. The following mathematical descriptions of multiple elastic scattering and inversion, as well as the subsequent analysis, are based on the Bloch-wave approach.

Bloch-wave formulation of forward scattering

Electron behavior in elastic forward scattering can be described by the relativistic-corrected Schrodinger equation as follows(John C.H. Spence & Zuo, 1992):

$$\frac{-h^2}{8\pi^2 m}\nabla^2\Psi(\mathbf{r}) - |e|V(r)\Psi(\mathbf{r}) = \frac{h^2K_0^2}{2m}\Psi(\mathbf{r}) \tag{5.1}$$

where K_0 is the incident electron wavevector.

Expand the wave-function as a sum of Bloch waves and crystal potential as a Fourier series:

$$\Psi(\mathbf{r}) = \sum_i c_i \exp\left(2\pi i \mathbf{k}^{(i)} \cdot \mathbf{r}\right) \sum_{\mathbf{g}} C_g^i \exp(2\pi i \mathbf{g} \cdot \mathbf{r}) \tag{5.2}$$

$$V(\mathbf{r}) = \frac{h^2}{2m|e|} U(\mathbf{r}) = \frac{h^2}{2m|e|} \sum_{\mathbf{g}} U_{\mathbf{g}} \exp\,(2\pi i \mathbf{g} \cdot \mathbf{r}) \tag{5.3}$$

where **g** denotes reciprocal lattice vectors.

Combine Eqn. (5.1), (5.2) and (5.3). The Schrodinger equation is cast in the form of an eigenvalue equation:

$$2KS_g C_g^i + \sum_{\mathbf{h}} U_{\mathbf{g}-\mathbf{h}} C_{\mathbf{h}}^i = 2K_n \gamma^i C_{\mathbf{g}}^i \tag{5.4}$$

or in matrix form

$$\mathbf{A}\mathbf{C}^i = 2K_n \gamma^i \mathbf{C}^i \tag{5.5}$$

where S_g denotes excitation errors and γ^i denotes dynamical dispersion constants. The A matrix is composed of diagonal elements dependent on excitation errors S_g and off-diagonal elements U_{g-h} which are structure factors determined completely by the crystal potential. Back scattering effects have been neglected in the above derivation.

In the Darwin representation, the exit wave-function can be expressed as a sum of plane waves each with the wave-vector of **K**+**g**:

$$\Psi(\mathbf{r}, t) = \sum_{\mathbf{g}} \phi_{\mathbf{g}}\,(t) \exp\,[2\pi i(\mathbf{K} + \mathbf{g}) \cdot \mathbf{r}] \tag{5.6}$$

where t is the crystal thickness $\phi_{\mathbf{g}}$ is the amplitude of the corresponding plane wave component and

$$\phi_{\mathbf{g}}(t) = \sum_{i=1}^{n} c_i C_{\mathbf{g}}^i \exp\,(2\pi i \gamma^i t) \tag{5.7}$$

Coefficients c_i can be determined by solving eq. (7) at t=0 (crystal entrance surface). Substituting c_i back into eq. (7), we have:

$$\begin{pmatrix} \phi_0(t) \\ \mathrm{M} \\ \phi_g(t) \\ \mathrm{M} \end{pmatrix} = C \begin{pmatrix} \exp(2\pi i\gamma^1 t) & \mathrm{L} & 0 \\ \mathrm{M} & \mathrm{O} & \mathrm{M} \\ 0 & \mathrm{L} & \exp(2\pi i\gamma^n t) \end{pmatrix} C^{-1} \begin{pmatrix} \phi_0(0) \\ \mathrm{M} \\ \phi_g(0) \\ \mathrm{M} \end{pmatrix} \tag{5.8}$$

C matrix is the eigenvector matrix of A.

If we define the scattering matrix as

$$\begin{aligned} S(t) &= C \begin{pmatrix} \exp(2\pi i\gamma^1 t) & \mathrm{L} & 0 \\ \mathrm{M} & \mathrm{O} & \mathrm{M} \\ 0 & \mathrm{L} & \exp(2\pi i\gamma^n t) \end{pmatrix} C^{-1} \\ &= C\left\{\exp(2\pi i\gamma t)\right\} C^{-1} \\ &= C\left\{\lambda\right\} C^{-1} \end{aligned} \tag{5.9}$$

Then the entrance wave is related to the exit wave by S

$$\begin{pmatrix} \phi_0(t) \\ \mathrm{M} \\ \phi_g(t) \\ \mathrm{M} \end{pmatrix} = S(t) \begin{pmatrix} \phi_0(0) \\ \mathrm{M} \\ \phi_g(0) \\ \mathrm{M} \end{pmatrix} \tag{5.10}$$

It is clearly shown by eq. (10) that with knowledge of the scattering material and geometry dynamical diffraction is a linear response system. Every column of S(t) matrix gives a diffraction pattern for an incident plane wave. This linearity allows the moduli of S matrix elements to be completely determined by diffraction experiments with various scattering geometry conditions that are the basis of the dynamical inversion.

Symmetries of A and S

From the above discussion we can see that dynamical diffraction is completely determined by S or A matrix for given incident electron wave $\begin{pmatrix} \phi_0(0) \\ \text{M} \\ \phi_g(0) \\ \text{M} \end{pmatrix}$. In this sense, the dynamical inversion is actually aimed at seeking the right complex A and S matrix with both moduli and phases. Since only the moduli of S matrix elements are known from diffraction experiments, there are n^2 unknown phases. Even for a relatively low energy of 30keV n would be more than 200. It is impossible to solve for the n^2 unknown phases analytically with no further information other than moduli of S matrix elements. Therefore, it is necessary to think of utilizing the mathematical properties such as symmetries of this Bloch-wave model as further constraints to determine A and S.

A matrix is composed by the diagonal elements $2KS_g$ and the off-diagonal elements $U_{\mathbf{g-h}}$. For a choice of 2-dimensional symmetric set of $\mathbf{g}$ vectors, S_g should be also symmetric, i.e. $S_g = S_{-g}$, which means the diagonal of A, is symmetric about its anti-diagonal. However, for a 3-D symmetric set of $\mathbf{g}$ vectors this symmetry is no longer there. The symmetry of $U_{\mathbf{g-h}}$ is dependent on crystal potential since they are related by FT. Ignoring the absorption effect if the crystal is centric, $U_{\mathbf{g-h}} = U_{\mathbf{h-g}}$ and are real while if the crystal is accentric, $U_{\mathbf{g-h}} = U^*_{\mathbf{h-g}}$ and are complex. Additionally, due to the symmetry of the set of $\mathbf{g}$ vectors, any pair of entries of A which are symmetric about the anti-diagonal are the same $U_{\mathbf{g-h}}$. To summarize, the diagonal of the A matrix has

anti-diagonal symmetry in case of a 2-D set of **g** vectors and the off-diagonal elements of A have both diagonal and anti-diagonal symmetries for centric crystals. A is always Hermitian regardless of crystal symmetry.

The symmetry of the S matrix can be analyzed according to its relation with A. According to matrix theory, eq. (9) could be rewritten in the form of a function of matrices:

$$\begin{aligned} S(t) &= C\left\{\exp(2\pi i\gamma t)\right\}C^{-1} \\ &= C\{\lambda\}C^{-1} = \exp(i\frac{2\pi}{2K_n}At) \end{aligned} \tag{5.11}$$

Since S is matrix function of only A, there are no commutativity issues to be considered here. Hence S should have the same symmetry as A (i.e. diagonal symmetry).

Schur-decompostion of A and S and related properties

According to Eqn. (5.5), matrix A could be Schur-decomposed into the following form:

$$\begin{aligned} A &= C\begin{pmatrix} \gamma^1 & \mathrm{L} & 0 \\ \mathrm{M} & \mathrm{O} & \mathrm{M} \\ 0 & \mathrm{L} & \gamma^n \end{pmatrix}C^{-1} \\ &= C\{\gamma/2K_n\}C^{-1} \end{aligned} \tag{5.12}$$

where C is the eigenvector matrix of A, and $\{\gamma/2K_n\}$ is the eigenvalue matrix. For the case of centric crystals, A is real and $A = A^T$. C is an orthonormal (i.e. $C^T = C^{-1}$) real matrix and $\{\gamma\}$ is also real.

S can also be Schur-decomposed as:

$$
\begin{aligned}
S(t) &= C\begin{pmatrix} \exp(2\pi i\gamma^1 t) & \mathrm{L} & 0 \\ \mathrm{M} & \mathrm{O} & \mathrm{M} \\ 0 & \mathrm{L} & \exp(2\pi i\gamma^n t) \end{pmatrix} C^{-1} \\
&= C\left\{\exp(2\pi i\gamma t)\right\} C^{-1} \\
&= C\left\{\lambda\right\} C^{-1}
\end{aligned} \tag{5.9}
$$

From Schur-decompostions of A and S, some properties can be found based on matrix theory.

1. Generally, for a Hermitian A, there must exist a unitary C ($C^{\dagger} = C^{-1}$) to diagonalize it. Specifically for centric crystals, A is diagonal symmetric, C is orthonormal and real ($C^{T} = C^{-1}$).

2. Eigenvalue matrix $\{\gamma / 2K_n\}$ of Hermitian A is real.

3. S and A share the same eigenvector matrix C. Specifically for centric crystals, $C^{T} = C^{-1}$ and is real. Column vectors of the C matrix form an orthonormal basis set.

4. Eigenvalues of S $\left\{\lambda\right\} = \left\{\exp(2\pi i\gamma t)\right\}$ are complex and have unit moduli.

5. S is unitary. $S^{\dagger} = S^{-1}$. Proof:

$$S = \exp(i\frac{2\pi}{2K_n}At)$$

$$S^{\dagger} = [\exp(i\frac{2\pi}{2K_n}At)]^{\dagger} = [\sum_n \frac{1}{n!}(i\frac{2\pi}{2K_n}At)^n]^{\dagger} = \sum_n \frac{1}{n!}[(-i\frac{2\pi}{2K_n}A^{\dagger}t)]^n$$

$$= \exp(-i\frac{2\pi}{2K_n}A^{\dagger}t)$$

$$= \exp(-i\frac{2\pi}{2K_n}At)$$

$$SS^{\dagger} = \exp(i\frac{2\pi}{2K_n}At)\exp(-i\frac{2\pi}{2K_n}At) = 1$$

$$S^{\dagger} = S^{-1}$$

6. Determinant of S(t) is related to the trace of A by:

$$\det(S(t)) = \exp(i2\pi\omega t)$$

$$\omega = \frac{tr(A)}{2K_n} \qquad (5.13)$$

Proof:

$$\det(S(t)) = \det(C\{\lambda\}C^{-1}) = \det(\{\lambda\})$$

$$= \prod_i \exp(i2\pi\gamma^i t) = \exp(i(\frac{2\pi}{2K_n}t)\sum_i \gamma^i)$$

$$= \exp(i2\pi\frac{tr(A)}{2K_n}t)$$

Moreover, if U_0=0, then $\omega = \sum_g S_g$.

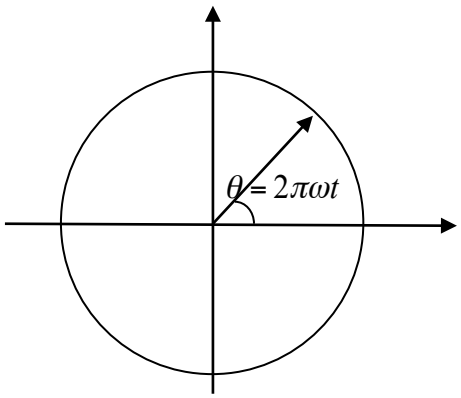

Fig. 5.1. Determinant of S: Unit vector in the complex plane.

Determinant of S(t) is complex number with unit modulus and phase $\theta = 2\pi\omega t$ as shown in the diagram above. The angular frequency is determined by the trace of A matrix i.e. the scattering geometry. Determinant of S(t) turns out to be a periodic function of thickness t.

Uniqueness

One question we would ask while working on dynamical inversion is whether we could get to the "right" S or A matrix by numerical methods with constraints related to the properties of the mathematical system discussed above? Or in other words, will the 6 properties listed above make sufficient constraints to get unique S and A?

Crystal potential and the choice of origin together determine the structure factors $U_{\mathbf{g-h}}$. Even for centric crystals, if the origin is not chosen with the highest symmetry, $U_{\mathbf{g-h}}$ could be complex while the A matrix is still Hermitian. From physics, we can see that the choice of origin should not affect the dynamical diffraction. This means if we change the origin, the absolute phases of Bragg beams would change but not the differences between them, nor the amplitudes. Therefore, without additional constraints A will not be uniquely retrieved from given moduli of S. However, if we impose the reality and orthornomality to the C matrix (1) and the determinant relationship (6) in the potential algorithms A will turn out to be real and symmetric. In this way, the ambiguity of the choice of origin is eliminated.

In most phase retrieval algorithms, the only constraint on complex S with known moduli is its unitarity. However, it has been reported that for a large size matrix with given moduli, phase retrieval to a unitary matrix is not unique (Auberson, 1989). For a symmetric S matrix of order n with given modulus $|S|$, the phases which make S unitary should satisfy the following conditions:

$$\sum_{k}^{n} |S|_{i,k} |S|_{j,k} \exp(i(\theta_{i,k} - \theta_{j,k})) = 0 \quad (for\ i \neq j)$$
$$\theta_{i,j} = \theta_{j,i} \tag{5.14}$$

There are $\frac{n(n-1)}{2}$ of the first equation of (14) and $\frac{n(n-1)}{2}$ of the second equation of (14). For the n^2 unknown phases, these equations leave at least *n* degrees of freedom. Fortunately, for centric crystals with absorption ignored, the symmetries of A together with reality and orthonormality of C could serve as further constraints to the retrieval process.

Based on the mathematical analysis in the above section, several algorithms have been tried to either retrieve phases of the S matrix or reconstruct the A matrix. The following discussions of various algorithms have not been analyzed from the aspect of stability or convergence behavior; instead, numerical experiments were directly carried out and analyzed. The following two algorithms are most promising.

Expectation-maximization-compression (EMC)

EMC has been given lots of attentions since its invention due to its great power in retrieving partial lost information from incomplete data by iteratively (Dempster, Laird, & Rubin, 1977; Sundberg, 1974). Recently it was used to reconstruct images from sparse sample data (Loh & Elser, 2009; Philipp et al., 2012). EMC could be applied to reconstructing the lost phase information from incomplete intensity data that exactly defines the dynamical inversion problem. The essence of EMC is to start with an initial assumed function, and correct it with incomplete data based on some probability model

(Poisson distribution in the work of Phillip et. al.(Philipp et al., 2012)) in each iteration until it converges to function which gives complete data consistent with the known incomplete data. However, dynamical inversion should is a deterministic problem rather than a stochastic one because diffraction intensity can be exactly determined given all the necessary information. Furthermore, an assumed A matrix could give an estimated S matrix but it is not obvious how to find a way to correct A using the existent data.

Phase retrieval for single S with constraints

It is mentioned in the theory section above that a unitarity constraint is insufficient in phase retrieval for S matrix with known moduli. However, for centric crystals, stronger additional constraints could be applied: reality and orthonormality of eigenvector matrix C and diagonal symmetry of S. Using all the constraints, an iterative algorithm was devised and its flow diagram (Fig. 5.2) is shown.

The error metric is chosen to be the 2-norm of the difference between the estimated S and the true S: $Error = norm(S^{es} - S)$. To monitor the convergence behavior of this iterative algorithm, the error was calculated at each iteration step (shown in Fig. 5.3). The error decreased monotonically with iteration number. In the first 4 iterations, the error decreased rapidly from 2.0553 to 2.0032, and for the consequent iterations the decrease was very slow. Even after 2000 iterations, the error could only be reduced to 2.0026. If this error reduction rate remains the same, it would take an estimated time of 347 days (mac in our lab 3.6GHz CPU, 8GB RAM) until the errors goes to an acceptably small

value (<0.1).

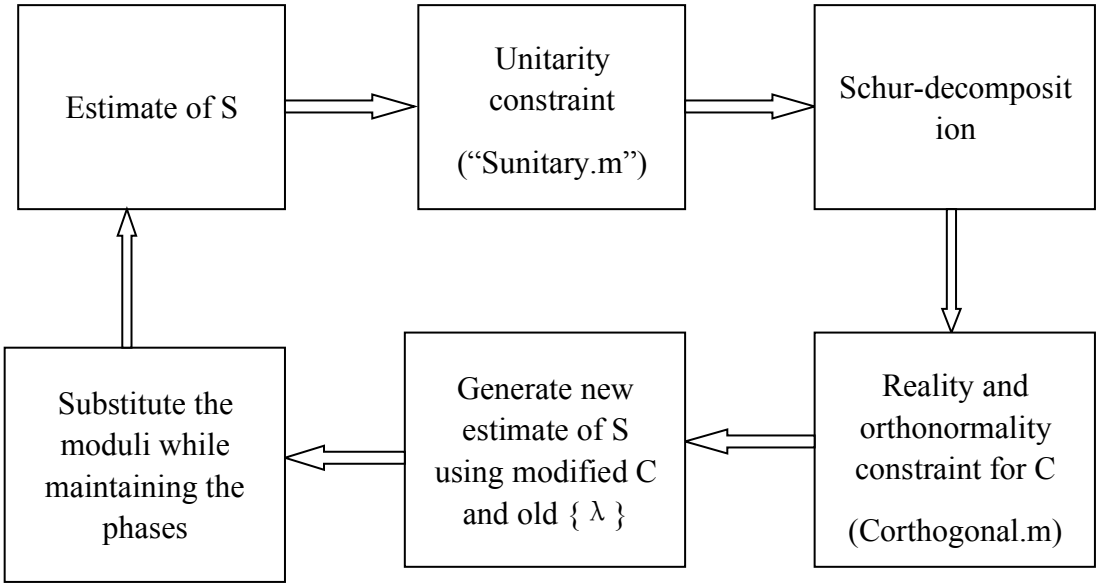

Fig. 5.2. Flowchart of phase retrieval for single S matrix. ("inversion7.m")

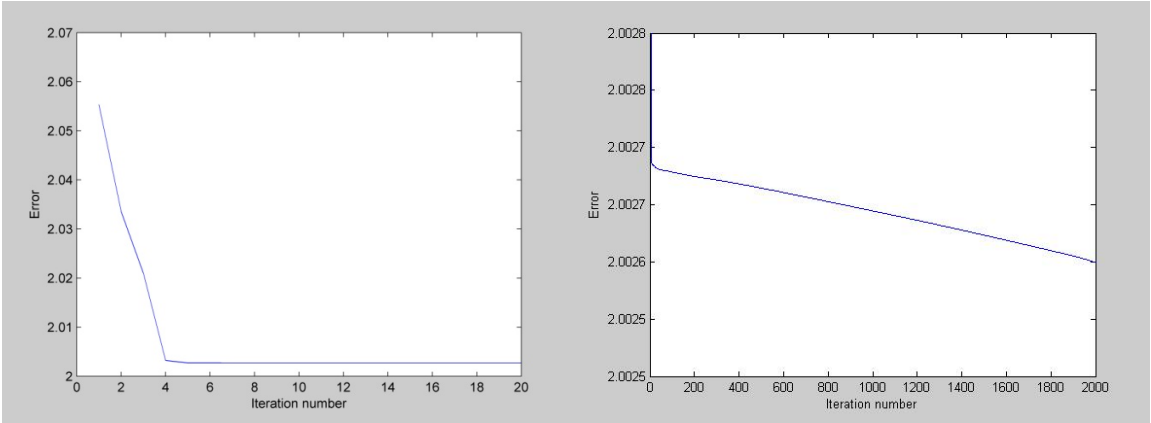

(a) (b)

Fig. 5.3. Convergence behavior of phase retrieval for single S matrix. ("inversion7.m")

(a)Error in the first 20 iterations; (b)Error in 2000 iterations

A possible reason for the slow error reduction may be the insufficient use of data. There are further constraints that could be applied. For example, in the phase retrieving process, the symmetry of the A matrix (off-diagonal elements are symmetric about both diagonal and anti-diagonal) could not be embedded in the algorithm because of the ambiguity of going from S to A. Also, only moduli of one S matrix of single thickness and scattering geometry was used as the experimental data. We can imagine that all S matrices must correspond to the same A matrix if they have same scattering geometry and even if they have different scattering geometries they will still share the same off-diagonal elements (structure factors) of A. Therefore, it is worth thinking of using moduli of many S matrices with various thicknesses or multiple scattering geometries in the reconstruction of A.

Inversion from two thicknesses or wavelengths

After realizing the low efficiency of phase retrieval for a single S as discussed above, other inversion algorithms that make use of multiple S matrices are explored in this section.

Note that the S matrix forms a subgroup of unitary group of order n. Additionally multiplication operation in this group is commutative i.e. $S(t_1)S(t_2) = S(t_2)S(t_1)$ since $S(t_1)$ and $S(t_2)$ have the same real orthonormal C matrix. Consider $S(t + \Delta t)$,which can be expanded about t as follows (Spence, 2008):

$$S(t+\Delta t) = S(t)S(\Delta t) = S(t)\exp(i\frac{2\pi}{2K_n}A\Delta t)$$
$$= S(t)(\mathbf{1} + i\frac{2\pi}{2K_n}\Delta tA) \quad (5.15)$$
$$= (\mathbf{1} + i\frac{2\pi}{2K_n}\Delta tA)S(t)$$

This expansion is a good approximation when $\omega t = 1$ is satisfied.

Eq (15) provides a simpler relation between A and S matrices than the previous definition of S in eq. (11). The advantage of eq. (15) is its computational simplicity and elimination of ambiguity. Inversion from the moduli of $S(t)$ and $S(t+\Delta t)$ is also experimentally feasible because varying the wavelength of the electron source is equivalent to changing the thickness of specimen under the non-relativistic condition (Spence, 2008). The algorithm was devised accordingly with its flow diagram shown in Fig. 5.4.

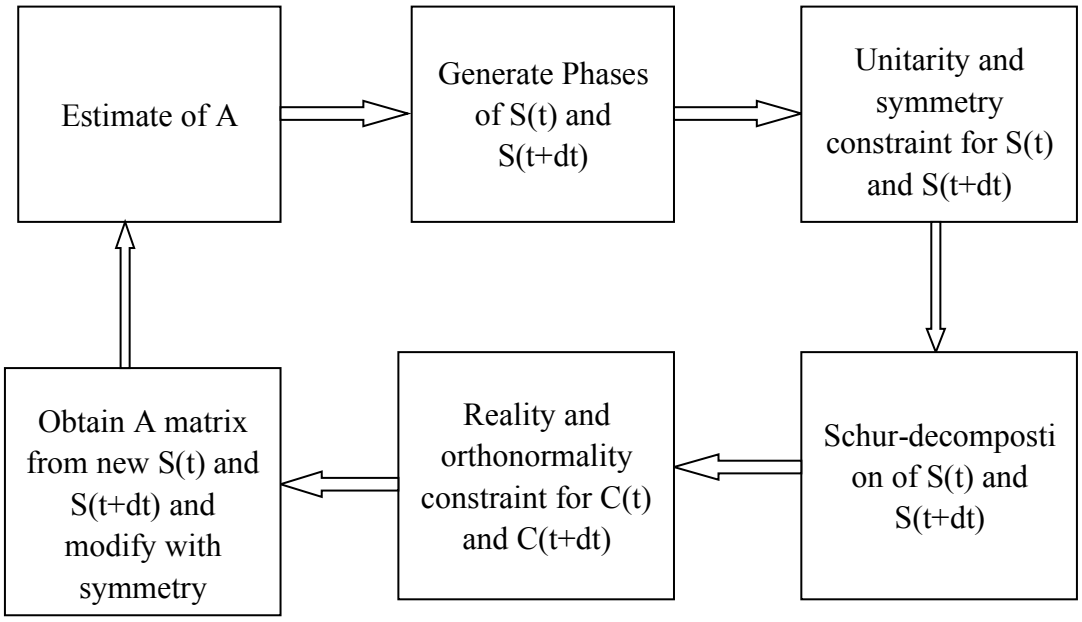

Fig. 5.4. Flowchart of inversion from two thicknesses. ("inversion8.m")

As is shown in Fig. 5.5, the algorithm does not converge as expected; instead the error quickly diverges, then fluctuates about the value 3000. This means an arbitrary initial guess of the A matrix could diverge very quickly from the true A in this algorithm. After checking the A matrix after each iteration, it was found that most matrix elements have the right order of magnitude compared to the true A with approximately 10% of the elements being singular. It is the singularities that make the error so large.

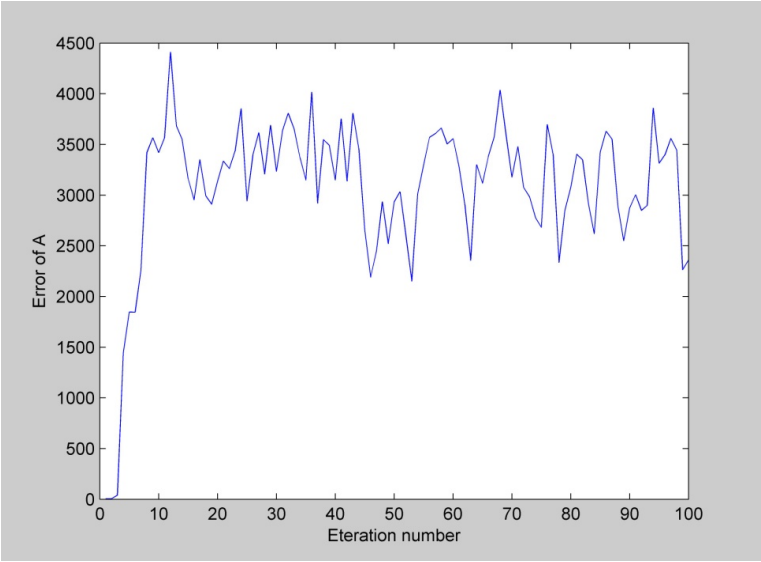

Fig. 5.5. Convergence behavior of inversion from two thicknesses. (“inversion8.m”)

Divergence of “inversion8.m” could possibly be avoided by considering the following: first, the way the unitarity constraint for S was applied (“Sunitary.m”) is not necessarily by “minimum adjustment” (generalized projection method) (Spence et al., 1999) from previous assumed S phases. Hence, it is not guaranteed that the next estimate of S does not “jump” too far away from the previous estimate so that it is converging to the true value. Second, there is one important property that cannot be easily used: A and

S share the real eigenvector matrix C. But it is not straightforward to find a way to compare and correct C of A and S because the order of eigenvalues or eigenvectors in $\{\gamma\}$, $\{\lambda\}$ and C is random when solving the eigenvalue problem in Matlab. The same C of A and S can also guarantee the commutativity of S.

Conclusions and prospects

The aim of this work is to inverse the dynamical electron diffraction to the real space crystal potential. Well-studied phase retrieval algorithms cannot be directly applied in the dynamical inversion problem because of multiple scattering effect which breaks the FT relationship between a diffraction pattern and crystal potential. The multislice approach and Bloch-wave approach have been used to describe multiple scattering and the latter was chosen for dynamical inversion in this work. The mathematical properties of structure matrix A and scattering matrix S have been analyzed including symmetry, determinant, eigenvalues and eigenvector matrix. Using constraints based on these properties, inversion from moduli of single S matrix and inversion from moduli of S matrices of multiple thicknesses were explored. One still needs to overcome the low efficiency and divergence of these two trial algorithms to achieve success.

These two algorithms could be improved in the following ways: Firstly, think of a new method of imposing the unitarity constraint (Sunitary.m) that is based on the "minimum adjustment" and guarantees convergence. Secondly, work out a method to sort

the eigenvalues and eigenvectors in a certain order so that comparison and correction of eigenvector matrix C are feasible. Dynamical inversion can be solved if this module successfully finds a common real and orthogonal C matrix.

REFERENCES

Ackermann, W., Asova, G., Ayvazyan, V., Azima, A., Baboi, N., Bähr, J., … Zapfe, K. (2007). Operation of a free-electron laser from the extreme ultraviolet to the water window. *Nature Photonics*, *1*(6), 336–342. http://doi.org/10.1038/nphoton.2007.76

Aquila, A., Hunter, M. S., Doak, R. B., Kirian, R. A., Fromme, P., White, T. A., … Chapman, H. N. (2012). Time-resolved protein nanocrystallography using an X-ray free-electron laser. *Optics Express*, *20*(3), 2706–2716.

Auberson, G. (1989). On the reconstruction of a unitary matrix from its moduli. Existence of continuous ambiguities. *Physics Letters B*, *216*(1–2), 167–171. http://doi.org/10.1016/0370-2693(89)91389-0

Ayyer, K., Philipp, H. T., Tate, M. W., Elser, V., & Gruner, S. M. (2014). Real-Space x-ray tomographic reconstruction of randomly oriented objects with sparse data frames. *Optics Express*, *22*(3), 2403–13. http://doi.org/10.1364/OE.22.002403

Barty, A., Caleman, C., Aquila, A., Timneanu, N., Lomb, L., White, T. a., … Chapman, H. N. (2011). Self-terminating diffraction gates femtosecond X-ray nanocrystallography measurements. *Nature Photonics*, *6*(1), 35–40. http://doi.org/10.1038/nphoton.2011.297

Barty, A., Kirian, R. a., Maia, F. R. N. C., Hantke, M., Yoon, C. H., White, T. a., & Chapman, H. (2014). Cheetah: Software for high-throughput reduction and analysis of serial femtosecond X-ray diffraction data. *Journal of Applied Crystallography*, *47*(3), 1118–1131. http://doi.org/10.1107/S1600576714007626

Beck, T., & Sheldrick, G. M. (2008). 5-Amino-2,4,6-triiodo-isophthalic acid monohydrate. *Acta Crystallographica Section E: Structure Reports Online*, *64*(7). http://doi.org/10.1107/S1600536808017741

Bevington, P. R., & Robinson, D. K. (1992). *Data reduction and error analysis for the physical sciences*. (S. J. Tubb & J. M. Morriss, Eds.) (2nd editio). McGraw-Hill, Inc.

Campbell, J. W. (1998). The Practicality of Using a Three-Dimensional Fast Fourier Transform in Auto-Indexing Protein Single-Crystal Oscillation Images. *Journal of Applied Crystallography*, *31*(3), 407–413. http://doi.org/10.1107/S0021889897014453

Chapman, H. N. (2009). X-ray imaging beyond the limits. *Nature Materials*, *8*(4), 299–301. http://doi.org/10.1038/nmat2402

Chapman, H. N., Fromme, P., Barty, A., White, T. a, Kirian, R. a, Aquila, A., … Spence, J. C. H. (2011). Femtosecond X-ray protein nanocrystallography. *Nature*, *470*(7332), 73–7. http://doi.org/10.1038/nature09750

Congreve, M., Murray, C. W., & Blundell, T. L. (2005). Keynote review: Structural biology and drug discovery. *Drug Discovery Today*, *10*(13), 895–907. http://doi.org/10.1016/S1359-6446(05)03484-7

Cowley, J. M., & Spence, J. C. H. (1981). Convergent beam electron microdiffraction from small crystals. *Ultramicroscopy*, *6*(1), 359–366. http://doi.org/10.1016/S0304-3991(81)80222-7

Dempster, A. P., Laird, N. M., & Rubin, D. B. (1977). Maximum likelihood from incomplete data via the EM algorithm. *Journal of the Royal Statistical Society*, *B*, 1–38. http://doi.org/10.2307/2984875

DePonte, D. P., Weierstall, U., Starodub, D., Schmidt, K., Spence, J. C. H., & Doak, R. B. (2008). Gas Dynamic Virtual Nozzle for Generation of Microscopic Droplet Streams. *Journal of Physics D: Applied Physics*, *41*(195505), 7. http://doi.org/10.1088/0022-3727/41/19/195505

Emma, P., Akre, R., Arthur, J., Bionta, R., Bostedt, C., Bozek, J., … Galayda, J. (2010). First lasing and operation of an a ̊ngstrom-wavelength free-electron laser, *4*(August), 641–647. http://doi.org/10.1038/NPHOTON.2010.176

Fienup, J. R. (1978). Reconstruction of an object from the modulus of its Fourier transform. *Optics Letters*, *3*(1), 27–29. http://doi.org/10.1364/OL.3.000027

Fienup, J. R. (1982). Phase retrieval algorithms: a comparison. *Applied Optics*, *21*(15), 2758–2769. http://doi.org/10.1364/AO.21.002758

Frank, M., Carlson, D. B., Hunter, M. S., Williams, G. J., Messerschmidt, M., Zatsepin, N. a., … Evans, J. E. (2014). Femtosecond X-ray diffraction from two-dimensional protein crystals. *IUCrJ*, *1*(2), 95–100. http://doi.org/10.1107/S2052252514001444

Garman, E. F. (2013). Radiation damage in macromolecular crystallography: What is it and why do we care? *NATO Science for Peace and Security Series A: Chemistry and Biology*, 69–77. http://doi.org/10.1007/978-94-007-6232-9-7

Ginn, H. M., Brewster, A. S., Hattne, J., Evans, G., Wagner, A., Grimes, J. M., … Stuart, D. I. (2015). A revised partiality model and post-refinement algorithm for X-ray free-electron laser data. *Acta Crystallographica Section D Biological Crystallography*, *71*(6), 1400–1410. http://doi.org/10.1107/S1399004715006902

Ginn, H. M., Messerschmidt, M., Ji, X., Zhang, H., Axford, D., Gildea, R. J., … Stuart, D. I. (2015). Structure of CPV17 polyhedrin determined by the improved analysis of serial femtosecond crystallographic data. *Nature Communications*, *6*, 6435. http://doi.org/10.1038/ncomms7435

Hattne, J., Echols, N., Tran, R., Kern, J., Gildea, R. J., Brewster, A. S., … Sauter, N. K. (2014). Accurate macromolecular structures using minimal measurements from X-ray free-electron lasers. *Nature Methods*, *11*(5), 545–8. http://doi.org/10.1038/nmeth.2887

Hauptman, H. (1997). Phasing methods for protein crystallography. *Current Opinion in Structural Biology*, *7*(5), 672–80. Retrieved from http://www.ncbi.nlm.nih.gov/pubmed/9345626

Hawkes, P., & Spence, J. C. H. (2007). *Science of Microscopy*. *Science of Microscopy, Volume 2* (Vol. 982). http://doi.org/10.1007/978-0-387-49762-4

Henderson. (1995). The potential and limitations of neutrons, electrons and X-rays for atomic resolution microscopy of unstained biological molecules. Quarterly Reviews of Biophysics.

Henderson, R. (1990). Cryo-Protection of Protein Crystals against Radiation Damage in Electron and X-Ray Diffraction. *Proceedings of the Royal Society B: Biological Sciences*, *241*(1300), 6–8. http://doi.org/10.1098/rspb.1990.0057

Henderson, R., & Moffat, J. K. (1971). The difference Fourier technique in protein crystallography: errors and their treatment. *Acta Crystallographica Section B Structural Crystallography and Crystal Chemistry*, *27*(7), 1414–1420. http://doi.org/10.1107/S0567740871004060

Kabsch, W. (2014). Processing of X-ray snapshots from crystals in random orientations. *Acta Crystallographica Section D Biological Crystallography*, *70*(8), 2204–2216. http://doi.org/10.1107/S1399004714013534

Kirian, R. a, Wang, X., Weierstall, U., Schmidt, K. E., Spence, J. C. H., Hunter, M., … Holton, J. (2010). Femtosecond protein nanocrystallography - data analysis methods. *Optics Express*, *18*(6), 5713–5723. Retrieved from http://www.opticsexpress.org/abstract.cfm?URI=oe-18-6-5713

Kirian, R. a, White, T. a, Holton, J. M., Chapman, H. N., Fromme, P., Barty, A., … Spence, J. C. H. (2011). Structure-factor analysis of femtosecond microdiffraction

patterns from protein nanocrystals. *Acta Crystallographica. Section A, Foundations of Crystallography*, *67*(Pt 2), 131–40. http://doi.org/10.1107/S0108767310050981

Kirkland, E. J. (2010). *Advanced computing in electron microscopy: Second edition*. *Advanced Computing in Electron Microscopy: Second Edition*. http://doi.org/10.1007/978-1-4419-6533-2

Kupitz, C., Basu, S., Grotjohann, I., Fromme, R., Zatsepin, N. a., Rendek, K. N., … Fromme, P. (2014). Serial time-resolved crystallography of photosystem II using a femtosecond X-ray laser. *Nature*, *513*, 261. http://doi.org/10.1038/nature13453

Leslie, A. G. W. (2006). The integration of macromolecular diffraction data. *Acta Crystallographica. Section D, Biological Crystallography*, *62*(Pt 1), 48–57. http://doi.org/10.1107/S0907444905039107

Liu, W., Wacker, D., Gati, C., Han, G. W., James, D., Wang, D., … Cherezov, V. (2013). Serial femtosecond crystallography of G protein-coupled receptors. *Science*, *342*(6165), 1521–4. http://doi.org/10.1126/science.1244142

Loh, N. T. D., & Elser, V. (2009). Reconstruction algorithm for single-particle diffraction imaging experiments. *Physical Review E - Statistical, Nonlinear, and Soft Matter Physics*, *80*(2). http://doi.org/10.1103/PhysRevE.80.026705

Lutman, a. a., Coffee, R., Ding, Y., Huang, Z., Krzywinski, J., Maxwell, T., … Nuhn, H.-D. (2013). Experimental Demonstration of Femtosecond Two-Color X-Ray Free-Electron Lasers. *Physical Review Letters*, *110*(13), 134801. http://doi.org/10.1103/PhysRevLett.110.134801

Neutze, R., Wouts, R., van der Spoel, D., Weckert, E., & Hajdu, J. (2000). Potential for biomolecular imaging with femtosecond X-ray pulses. *Nature*, *406*(6797), 752–757. http://doi.org/10.1038/35021099

Philipp, H. T., Ayyer, K., Tate, M. W., Elser, V., & Gruner, S. M. (2012). Solving structure with sparse, randomly-oriented x-ray data. *Optics Express*, *20*(12), 13129. http://doi.org/10.1364/OE.20.013129

Powell, H. R. (1999). The Rossmann Fourier autoindexing algorithm in MOSFLM. *Acta Crystallographica Section D: Biological Crystallography*, *55*(10), 1690–1695. http://doi.org/10.1107/S0907444999009506

Press, W. H., Flannery, B. P., Teukolsky, S. A., & Vetterling, W. T. (1988). *Numerical recipes in C*. Cambridge University Press.

Redecke, L., Nass, K., DePonte, D. P., White, T. a, Rehders, D., Barty, A., … Chapman, H. N. (2013). Natively inhibited Trypanosoma brucei cathepsin B structure determined by using an X-ray laser. *Science (New York, N.Y.)*, *339*(6116), 227–30. http://doi.org/10.1126/science.1229663

Rossmann, M. G., Leslie, A. G. W., Abdel-Meguid, S. S., & Tsukihara, T. (1979). Processing and Post-Refinement of Oscillation Camera Data. *J. Appl. Cryst.*, *12*, 570–581.

Snell, E. H., Bellamy, H. D., & Borgstahl, G. E. (2003). Macromolecular crystal quality. *Methods in Enzymology*, *368*, 268–88. http://doi.org/10.1016/S0076-6879(03)68015-8

Solem, J. (1986). Imaging biological specimens with high-intensity soft x rays. *Journal of the Optical Society of America B*, *3*(11), 1551–1565. http://doi.org/10.1364/JOSAB.3.001551

Spence, J. (2008). Two-wavelength inversion of multiply scattered soft X-ray intensities to charge density. *Acta Crystallographica Section A: Foundations of Crystallography*, *65*(1), 28–38. http://doi.org/10.1107/S0108767308032728

Spence, J. (2014). Approaches to time-resolved diffraction using and XFEL. *Faraday Discussions*, *171*(Mx), 429–438. http://doi.org/10.1039/c4fd00025k

Spence, J. C. H. (2010). *High-Resolution Electron Microscopy* (third).

Spence, J. C. H., Calef, B., & Zuo, J. M. (1999). Dynamic inversion by the method of generalized projections. *Acta Crystallographica Section A Foundations of Crystallography*, *55*(2), 112–118. http://doi.org/10.1107/S0108767398006977

Spence, J. C. H., Weierstall, U., & Chapman, H. N. (2012). X-ray lasers for structural and dynamic biology. *Reports on Progress in Physics. Physical Society (Great Britain)*, *75*(10), 102601. http://doi.org/10.1088/0034-4885/75/10/102601

Spence, J. C. H., Zatsepin, N. A., & Li, C. (2014). Coherent convergent-beam time-resolved X-ray diffraction. *Phil. Trans. R. Soc. B*, *369*(June), 20130325.

Spence, J. C. H., & Zuo, J. M. (1992). *Electorn Microdiffraction*. Plenum Press.

Steller, I., Bolotovsky, R., & Rossmann, M. (1997). An algorithm for automatic indexing of oscillation images using Fourier analysis. *Journal of Applied Crystallography*, 1036–1040. http://doi.org/10.1107/S0021889897008777

Stevenson, H. P., Deponte, D. P., Makhov, A. M., Conway, J. F., Zeldin, O. B., Boutet, S., & Calero, G. (2014). Transmission electron microscopy as a tool for nanocrystal characterization pre- and post-injector Transmission electron microscopy as a tool for nanocrystal characterization pre- and. *Phil. Trans. R. Soc. B*, *369*, 20130322.

Sundberg, R. (1974). Maximum Likelihood Theory for Incomplete Data from an Exponential Family. *Scandinavian Journal of Statistics*, *1*(2), 49–58. Retrieved from http://www.jstor.org/stable/4615553\npapers2://publication/uuid/C155C882-B614-4D6D-A783-7DA1DB775C43

Tenboer, J. (2014). Time-resolved serial crystallography captures high-resolution intermediates of photoactive yellow protein. *Science*, 1–6.

Van Den Broek, W., & Koch, C. T. (2012). Method for retrieval of the three-dimensional object potential by inversion of dynamical electron scattering. *Physical Review Letters*, *109*(24). http://doi.org/10.1103/PhysRevLett.109.245502

White, T. (2014). Post-refinement method for snapshot serial crystallography Post-refinement method for snapshot serial crystallography. *Phil. Trans. R. Soc. B*, *369*(June), 20130330.

White, T. a., Barty, A., Stellato, F., Holton, J. M., Kirian, R. a., Zatsepin, N. a., & Chapman, H. N. (2013). Crystallographic data processing for free-electron laser sources. *Acta Crystallographica Section D Biological Crystallography*, *69*(7), 1231–1240. http://doi.org/10.1107/S0907444913013620

White, T. a., Kirian, R. a., Martin, A. V., Aquila, A., Nass, K., Barty, A., & Chapman, H. N. (2012). CrystFEL : a software suite for snapshot serial crystallography. *Journal of Applied Crystallography*, *45*(2), 335–341. http://doi.org/10.1107/S0021889812002312

Zachariasen, W. H. (1967). *Theory of X-ray diffraction in crystals*. Dover, Toronto.

Zhu, D., Cammarata, M., Feldkamp, J. M., Fritz, D. M., Hastings, J. B., Lee, S., … Feng, Y. (2012). A single-shot transmissive spectrometer for hard x-ray free electron lasers A single-shot transmissive spectrometer for hard x-ray free electron lasers, *34103*, 1–5. http://doi.org/10.1063/1.4736725

APPENDIX A

STATISTICS OF TbCatB CRYSTAL SHAPE TRANSFORM CALCULATED BY MONTE-CARLO SIMULATION

To characterize the source of errors in XFEL experiments, Monte-Carlo simulations were conducted to estimate the dominant contribution from the large intensity fluctuation across the shape transform based on its statistics. Shape transforms were modeled using Eqn. (3.4) for TbCatB crystals (Redecke, 2013) of 0.9×0.9×11μm average size with 10% Gaussian-distributed deviation. Statistics of intensity variation across the shape transform depend on the integration radius δ_t. Therefore, mean value, standard deviation and their ratio (relative deviation) were calculated as functions of δ_t as a fraction of the scattering vector (Fig. A1). δ_t ranges from 0 to 0.1 with an increment of 0.01, and for each value of δ_t, 10^6 sampling points on the shape transform were randomly generated for a uniform distribution. At δ_t=0.01 which matches the average size of the crystal, the mean value and the relative deviation of the shape transform for TbcatB crystals was found to be 1.76×10^{12} and 5.7 respectively.

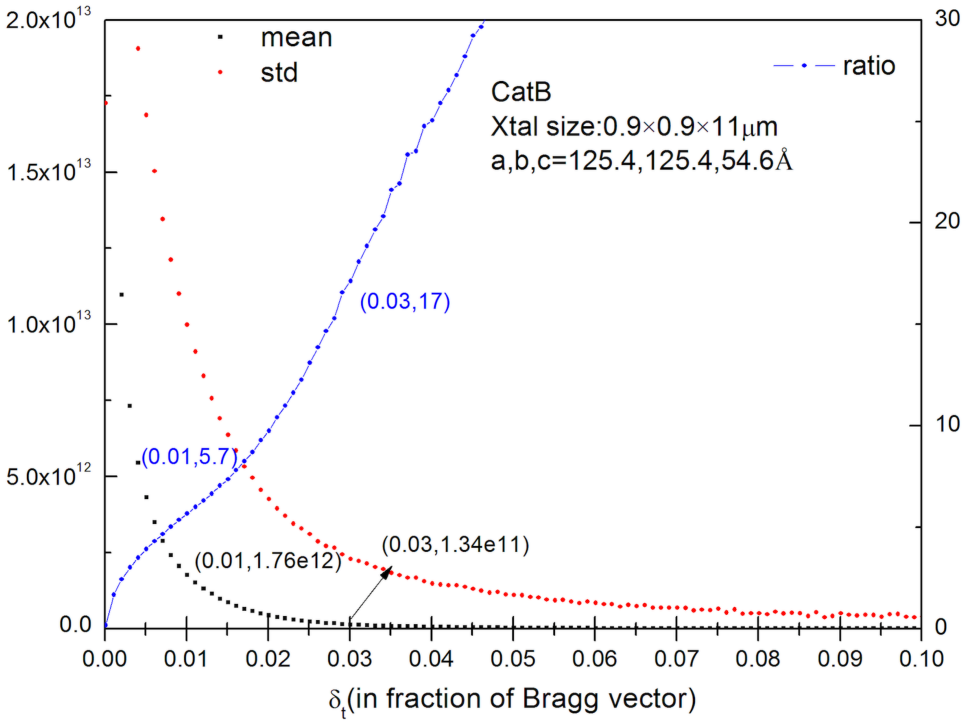

Fig. A.1. Statistics (mean, standard deviation, and relative deviation/ratio) of TbcatB crystal shape transform obtained from Monte-Carlo simulation. 10% standard deviation in crystal size was assumed based on experimental data (Redecke et al., 2013). The abscissa δ_t is the integration radius around Bragg peaks; left vertical axis shows the mean and standard deviation values; right vertical axis shows the relative deviation/ratio.

APPENDIX B

ERROR ANALYSIS FOR TWO-COLOR APPROACH

According to error propagation theory (Bevington & Robinson, 1992), errors in different variables are related as follows:

$$\sigma\left(R'^{(i)}_{(hkl)}\right)=\sigma\left(\sqrt{A^{(i)}_{(hkl)}}\right) \tag{B.1}$$

$$\frac{\sigma\left(\sqrt{A^{(i)}_{(hkl)}}\right)}{\left\langle\sqrt{A^{(i)}_{(hkl)}}\right\rangle}=\frac{1}{2}\frac{\sigma\left(A^{(i)}_{(hkl)}\right)}{\left\langle A^{(i)}_{(hkl)}\right\rangle} \tag{B.2}$$

$$\frac{\sigma\left(A^{(i)}_{(hkl)}\right)}{\left\langle A^{(i)}_{(hkl)}\right\rangle}=\sqrt{\left(\frac{\sigma\left(I^{(i)}_{1,(hkl)}\right)}{I^{(i)}_{1,(hkl)}}\right)^2+\left(\frac{\sigma\left(I^{(i)}_{2,(hkl)}\right)}{I^{(i)}_{2,(hkl)}}\right)^2+\left(\frac{\sigma\left(k_{12}\right)}{k_{12}}\right)^2} \tag{B.3}$$

$$\sigma\left(I^{(i)}_{1,(hkl)}\right)=\sqrt{I^{(i)}_{1,(hkl)}}\,;\,\sigma\left(I^{(i)}_{2,(hkl)}\right)=\sqrt{I^{(i)}_{2,(hkl)}}\,;\,\alpha\equiv\frac{\sigma\left(k_{12}\right)}{k_{12}} \tag{B.4}$$

$$\sigma\left(R'^{(i)}_{(hkl)}\right)=\frac{\left\langle\sqrt{A_{(hkl)}}\right\rangle}{2}\cdot\sqrt{\frac{1}{I^{(i)}_{1,(hkl)}}+\frac{1}{I^{(i)}_{2,(hkl)}}+\alpha^2} \tag{B.5}$$

In order to analyze the error in $R'^{(N)}_{(hkl)}$, we express it explicitly in terms of the experimentally measured parameters as below:

$$R'^{(N)}_{(hkl)}=\sqrt{\frac{\sum_{i=1}^{N}I^{(i)}_{2,(hkl)}\cdot\left\langle k^{(i)}_{12}\right\rangle}{\sum_{i=1}^{N}I^{(i)}_{1,(hkl)}}}-1 \tag{B.6}$$

To show that $R'^{(N)}_{(hkl)}$ is indeed a valid estimate of $R_{(hkl)}$ which is the true value of the relative change in structure factor magnitude $\left|F_{(hkl)}\right|$, we show that the average value (expectation) of $R'^{(N)}_{(hkl)}$ approaches the true value $R_{(hkl)}$ when the number of shots N is sufficiently large. The average value of $R'^{(N)}_{(hkl)}$ is:

$$\left\langle R'^{(N)}_{(hkl)} \right\rangle \Big|^{\text{intensity}} = \sqrt{\frac{\sum_{i=1}^{N} \left\langle I^{(i)}_{2,(hkl)} \right\rangle \Big|^{\text{intensity}} \cdot \left\langle k^{(i)}_{12} \right\rangle}{\sum_{i=1}^{N} \left\langle I^{(i)}_{1,(hkl)} \right\rangle \Big|^{\text{intensity}}}} - 1 \tag{B.7}$$

We define $\Delta^{(i)}$ as the discrepancy between $k^{(i)}_{12}$ and its expectation value $\left\langle k^{(i)}_{12} \right\rangle$

$$\Delta^{(i)} \equiv k^{(i)}_{12} - \left\langle k_{12} \right\rangle \tag{B.8}$$

Then, Eqn. (B.7) can be rewritten as:

$$\left\langle R'^{(N)}_{(hkl)} \right\rangle \Big|^{\text{intensity}} = \sqrt{\frac{\sum_{i=1}^{N} \left\langle I^{(i)}_{2,(hkl)} \right\rangle \Big|^{\text{intensity}} \cdot k^{(i)}_{12}}{\sum_{i=1}^{N} \left\langle I^{(i)}_{1,(hkl)} \right\rangle \Big|^{\text{intensity}}} - \frac{\sum_{i=1}^{N} \left\langle I^{(i)}_{2,(hkl)} \right\rangle \Big|^{\text{intensity}} \cdot \Delta^{(i)}}{\sum_{i=1}^{N} \left\langle I^{(i)}_{1,(hkl)} \right\rangle \Big|^{\text{intensity}}}} - 1 \tag{B.9}$$

If the number of shots N goes to infinity, or more practically, we have a sufficiently large number of shots from which diffraction patterns are collected, the second term under the square root sign approaches 0:

$$\lim_{N \to \infty} \left(\frac{\sum_{i=1}^{N} \left\langle I^{(i)}_{2,(hkl)} \right\rangle \Big|^{\text{intensity}} \cdot \Delta^{(i)}}{\sum_{i=1}^{N} \left\langle I^{(i)}_{1,(hkl)} \right\rangle \Big|^{\text{intensity}}} \right) = \left\langle \Delta^{(i)} \right\rangle = 0 \tag{B.10}$$

Hence, the average of $R'^{(N)}_{(hkl)}$ approaches the true value $R_{(hkl)}$

$$\lim_{N \to \infty} R'^{(N)}_{(hkl)} = R_{(hkl)} \tag{B.11}$$

Therefore, $R'^{(N)}_{(hkl)}$ is a good estimate of the relative change in structure factor magnitude.

We now omit the Bragg order index $_{(hkl)}$ from subscripts and $^{(N)}$ from superscripts. Additionally, we define some auxiliary variables for notational convenience as follows:

$$R' = \sqrt{A} - 1 \tag{B.12}$$

$$A = \frac{\sum_{i=1}^{N}\left(I_2^{(i)}\langle k_{12}\rangle\right)}{\sum_{i=1}^{N} I_1^{(i)}} \equiv \frac{B}{D} \tag{B.13}$$

$$B = \sum_{i=1}^{N} B^{(i)}\,;\; B^{(i)} = \left(I_2^{(i)}\langle k_{12}\rangle\right);\; D = \sum_{i=1}^{N} I_1^{(i)} \tag{B.14}$$

According to the theory of errors, the errors in the different variables are related as follows:

$$\sigma\left(R'\right) = \sigma\left(\sqrt{A}\right) \tag{B.15}$$

$$\frac{\sigma^2(A)}{\langle A\rangle^2} = \frac{\sigma^2(B)}{\langle B\rangle^2} + \frac{\sigma^2(D)}{\langle D\rangle^2} \tag{B.16}$$

$$B^{(i)} = \left(I_2^{(i)} \cdot \langle k_{12}\rangle\right) \tag{B.17}$$

$$\frac{\sigma^2\left(B^{(i)}\right)}{\left\langle B^{(i)}\right\rangle^2} = \frac{1}{\left\langle I_2^{(i)}\right\rangle} + \left(\frac{\sigma\left(k_{12}\right)}{\langle k_{12}\rangle}\right)^2 = \frac{1}{\left\langle I_2^{(i)}\right\rangle} + \alpha^2 \tag{B.18}$$

$$\begin{aligned}\sigma^2(B) &= \sum_{i=1}^{N}\sigma^2(B^{(i)}) \\ &= \sum_{i=1}^{N}\left(\left\langle I_2^{(i)}\right\rangle^2 \langle k_{12}\rangle^2\left(\frac{1}{\left\langle I_2^{(i)}\right\rangle} + \alpha^2\right)\right)\end{aligned} \tag{B.19}$$

$$\sigma^2(D) = \sum_{i=1}^{N}\sigma^2\left(I_1^{(i)}\right) = \sum_{i=1}^{N}\left\langle I_1^{(i)}\right\rangle \tag{B.20}$$

Combining Eqn. (B.15) – (B.20), we obtain the error in A, hence R′

$$\frac{\sigma^2(A)}{\langle A\rangle^2} = \frac{\sum_{i=1}^{N}\left(\left\langle I_2^{(i)}\right\rangle^2 \langle k_{12}\rangle^2 \left(\frac{1}{\left\langle I_2^{(i)}\right\rangle} + \alpha^2\right)\right)}{\left\langle \sum_{i=1}^{N} I_2^{(i)}\right\rangle^2 \langle k_{12}\rangle^2} + \frac{\sum_{i=1}^{N}\left\langle I_1^{(i)}\right\rangle}{\left\langle \sum_{i=1}^{N} I_1^{(i)}\right\rangle^2}$$

$$= \frac{1}{\sum_{i=1}^{N}\left\langle I_2^{(i)}\right\rangle} + \frac{1}{\sum_{i=1}^{N}\left\langle I_1^{(i)}\right\rangle} + \alpha^2 \cdot \frac{\sum_{i=1}^{N}\left\langle I_2^{(i)}\right\rangle^2}{\left\langle \sum_{i=1}^{N}\left\langle I_2^{(i)}\right\rangle\right\rangle^2} \tag{B.21}$$

$$\approx \frac{1}{\sum_{i=1}^{N} I_2^{(i)}} + \frac{1}{\sum_{i=1}^{N} I_1^{(i)}} + \alpha^2 \cdot \frac{\sum_{i=1}^{N}\left(I_2^{(i)}\right)^2}{\left(\sum_{i=1}^{N} I_2^{(i)}\right)^2}$$

$$\equiv T1 + T2 + T3$$

$$\sigma(R') = \sigma\left(\sqrt{A}\right) = \frac{1}{2}\sqrt{\langle A\rangle} \cdot \sqrt{T1 + T2 + T3} \tag{B.22}$$

In case of a large value of N, the sampling can cover the whole intensity distribution of Bragg reflections ergodically with much less fluctuation than for small values of N. Instead of using Eqn. (B.21), we estimate the error in R′ using the expectation value of the refection intensity $I_1^{(i)}$ and $I_2^{(i)}$ over the entire intensity distribution:

$$\lim_{N\to\infty} T1 = \frac{1}{N}\frac{1}{\left\langle I_2^{(i)}\right\rangle\Big|_{shots}^{\text{intensity}}} \tag{B.23}$$

$$\lim_{N\to\infty} T2 = \frac{1}{N}\frac{1}{\left\langle I_1^{(i)}\right\rangle\Big|_{shots}^{\text{intensity}}} \tag{B.24}$$

$$\lim_{N\to\infty}\frac{\sum_{i=1}^{N}\left\langle I_2^{(i)}\right\rangle^2}{\left\langle\sum_{i=1}^{N}I_2^{(i)}\right\rangle^2}=\frac{N\left(\left\langle I_2^{(i)}\right\rangle^2\right)\Big|_{\text{shots}}^{\text{intensity}}}{\left(N\left\langle I_2^{(i)}\right\rangle\Big|_{\text{shots}}^{\text{intensity}}\right)^2} \tag{B.25}$$

$$=\frac{N\left(\left(\left\langle I_2^{(i)}\right\rangle\Big|_{\text{shots}}^{\text{intensity}}\right)^2+\sigma^2\left(I_2^{(i}\right)\right)}{N^2\left(\left\langle I_2^{(i)}\right\rangle\Big|_{\text{shots}}^{\text{intensity}}\right)^2} \tag{B.26}$$

$$=\frac{1}{N}\left(1+\left(\frac{\sigma\left(I_2^{(i)}\right)}{\left\langle I_2^{(i)}\right\rangle\Big|_{\text{shots}}^{\text{intensity}}}\right)^2\right) \tag{B.27}$$

$$=\frac{1}{N}\left(1+\beta^2\right) \tag{B.28}$$

$$\beta\equiv\frac{\sigma\left(I_2^{(i)}\right)}{\left\langle I_2^{(i)}\right\rangle\Big|_{\text{shots}}^{\text{intensity}}} \tag{B.29}$$

$$\lim_{N\to\infty}T3=\frac{1}{N}\left(1+\beta^2\right)\alpha^2 \tag{B.30}$$

Therefore, the error in R′ can be estimated as below:

$$\sigma\left(R'\right)=\frac{1}{2}\sqrt{\langle A\rangle}\cdot\sqrt{T1+T2+T3} \tag{B.31}$$

$$\xrightarrow{N\to\infty}\frac{1}{2}\sqrt{\langle A\rangle}\cdot\sqrt{\frac{1}{\left\langle I_2^{(i)}\right\rangle\Big|_{\text{shots}}^{\text{intensity}}}+\frac{1}{\left\langle I_1^{(i)}\right\rangle\Big|_{\text{shots}}^{\text{intensity}}}+\left(1+\beta^2\right)\alpha^2}\cdot\frac{1}{\sqrt{N}} \tag{B.32}$$

where $\left\langle I_1^{(i)}\right\rangle\Big|_{\text{shots}}^{\text{intensity}}$ and $\left\langle I_2^{(i)}\right\rangle\Big|_{\text{shots}}^{\text{intensity}}$ are the expectation values over the rocking curve of the reflection intensities from the first and second pulses respectively. β is the relative standard deviation in $I_2^{(i)}$ over the rocking curve, and α denotes the relative error in k_{12}. The ratio of the intensities of the two pulses k_{12} varies from shot to shot, and this amplitude of fluctuation is characterized by α and determined by the stability of the

emittance spoiler in the delay line.

APPENDIX C

DOSE ESTIMATION FOR NON-DAMAGING FIRST PULSE

It is recognized that the first pulse must be below the threshold so that not to damage the crystal severely. Actually, the intensity of the first X-ray pulse can be estimated and calculations are shown below for the feasibility check.

Assuming that we use I3C microcrystals which are generally larger than the X-ray beam size in our proposed experiment and Henderson safe dose limit of 1Gy at room temperature, the critical fluence corresponding to the safe dose DH=1Gy is:

$$F_C = D_H \cdot \rho L \tag{C.1}$$

For I3C crystals, the mass density $\rho = 2.809\ g \cdot cm^{-3}$, attenuation length at the photon energy of 6.6keV $L = 11.03\ \mu m$, $F_C = 31\ kJ \cdot m^{-2}$. Since the beam size is considered smaller than the micro-crystals, the effective interaction area is just:

$$A_{eff} = \frac{\pi}{4} d^2 \tag{C.2}$$

where d is the diameter of the X-ray beam focus. Assuming a beam focus of 4 um in diameter, we can estimate the total X-ray energy per pulse as:

$$E_{Tot} = F_C \cdot A_{eff} = 2.43 \times 10^9\ keV \tag{C.3}$$

and number of photons per pulse is:

$$N_{ph} = \frac{E_{Tot}}{E_{photon}} = 3.69 \times 10^8 \tag{C.4}$$

This is weaker compared to the typical parameter value of 1e12 per pulse which we have been using by a factor of 2710. Note that this is dependent on the beam size, the larger beam the more photons we can tolerate.

APPENDIX D

CAN WE SEPARATE THE TWO-COLOR PATTERNS? CRYSTAL SIZE MATTERS, MODELING MAY HELP.

The best we can hope is that the two patterns have sufficiently strong signals and can be separated to take the difference. But it seems that many people put question mark on that. I want to discuss about this issue in a qualitative level considering the crystal size and the energy difference. As we may notice, although the difference in photon energy results in two slightly different partials, these two partials are very close to each other on the same rocking curve, at least they are correlated, unlike the traditional random sampling in Monte-Carlo approach. Averaging over this difference might be much more efficient than averaging over the whole rocking curve, and this might converge much faster. However, whether we can separate the two patterns depends on several factors including the bandwidth, divergence of the X-ray beam energy difference between the pulses and also the crystal size. The effects of the former few factors are straightforward and I analyze only the effect of the crystal size. Crystal size is inversely proportional to the width of the rocking curve, and thus determines if we can resolve the two spots of the same Bragg order from two pulses with a certain energy difference. Big crystals generally have sharp rocking curves and small crystals have broad ones. Meanwhile, given a specific energy difference, the intensity difference is greater for larger crystals than for small ones. (Fig. D1) Therefore, we want an optimal size of crystals so that difference of the two partials is not significant and, at the same time, the two spots can still be resolved. (Fig. D1 bottom)

Also, it is worthwhile to note that the sign of the difference between the two partials

reverse if the two Ewald spheres cut the right half of the rocking curve. This implies that summing the differences over a large number of crystals might cancel this effect, and this process might converge faster than M.C. since the two partials are “correlated” somewhat and somehow. At this point, modeling can help.

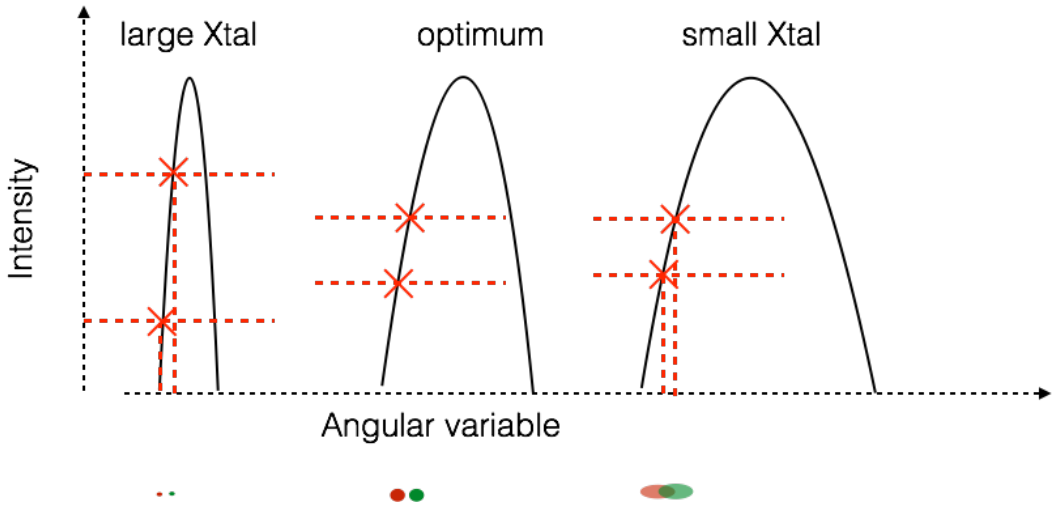

Fig. D.1. Schematic of two-color Ewald spheres intersecting at two different points with the rocking curve of a crystal of large size, optimal size and small size. The lower inset shows the corresponding Bragg spots of the same order from two colors in diffraction patterns. In the case of large crystal, the rocking curve is narrow, the two intersection points differs significantly in Bragg reflection intensity, while the diffraction spots are well separated. In the case of small crystal, the rocking curve is relatively broad, the two intersection points are close to each other and the difference in in reflection intensity is negligible, but the diffraction spots overlap. In case of crystal of optimal size, difference in Bragg reflection intensity between the intersection points is insignificant

and Bragg spots can be well separated.

APPENDIX E

MATLAB CODES FOR DYNAMICAL INVERSION

Forward Scattering Simulation (To generate simulated dynamical diffraction data

"fscode.m")

```
%parameterization
Klength=114.94; %for 1MeV beam energy. In this source code, crytallography
convention is adopted.
a=4.05;  %lattice parameter
thickness=10000;  %thickness of XTAL.
Ktx=0 ;Kty=0 ; % input the tangential componet of the incident wavevector.
Kn=-sqrt(Klength^2-Ktx^2-Kty^2); % calculate the normal component of the
incident wavevector.



%put G vectors involved into symmetric G matrix and open record file.
fid=fopen('Gvectors.txt','r');
   g=fscanf(fid,'%d',[3,69]);
   g=g.';
fclose('all')
fid=fopen('output.txt','w');
fprintf(fid,'Forward Scattering simulation\n');
 for l=0:68
     for m=1:3
       G(69+l,m)=1/a*g(l+1,m);
       G(69-l,m)=-1/a*g(l+1,m);
     end;
 end;

% establish the Fourier coefficients of XTAL potential as a function of
Glength.
syms u d R Glength v
   u=31.3; R=0.943; d=0.35;

v=@(Glength)u*exp(-R/d)*(sin(R*Glength*2*pi)+Glength*2*pi*d*cos(R*Glengt
h*2*pi))/(d*Glength*2*pi)/((d*Glength*2*pi)^2+1)/(3.8236*4*pi^2);

%establish the excitation error as a function of K vector and g vector.
Sg=@(Gx,Gy,Gz)(sqrt(Klength^2-((Gx^2+Gy^2+Gz^2)-(Ktx*Gx+Kty*Gy+Kn*Gz)^2/
Klength^2))-sqrt(((Ktx+Gx)^2+(Kty+Gy)^2+(Kn+Gz)^2)-((Gx^2+Gy^2+Gz^2)-(Kt
```

```
x*Gx+Kty*Gy+Kn*Gz)^2/Klength^2)));


%build the A matrice
for s=1:137
  for t=1:137

Glength=sqrt((G(s,1)-G(t,1))^2+(G(s,2)-G(t,2))^2+(G(s,3)-G(t,3))^2)/a; %
calculate the length
                                                                    %of
G(s-t) vector

A(s,t)=2*Klength*Sg(G(s,1),G(s,2),G(s,3))*(s==t)+v(Glength+eps*(s==t));
  end;
end;

%solve for eigenvalue spectrum and eigenvector matrice of A matrice.
[C,Gamma1]=eig(A);
C_1=inv(C);

%calculate the eigenvalue spectrum of S matrice by the A-S approach.
Gamma=Gamma1./(2*Kn);

%construct the matrice of eigenvalues Lamda for S matrice.
Lamda=zeros(137);
for s=1:137
  for t=1:137
    Lamda(s,t)=0+exp(2*pi*1i*Gamma(s,s)*thickness)*(s==t);
  end;
end;
% calculate Scattering matrice S.
S=C*Lamda/C;

%plot out the diffraction pattern.
Dx=G(:,1);Dy=G(:,2);I=(abs(S(:,69))).^2;
Dx=Dx.';Dy=Dy.';I=I.';
Size=1./abs(log(I))*10;
scatter3(Dx,Dy,I,Size,I,'fill')
view(0,90)
grid off
```

```
save('I.mat','I')
Sexp=abs(S);
save('S6.mat','S')
save('Sexp6.mat','Sexp')
save('A original.mat','A')
```

g vectors used in reciprocal space (“Gvectors.txt”)

```
0   0   0
1   1   1
-1  1   1
1   -1  1
1   1   -1
2   0   0
0   2   0
0   0   2
2   2   0
-2  2   0
2   0   2
-2  0   2
0   2   2
0   -2  2
3   1   1
-3  1   1
3   -1  1
3   1   -1
1   3   1
-1  3   1
1   -3  1
1   3   -1
1   1   3
-1  1   3
1   -1  3
1   1   -3
2   2   2
-2  2   2
2   -2  2
2   2   -2
4   0   0
```

```
0   4   0
0   0   4
3   3   1
-3  3   1
3   -3  1
3   3   -1
3   1   3
-3  1   3
3   -1  3
3   1   -3
1   3   3
-1  3   3
1   -3  3
1   3   -3
4   2   0
-4  2   0
4   0   2
-4  0   2
0   4   2
0   -4  2
0   2   4
0   -2  4
2   0   4
-2  0   4
2   4   0
-2  4   0
4   2   2
-4  2   2
4   -2  2
4   2   -2
2   4   2
-2  4   2
2   -4  2
2   4   -2
2   2   4
-2  2   4
2   -2  4
2   2   -4
```

Unitarity constraint for S matrices (“Sunitary.m”)

```
%Sunitary: unitary constraint of S matrix.



ErrorS6=zeros(500,1);
ErrorS17=zeros(500,1);
loop=1:2000;

for l6=1:100
    %calculate Phase of S.
    S6=Sexp6.*exp(1i*Phase6);
    S6_1=(S6\eye(137)+eye(137)/S6)/2;
    S6_H=S6';
    l6;
    ErrorS6(l6,1)=norm(S6_1-S6_H);
    S6_S=(S6_1+S6_H)/2;
    DS=diag(diag(S6_S));
    %modify using symmetry.
    S6_C=zeros(137)+DS;
    for s=1:137
        for t=1:137
            if (s~=t)
                S6_C(s,t)=(S6_S(s,t)+S6_S(t,s))/2;
            end
        end
    end
    Phase6=-angle(S6_C);
end

for l17=1:100
    %calculate Phase of S.
    S17=Sexp17.*exp(1i*Phase17);
    S17_1=(S17\eye(137)+eye(137)/S17)/2;
    S17_H=S17';
    l17;
    ErrorS17(l17,1)=norm(S17_1-S17_H);
    S17_S=(S17_1+S17_H)/2;
    DS=diag(diag(S17_S));
```

```
    %modify using symmetry.
    S17_C=zeros(137)+DS;
    for s=1:137
        for t=1:137
            if (s~=t)
                S17_C(s,t)=(S17_S(s,t)+S17_S(t,s))/2;
            end
        end
    end
    Phase17=-angle(S17_C);
end
```

Reality and orthonormality constraint for C matrices (“Corthogonal.m”)

```
%Corthogonal. make C matrix orthogonal by iterations.

ErrorC6=zeros(10,1);
ErrorC17=zeros(10,1);
loopC=1:10;
for k6=1:10
    C6_T=C6.';
    C6_1=inv(C6);
    k6;
    ErrorC6(k6,1)=norm(C6_1-C6_T);
    C6_S=(C6_T+C6_1)/2;
    C6=C6_S.';
end
for k17=1:10
    C17_T=C17.';
    C17_1=inv(C17);
    k17;
    ErrorC17(k17,1)=norm(C17_1-C17_T);
    C17_S=(C17_T+C17_1)/2;
    C17=C17_S.';
end
```

Phase retrieval for single S with constraints (“inversion7.m”)

```
%inversion7 add in the C constraints(real and orthogonal) to Phase.
```

```
%parameterization
Klength=114.94; %for 1MeV beam energy. In this source code, crytallography
convention is adopted.
a=4.05;  %lattice parameter
thickness=10000;  %thickness of XTAL. Illumination condition #6.
dthickness=0.01; %thickness step.
Ktx=0 ;Kty=0 ; % input the tangential componet of the incident wavevector.
Kn=-sqrt(Klength^2-Ktx^2-Kty^2); % calculate the normal component of the
incident wavevector.
fid=fopen('output.txt','w');
fprintf(fid,'inversion6\n');

%load experimental data and some prerequisites.
load('Sexp6.mat');
Sexp6=Sexp;
load('S6.mat');
SS6=S;
load('Sexp17.mat');
Sexp17=Sexp;
load('S17.mat');
SS17=S;
load('A original.mat'); %original A as the final aim.
Aorigin=A;
load('A from linear.mat'); %A from linear potential model.
Alinear=real(A);

A=Alinear;
DA=diag(diag(Aorigin));

Phase6=angle(expm(2*1i*pi*A*thickness/(2*Kn)));
Phase17=angle(expm(2*1i*pi*A*(thickness+dthickness)/(2*Kn)));
DETS6=zeros(2000,1);
DETS17=zeros(2000,1);
Error6=zeros(2000,1);
Error17=zeros(2000,1);
Error6_1=zeros(2000,1);
Error17_1=zeros(2000,1);
for L=1:2000
    Sunitary;
```

```
    S6=Sexp6.*exp(1i*Phase6); %construct S.
    [C6,Lamda6]=eig(S6);
    DETS6(L,1)=det(Lamda6);
    C6=real(C6);
    S17=Sexp17.*exp(1i*Phase17);
    [C17,Lamda17]=eig(S17);
    DETS17(L,1)=det(Lamda17);
    C17=real(C17);
    Corthogonal;
    Phase6=angle(C6*Lamda6*C6.');
    Phase17=angle(C17*Lamda17*C17.');
    L
    Error6(L,1)=norm(S6-SS6);
    Error6_1(L,1)=norm(C6*Lamda6*C6.'-S6);
    disp(Error6(L,1))
    disp(Error6_1(L,1))
    Error17(L,1)=norm(S17-SS17);
    Error17_1(L,1)=norm(C17*Lamda17*C17.'-S17);
    disp(Error17(L,1))
    disp(Error17_1(L,1))
end
S6=Sexp6.*exp(1i*Phase6);
S17=Sexp17.*exp(1i*Phase17);
```

Inversion from tow thicknesses or wavelengths (“inversion8.m”)

```
%inversion7 add in the C constraints(real and orthogonal) to Phase.

%parameterization
Klength=114.94; %for 1MeV beam energy. In this source code, crytallography
convention is adopted.
a=4.05;  %lattice parameter
thickness=10000;  %thickness of XTAL. Illumination condition #6.
dthickness=0.01; %thickness step.
Ktx=0 ;Kty=0 ; % input the tangential componet of the incident wavevector.
Kn=-sqrt(Klength^2-Ktx^2-Kty^2); % calculate the normal component of the
incident wavevector.
fid=fopen('output.txt','w');
fprintf(fid,'inversion6\n');
```

```
%load experimental data and some prerequisites.
load('Sexp6.mat');
Sexp6=Sexp;
load('S6.mat');
SS6=S;
load('Sexp17.mat');
Sexp17=Sexp;
load('S17.mat');
SS17=S;
load('A original.mat'); %original A as the final aim.
Aorigin=A;
load('A from linear.mat'); %A from linear potential model.
Alinear=real(A);

A=Alinear;
DA=diag(diag(Aorigin));

Phase6=angle(expm(2*1i*pi*A*thickness/(2*Kn)));
Phase17=angle(expm(2*1i*pi*A*(thickness+dthickness)/(2*Kn)));
DETS6=zeros(100,1);
DETS17=zeros(100,1);
Error6=zeros(100,1);
Error17=zeros(100,1);
ErrorA=zeros(100,1);
for L=1:100
    Sunitary;
    S6=Sexp6.*exp(1i*Phase6); %construct S.
    [C6,Lamda6]=eig(S6);
    DETS6(L,1)=det(Lamda6);
    C6=real(C6);
    S17=Sexp17.*exp(1i*Phase17);
    [C17,Lamda17]=eig(S17);
    DETS17(L,1)=det(Lamda17);
    C17=real(C17);
    Corthogonal;
    S6=C6*Lamda6*C6.';
    S6=(S6+S6.')/2;
    S6=Sexp6.*exp(1i*angle(S6));
    S17=C17*Lamda17*C17.';
```

```
    S17=(S17+S17.')/2;
    S17=Sexp17.*exp(1i*angle(S17));

S6=S6*(exp(2*1i*pi*trace(Aorigin)/(2*Kn)*thickness)/det(S6))^(1/137);

S17=S17*(exp(2*1i*pi*trace(Aorigin)/(2*Kn)*(thickness+dthickness))/det(S
17))^(1/137);
    A1=(S17/S6-eye(137))/(2*1i*pi*dthickness/(2*Kn)); %calculate A1.
    A2=(S6\S17-eye(137))/(2*1i*pi*dthickness/(2*Kn)); %calculate A2.
    %modify A using symmetry.
    tic
    disp('modifying A with symmmetry')
    A3=zeros(137)+DA;
    for s=1:137
        for t=1:137
            if (s~=t)

A3(s,t)=(A1(s,t)+A1(t,s)+A1((138-s),(138-t))+A1((138-t),(138-s))+A2(s,t)
+A2(t,s)+A2((138-s),(138-t))+A2((138-t),(138-s)))/8;
            end
        end
    end
    A3=real(A3);
    ErrorA(L,1)=norm(A3-Aorigin);
    toc
    Phase6=angle(expm(2*1i*pi*A3*thickness/(2*Kn)));
    Phase17=angle(expm(2*1i*pi*A3*(thickness+dthickness)/(2*Kn)));
    L
    Error6(L,1)=norm(S6-SS6);
    disp(Error6(L,1))
    Error17(L,1)=norm(S17-SS17);
    disp(Error17(L,1))
end
S6=Sexp6.*exp(1i*Phase6);
S17=Sexp17.*exp(1i*Phase17);
```